Multijunction Solar Cells on Epitaxial Templates

Thesis by
Melissa Jane Archer

In Partial Fulfillment of the Requirements
for the Degree of
Doctor of Philosophy

California Institute of Technology
Pasadena, California

2008

(Defended May 8, 2008)

In loving memory of

Astor Gary Griggs

(1920–2003)

and

Jane Bellows King

(1924–1994)

Acknowledgments

It's hard to believe that I have made it to the end of my graduate career. It seems only yesterday I was sitting in an apartment in Syracuse, NY, submitting grad school applications to 9 different schools for many different programs, and heading out on interviews for real jobs. In the end, I was shocked to be accepted into the PhD program at Caltech. I decided that sink or swim, I had to try my hand at a "real" engineering school. I'm glad I did.

The road has not been easy. There are many people that helped me get through the tough days and realize that quitting was not an option. I am grateful for the support and encouragement I found in my family. First, I'd like to thank my husband, Ray, for always being there. He has more experience lifting and bolting together UHV equipment than many people in our group. We spent many a weekend and evening opening up my chamber and putting it back together, only to be up all night waiting for a growth to finish. In addition, my Aunt Nancy provided a getaway from Pasadena. Her door was always open for me in San Diego when things got to be too much for me. My grandfather and step-grandmother in Palos Verdes Estates always made sure I never forgot that the beautiful coast was never far away. Last but not least, my family in Atlanta was always just a phone call away and provided me with much needed perspective.

I'd like to thank Harry Atwater for bringing me into his group. Harry was my source of perpetual optimism. When I saw only black clouds ahead and failures, he always saw a silver lining and reasons to keep trying. He was always ready to add new ideas and pushed me to see around the problems I was facing. Invariably, things did work out, just not always in the way I had hoped. In addition, I'd like to thank him for making conferences a priority. Though there were times when I thought I'd end up with nothing to say, I have learned a great deal about myself and the field I work in from my attendance and participation in conferences.

The Atwater group also provides a great deal of internal support. Many of us are on fairly individual projects, but we always seem to make time for each other when we are stuck. Specifically, I would like to thank Luke Sweatlock for being willing to help me work through my modeling problems and for always providing much needed levity. Brendan Kayes and Jen Dionne provided a great deal of assistance when I was getting started on working in Matlab. Ken Diest always provided a helping hand and critical perspective whenever asked, though with a dose of sarcasm at all times. Morgan Putnam added excitement to every day that he was in the office. Mike Kelzenberg provided significant assistance in setting up testing equipment in the lab and was always willing to stay late to help meet a deadline. I enjoyed my time in the Atwater group with: Julie Biteen, Julie Brewer, Ryan Briggs, Stan Burgos, Davis Darvish, Rene de Waele, Matt Dicken, Vivian Ferry, Carrie Hofmann, Seokmin Jeon, Greg Kimball, Krista Langeland, Andrew Leenheer, Gerald Miller, Imogen Pryce, Christine Richardson, Jen Ruglovsky, Katsu Tanabe, Darci Taylor, and Jimmy Zahler.

Several post-docs have passed through the Atwater group in my tenure. Young-bae Park helped me when I first joined the group to get my bearings and in understanding that sometimes you need to ask stupid questions. He always had more ideas for us to pursue that there was ever time for, but I appreciated his insight and encouraging words when I was struggling with MBE growth of Ge. He also taught me everything I know about AFM. Anna Foncuberta i Morral helped to show me the ropes of wafer bonding and understanding that in the end the key is to publish your results, not stop just before writing the paper. In addition, I have enjoyed working with Mike Filler, Sunjee Kim, Deirdre O'Carroll, and Domenico Pacifici.

The Atwater group would not run nearly as smoothly as it does without the assistance of April Neidholdt. She serves many purposes in our group, not the least of which is as a personal cheerleader for everyone of us. You can't leave her office without a smile on your face. In addition, administrative support was provided by Kathy Bubash, Irene Loera, Fran Matzen, Eleonora Vorobieff, and Cierina Marks, who have helped to solve problems when they arise.

I would like to thank Carol Garland in the TEM lab for all her encouragement and support in learning the ropes of the TEM and sample preparation. She has always seemed to have unlimited patience for my questions. In addition, Leslie Lamberson made all the wafer bow measurements possible. Ali Ghaffari provided me with my first introduction to the cleanrooms and equipment on campus.

I would like to thank Spectrolab for their assistance and support of this work. I know it has not been an easy road with tight deadlines. In particular, Daniel Law, Andreea Boca, and Richard King were pivotal in the work described here. I also appreciate that you all were friendly to me at conferences where I generally did not know anyone else, and you don't remind me too often of my first talk in Santa Barbara.

I have had the fortune to meet many great people during my time at Caltech. Though they are too many to name here, I would like to recognize our ChemE class for sticking by each other through the first year of terrible classes and quals. I would not have made it through without you guys. In particular, Harmony Gates, Marc Woodka, Ameri David, and John Carpenter: thank you for your support through the tough times.

I appreciate the financial support for this work provided by the National Science Foundation Graduate Research Fellowship Program and from the National Renewable Energy Laboratory.

Finally, I would like to thank my thesis committee: Professors Harry Atwater, Richard Flagan, Sossina Haile, Nate Lewis, and Dr. Richard King.

Melissa Archer
May 2008
Pasadena, CA

Abstract

Future ultrahigh efficiency multijunction solar cells will employ designs that feature three or four or more subcells utilizing lattice-mismatched structures to achieve an optimal band gap sequence for solar energy conversion. While lattice-mismatched multijunction cells have been fabricated recently using metamorphic growth approaches, use of direct wafer bonding techniques to enable lattice mismatch accommodation at the subcell interfaces allows considerably more design freedom and inherently higher-quality, defect-free active regions. This thesis presents new results on wafer bonding and layer transfer for integration of materials with large lattice mismatch, as well as modeling work to better understand the key material parameters in the design of new multijunction solar cells.

GaInP/GaAs dual junction solar cells on Ge/Si templates were fabricated using wafer bonding and ion implantation induced layer transfer techniques. Following layer transfer, the surface of the ~1.4 μm thick transferred Ge(100) has an as-transferred RMS roughness of ~20 nm and a near surface layer containing a high density of ion implantation-induced defects. The RMS roughness has been reduced to <1 nm. In addition, the effects of changing the strain state of the template substrate on the performance of the devices has been explored by comparing devices grown on Ge/Si and Ge/sapphire. The CTE mismatch between Si and GaAs/GaInP materials induces a tensile strain, whereas the sapphire substrate induces a compressive strain.

An analytical p-n junction device physics model for GaInP/GaAs/InGaAsP/InGaAs four junction solar cells was developed. Real behavior of solar cells is accounted for by including: free carrier absorption, temperature and doping effects on carrier mobility, as well as two recombination pathways: Shockley-Read-Hall recombination from a single mid gap trap level and surface recombination. Upper bounds set by detailed balance calculations can be approached by letting the parameters approach ideal conditions. Detailed balance calculations always benefit from added subcells, current matching requirements in series connected p-n multijunctions indicate a minimum performance required from added subcells for net contribution to the overall device. This model allows novel solar cell structures to be evaluated by providing realistic predictions of the performance limitations of these multijunction devices.

Contents

List of Figures

List of Tables

Portions of this thesis have been drawn from the following publications:

GaInP/GaAs dual junction solar cells on Ge/Si epitaxial templates. Melissa J. Archer, Daniel C. Law, Shoghig Mesropian, Moran Haddad, Christopher M. Fetzer, Arthur C. Ackerman, Corinne Ladous, Richard R. King and Harry A. Atwater, Applied Physics Letters, **92**, 103503, 2008

Role of hydrogen in hydrogen-induced layer exfoliation of germanium. James M. Zahler, Anna Foncuberta i Morral, Melissa J. Griggs, Harry A. Atwater, and Yves J. Chabal, Physical Review B **75**, 035309, 2007

pn Junction Heterostructure Device Physics Model of a Four Junction Solar Cell. Melissa J. Griggs, Brendan M. Kayes, and Harry A. Atwater, Proceedings of SPIE **6339**, 2006

Design Approaches and Materials Processes for Ultrahigh Efficiency Lattice Mismatched Multi-junction Solar Cells. Melissa J. Griggs, Daniel C. Law, Richard R. King, Arthur C. Ackerman, James M. Zahler, and Harry A. Atwater, Proceedings of the 4th World Conference on Photovoltaic Energy Conversion **857**, 2006

Spectroscopic Studies of the mechanism for hydrogen-induced exfoliation of InP. Anna Foncuberta i Morral, James M. Zahler, Melissa J. Griggs, Harry A. Atwater, and Yves J. Chabal, Physical Review B **72**, 085219, 2005

Chapter 1

Introduction

1.1 Current Photovoltaic Technology

The most plentiful source for renewable energy is the sun. There are several different ways of harnessing the energy of the sun including: photovoltaic, solar thermal (concentrated solar power), solar hot water, and thermal electric devices. Solar thermal, solar hot water, and thermal electric devices all rely on the heat produced through photon absorption. Photovoltaic devices provide direct conversion of solar energy to electricity. All of these processes have advantages and disadvantages. For example, in residential applications, solar hot water panels can significantly reduce the costs associated with water heating. In addition, solar thermal technologies in the form of concentrated solar power stations are ideally suited for areas without much cloud cover. These systems use a heat transfer fluid (water, oil, or molten salts) to absorb the energy from the sun and transfer that energy as heat to water, producing steam which can be used to run a turbine and generate electricity. One of the advantages of these systems is that by storing the hot fluid underground, several hours of energy storage can be achieved beyond the time when the sun sets for the evening.

Photovoltaic devices convert energy in the form of photons into electricity via an excited state. In solar cells made of semiconductor materials, each absorbed photon excites an electron from the valence band to the conduction band, producing an electron-hole pair. These carriers diffuse through the quasi-neutral material until they reach the pn junction where drift caused by the built-in electric field separates the carriers. For example, in figure 1.1, holes move to the bottom of the cell while electrons move to the top of the cell. This process produces a current which can be extracted. A solar cell will often consist of the semiconductor pn junction with a solid back metal contact, metal fingers on the top surface as a top contact, and an anti-reflective coating on the top surface. The front metal contact is in the form of stripes, rather than a continuous layer to allow sunlight through to the active

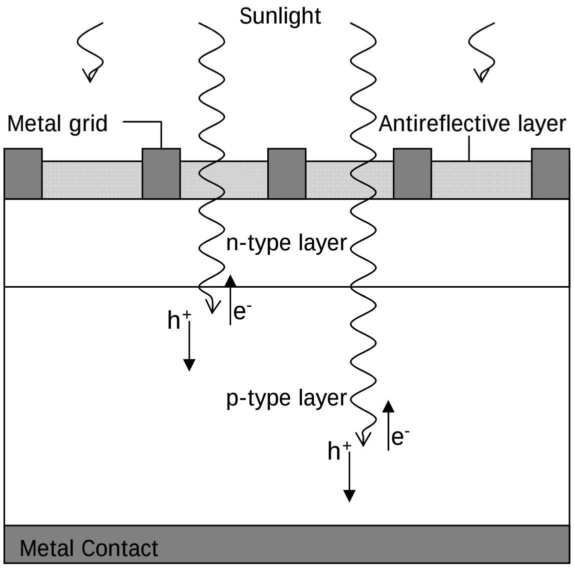

Figure 1.1. Schematic of a simple single junction solar cell

device. Often a key step in device design is optimizing the shape and size of the top metal contacts to minimize shadowing losses. Commercial crystalline silicon cells are available from SunPower with all back-side contacts, thereby eliminating this optimization problem. The anti-reflective coating minimizes reflection losses due to refractive index mismatch with air.

There are two primary limitations to solar cell performance. The first is due to the reversibility of the photon absorption process. A perfect defect-free crystal that absorbs light efficiently, also emits light efficiently. Generally speaking, all solar cell devices strive to be in the so-called “radiative-limit” wherein the only source of carrier recombination is through radiative processes. This means that all electron hole pairs generated through the absorption of photons are either separated and collected externally, or radiatively recombine emitting a photon. The only means of improving on this limit is to develop schemes for re-absorbing the emitted photons.

The second limitation is due to the single gap nature of semiconductors. Only those photons equal in energy to the band gap are absorbed efficiently. Photons greater in energy than the band gap are absorbed, but all energy in excess of the band gap is lost in the thermal relaxation of the generated hot carriers. Therefore, with a single junction solar cell, the overall conversion efficiency is inherently limited, as can be seen in figure 1.2.

There are several proposals for relaxing this limitation on solar cell efficiency. Two

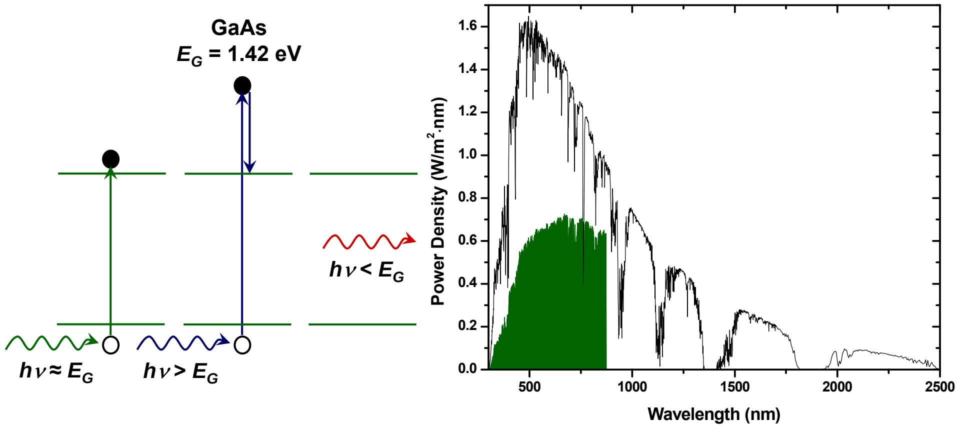

Figure 1.2. On the left, a schematic of the photons that are absorbed in a GaAs solar cell; on the right, a plot showing the solar spectrum (in black) and the power converted by the GaAs cell (the shaded green area). The maximum theoretical efficiency of this device is 30%.

ideas that go hand in hand are up-conversion[1] and down-conversion[2]. Up-converters work by using an external device to convert low energy photons into high energy photons. In this way, photons that would normally pass directly through a given solar cell can be captured on the back side of the device and re-emitted at a wavelength at or above the band gap. Down-converters are quite similar, but they perform work on the front side of a solar cell converting the high energy photons, whose excess energy is lost to thermalization, into multiple photons with energy equal to the band gap. It has been shown that up-converters will always help the performance of a device, whereas down-converters have to have a quantum efficiency greater than 1 to enhance the performance of a solar cell[3]. This makes intuitive sense, as the down-converter is on the front of the device and could potentially absorb light that would have been absorbed by the solar cell without re-emitting two photons of equal energy for the cell to absorb instead. In contrast, the up-converter is on the backside and therefore cannot interfere with the normal operation of the device. In this case, any photons it absorbs and re-emits at a higher energy than the band gap can only add to what the cell absorbs. Unfortunately, current up-converters have only been demonstrated using laser illumination and they generally only absorb one wavelength of light[4]. Therefore, this only captures one more energy line worth of material, rather than being a broadband absorber with single mode emission.

Other proposals which have been evaluated with varying degrees of success include intermediate gap solar cells[5, 6] and hot carrier solar cells [7]. The general idea behind the intermediate band solar cell is that three band gaps are created within one semiconductor material, therefore the collection efficiency of the device improves with multiple band gaps. In the hot carrier solar cell design, the electrons with energy in excess of the band gap would be extracted from the device at their full energy before relaxing to the conduction band through thermalization processes by minimizing electron-phonon interactions.

The main idea behind all of these high efficiency cell concepts is splitting the incoming energy spectrum into multiple segments, each of which are treated separately to enable more efficient collection. Another means of splitting the spectrum is to build the solar cell out of multiple semiconductor materials, and therefore multiple band gaps. There are two ways of integrating semiconductor materials with different band gaps, either use a filter to spatially split the spectrum over separate areas, or stack the materials together with the highest band gap at the top. The junctions have to be stacked in order of descending bad gap since each material is only transparent to those photons with energies less than the band gap. Therefore, the top material absorbs the highest energy photons. The current technology for these devices is a monolithic two-terminal device where multiple semiconductor solar cell devices are grown on top of each other. Connecting each pn junction is a tunnel junction. The tunnel junction provides a low-resistance connection between the p-type base of the upper cell and the n-type window of the lower cell. The tunnel junction is a degenerately doped pn junction where tunneling "shorts" the normal pn junction current characteristics below the peak tunneling current. Therefore, the tunnel junction must be designed such that the operating current of the device is below the peak tunneling current. A schematic of how this design can improve solar energy conversion is shown in figure 1.3. Due to the spectrum splitting advantages of multijunction solar cells, they are the leading technology for high-efficiency solar cells (figure 1.4).

1.2 Performance Limitations in Multijunction Solar Cells

Multijunction solar cells have several design requirements. The first is monolithic epitaxial integration of multiple single junction solar cells. This inherently requires that the device have only two terminals, and obey Kirchhoff's Law. In this way, all subcells must run at the same current. Therefore, one cell often limits performance of the entire device. To avoid this,

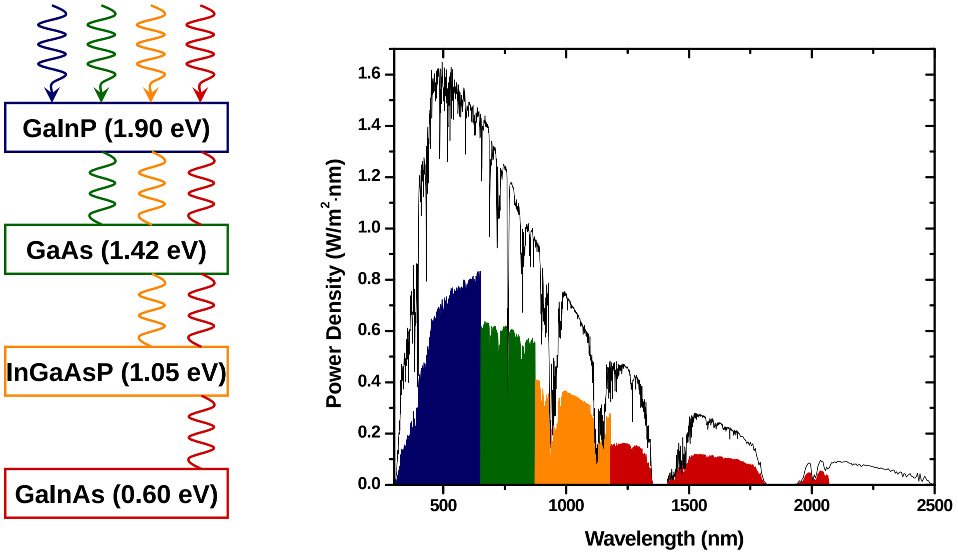

Figure 1.3. On the left, a schematic of the photons that are absorbed in a proposed four junction solar cell; on the right, a plot showing the solar spectrum (in black) and the power converted by each of the four subcells (the shaded area). The maximum theoretical efficiency of this device is 55%.

the cells would ideally be current matched such that the current produced in each subcell is the same due to appropriate spectrum splitting. Finally, to make good quality devices, the materials used must have well-understood band gaps and growth properties. Unfortunately, well-tuned band gaps are rarely found in lattice matched materials. Therefore high-quality monolithic epitaxy becomes quite difficult.

One of the most common multijunction cell technologies today is a triple junction design incorporating GaInP, GaAs, and Ge. Though these materials are nearly lattice matched (as can be seen from figure 1.5), the band gaps of the three junctions are not optimal. Given the GaInP, GaAs top two cells, the third cell would ideally have a band gap closer to 1 eV[8, 9]. Unfortunately, the Ge cell is poorly suited to the other two cells as its band gap is too low for current matching at 0.66 eV. Therefore, the Ge subcell overproduces current compared to the other two cells and all the heat generated from absorbing photons much higher in energy than its band gap just goes into heating the entire device. Though the III-V alloys provide a great deal of flexibility in band gap and lattice constant, it is still difficult to find three or more materials that are lattice matched with the appropriate band gaps for a well-optimized cell design. The options become much worse when looking to increase the number of junctions to four or more. The ideal band gaps, calculated via detailed balance,

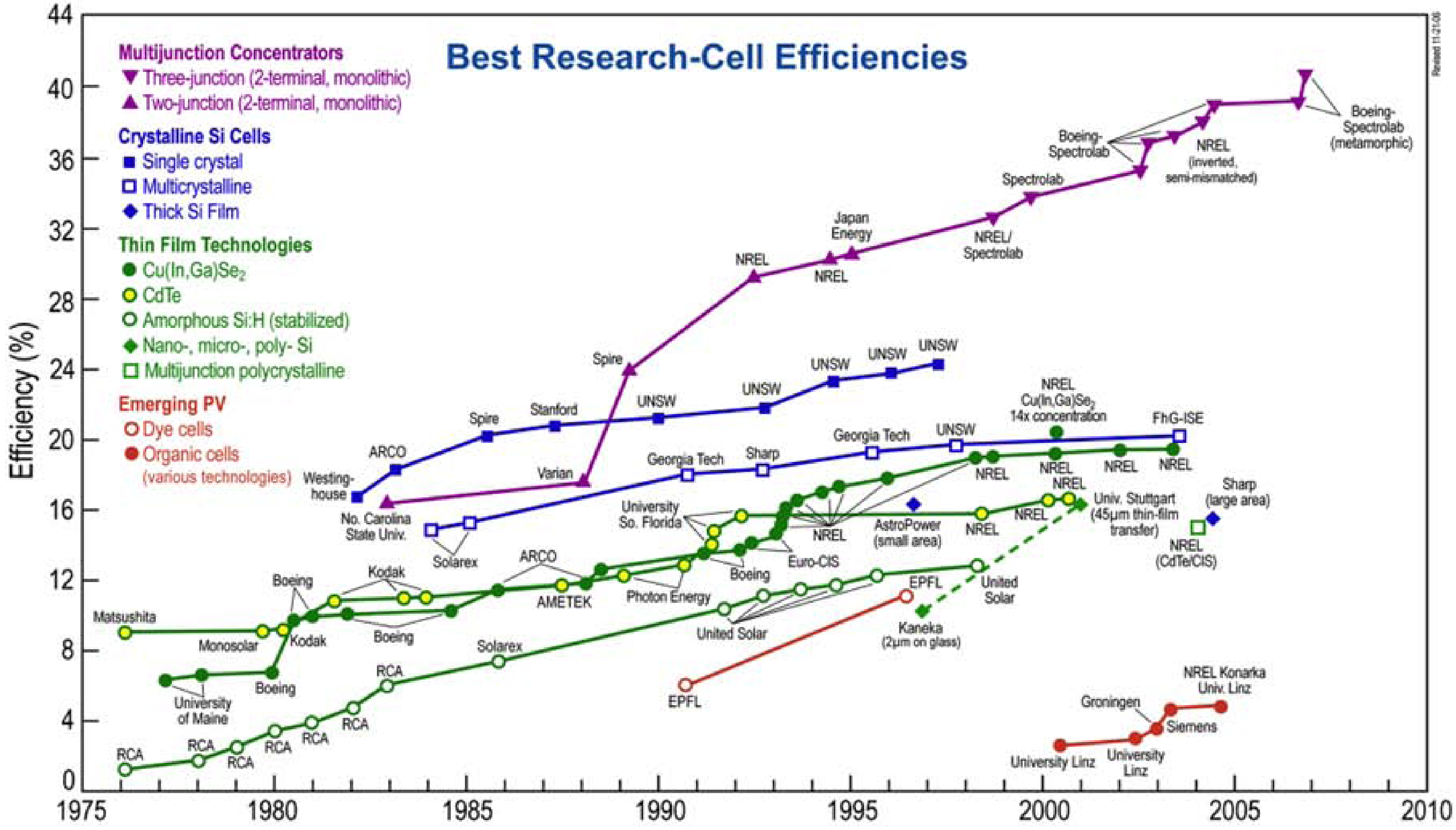

Figure 1.4. Graph of the world record efficiencies for different solar cell technologies by year

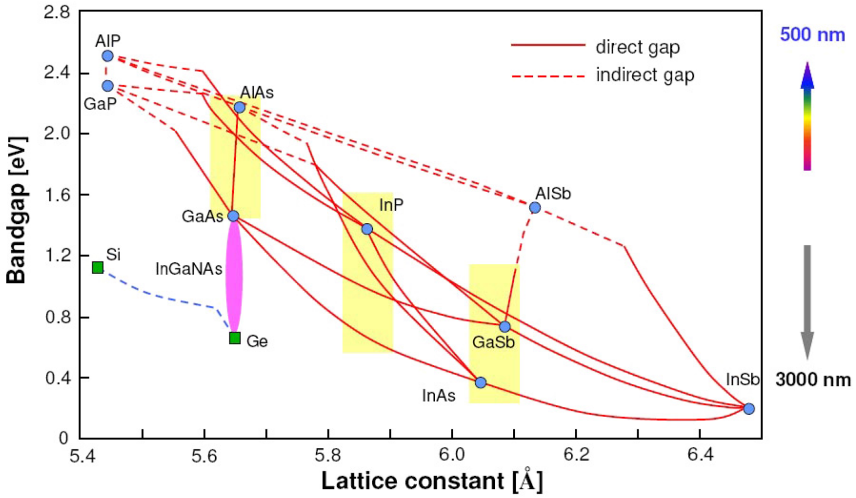

Figure 1.5. Plot of band gap versus lattice constant for III-V materials, with Si and Ge. Binary materials are shown as points, ternary alloys are indicated by connecting curves, and the quaternary alloys fill the area enclosed by the ternary curves.

for a four junction solar cell are 2.00/1.49/1.12/0.72 eV[10]. Detailed balance calculations will be discussed in further detail in Ch. 3. When looking at these band gaps in figure 1.5 it can clearly be seen that there are no lattice matched combinations of materials that can achieve these band gaps. Therefore, the high-efficiency solar cell community is looking for alternatives.

1.3 Metamorphic Growth Techniques

There has been a large amount of work in the past 35 years on direct epitaxial integration of lattice mismatched materials[11, 12, 13, 14, 15, 16]. Many advances have been made in reducing dislocation density of lattice mismatched epitaxial layers through graded buffer layers. Two of the most researched materials systems have been Ge_xSi_{1-x} on Si substrates and $In_xGa_{1-x}As$ on GaAs substrates. In both materials systems the final dislocation density has been reduced to the range of $10^5 - 10^6$ cm^{-2} in the epilayers grown over the buffer layers. This has been achieved for lattice mismatches on the order of 4% (the degree of mismatch between Ge and Si). The key to reducing the defect density in the final epitaxial layer is to maximize strain relaxation per misfit dislocation. In other words, the nucleation rate of misfit dislocations must be fast enough to relax the growing film, but simultaneously slow enough to allow threading dislocations to glide unimpeded to the film edge.

This requirement leads to several engineering limitations. First, the smaller the active area, the shorter the path to the edge for any dislocation. Related to that, as the active growth area gets larger, the growth temperature required goes up. With higher growth temperatures, dislocations can glide more quickly to the edges. However, at high growth temperatures, the nucleation rate of defects is higher.

In addition, the type of buffer layer grading can have a strong impact on the final structure. For example, in the $Ge_xSi_{1\text{-}x}$ system, it has been shown that step graded buffer layers are inferior to continuously graded buffer layers in defect nucleation and surface roughness. Several types of continuous grading have been explored, including linear, parabolic, and square root gradation[17]. Linearly graded buffer layers have shown smoother final films, though the parabolic gradation shows lower defect density in the final over layer.

The proper engineering of any given graded buffer layer is extremely dependent on material system. The $Ge_xSi_{1\text{-}x}$ system, for example, has exhibited a defect pileup phenomenon not seen in the $In_xGa_{1\text{-}x}As$ on GaAs system. In addition, accommodating very high lattice mismatch ($> 4\%$) is extremely difficult and the larger the mismatch, the thicker the required graded buffer layer.

Solar cell designs have employed metamorphic growth techniques for many years[18, 19, 20, 21, 22, 23, 24, 9, 25]. For example, in 1983, a 21.4% efficient metamorphic dual junction $Ga_{0.75}In_{0.25}As/GaAs$ solar cell was demonstrated[18]. In addition, the current world-record efficiency solar cell is a metamorphic $Ga_{0.44}In_{0.56}P/Ga_{0.92}In_{0.08}As/Ge$ cell with an efficiency of 40.7%[26]. The lattice mismatch between the top two cells and the Ge cell is 0.5%. Whereas the Spectrolab approach used a metamorphic buffer layer to bring the band gaps of the top two cells down, at NREL, they looked to correct the triple junction design by growing the cell upside down and using a metamorphic buffer layer to integrate a higher band gap third cell[9, 27]. The structure grown at NREL had 2% lattice mismatch, going from the GaInP/GaAs top two cells to $Ga_{0.7}In_{0.3}As$.

Unfortunately, the biggest limitation with metamorphic growth techniques, aside from the complexity, is in the amount of lattice mismatch that can be accommodated. When looking at designs with more than three junctions, it becomes very difficult to select materials that are viable for metamorphic growth techniques. Therefore, incorporating other techniques with metamorphic growth is required to achieve higher efficiency solar cells.

1.4 Wafer Bonding and Layer Transfer

Wafer bonding is the process by which two wafers are brought into contact with each other and "stick" together. In this way, they are nominally bonded. Generally, if the bonding occurs at room temperature the bond is relatively weak, as it is held together by van der Waals forces. To strengthen the bond, a secondary anneal step can be added which replaces the van der Waals bonds with strong covalent bonds between the two interfaces. All bulk materials have a well-defined surface reconstruction that is the lowest surface energy state for the material in air. In this fashion, no dangling bonds are present on the surface. Therefore, when two wafers are brought together, they cannot inherently break the surface reconstructed bonds to form new strong covalent bonds with the other wafer. However, with the addition of heat, the atoms at the interface are given enough energy to seek the new lowest energy state, which is connecting bonds to the new surface. In this way, strong covalent bonds are formed between the two wafers during the secondary anneal.

Due to the nature of wafer bonding, any degree of lattice mismatch can be accommodated fully at the bonded interface. As two crystalline materials are direct bonded together, there is no opportunity for defects to propagate through the material due to lattice mismatch. However, the largest limitation in wafer bonding is in engineering the appropriate substrates such that the coefficient of thermal expansion differences between the materials does not induce delamination or defects during thermal processing. Table 1.1 shows linear coefficients of expansion for common semiconductors. From this table, it is easy to see that some combinations of materials would inherently be more difficult to strain engineer than others.

1.5 Outline of This Thesis

This thesis presents experimental work developing epitaxial templates for use as substrates for compound semiconductor multijunction solar cell growth as well as modeling of these devices. The chapters are organized as follows:

Chapter 2 illustrates the process of creating Ge/Si epitaxial templates. The mechanism for layer transfer in Ge is described through the role of hydrogen in this process and compared to the mechanism in Si. The post-processing required after layer transfer is then described in detail, along with preliminary homoepitaxial and heteroepitaxial growth

Table 1.1. Linear coefficient of thermal expansion for common semiconductors at room temperature[28]

Material	CTE (ppm/°C)	Material (ppm/°C)	CTE
Si	2.6	AlAs	4.9
Si_3N_4	3.2	InSb	5.37
GaP	4.5	Ge	5.8
InAs	4.52	GaAs	6.86
InP	4.75	GaSb	7.75

results.

Chapter 3 describes the theoretical work that has been performed to develop a device physics based model to understand the limiting parameters of multijunction solar cells. First, an analytical model developed in Matlab is presented, followed by initial work with finite element method software packages.

Chapter 4 presents results from dual junction solar cells grown on Ge/Si epitaxial templates. The first results for GaInP/GaAs dual junction solar cells grown on Ge/Si epitaxial templates showing comparable performance to cells grown on bulk Ge are shown.

Finally, future directions for research in epitaxial templates and modeling of III-V multijunction solar cells are discussed.

Chapter 2

Wafer Bonding and Layer Transfer

2.1 Introduction: The History of Direct Bonding

Direct bonding of materials has been around at least as long as written history[29]. One early example is gold-glass technology from 300–600A.D., wherein gold and silver foils were direct bonded onto a black glass background and then covered by a thin translucent glass. Direct bonding with bond strengthening was first introduced in the 20th century by adding a secondary annealing step to form covalent bonds between the two materials. Finally, in the 1960s direct bonding with semiconductor wafers, namely silicon, was demonstrated. Since then, there has been great interest in semiconductor technology aimed at bringing lattice-mismatched materials together through this process.

One of the primary reasons for extensive research in direct bonding techniques in the 1970s was the realization of Silicon-On-Insulator (SOI) structures. SOI wafers are processed much as traditional silicon substrates for IC manufacturing. However, the embedded layer of insulation enables the SOI-based chips to function at significantly higher speeds while reducing electrical losses. The result is an increase in performance and a reduction in power consumption. In the first half of the 1980s, three separate companies independently reached a dedicated patent position on the formation of SOI structures by direct wafer bonding. Toshiba, IBM, and Philips all developed direct bonding processes that realized the creation of SOI structures.

Any entantiomorphic shapes can be directly bonded, though most current work focuses on two flat surfaces. Generally, direct bonding is a two-step process. First, the two materials are brought into contact with each other, producing a relatively weak bond between the two substrates governed by van der Waals forces. The second step is a higher temperature anneal, often under pressure, whereby the van der Waals bonds are eliminated in favor of covalent bonds between the two materials[30]. A schematic of the hydropho-

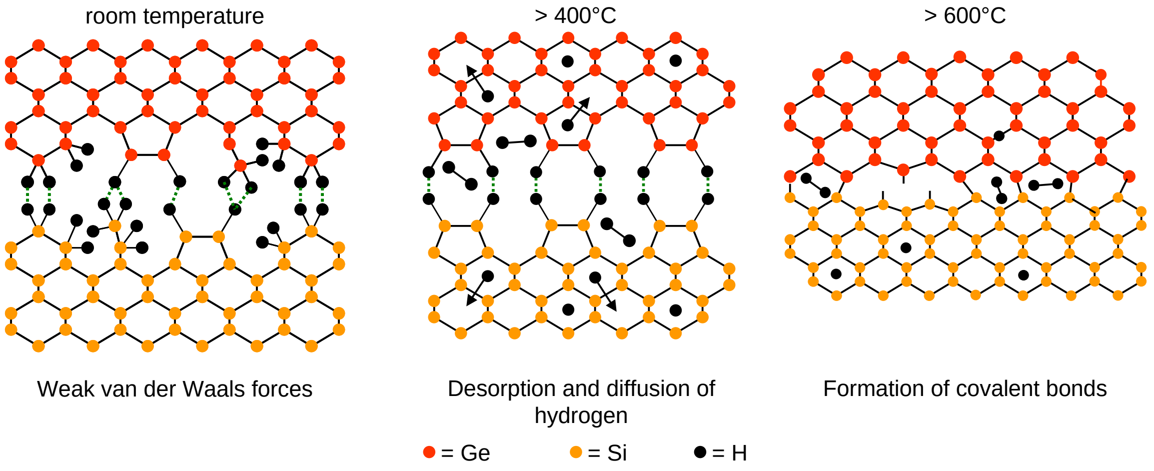

Figure 2.1. Schematic of bond evolution in hydrophobic bonding[30].

bic bonding process for Ge on Si is shown in figure 2.1. Through this process, two high quality single crystalline materials may be brought together and all defects due to lattice mismatch between the materials is fully accommodated at the bond interface. Therefore, unless strain from coefficient of thermal expansion mismatch between the two materials is not properly engineered, the two materials will be stable without any propagation of defects from the bond interface. If the strain engineering is not optimal, the bonded layer will either delaminate, or defects will propagate through the materials to alleviate the strain.

2.2 The Mechanism for Layer Transfer

2.2.1 Ion Implantation

Ion implanters consist of three main parts, the ion source, the accelerator, and the target chamber. Each ion is typically a single atom, and thus the dose, or amount of material implanted in the target, is the integral over time of the ion current. Ion energies are often between 10 and 400 keV. The energy of the ions, as well as the ion species and the composition of the target determine the depth of penetration of the ions in the solid[31].

Ion implantation is most commonly used in semiconductor technology as a method of doping. It is preferred over thermal diffusion due to the strict control over ion placement in the material. However, after implantation, the implanted wafers generally undergo an annealing process to repair the lattice damage caused by implantation and to move the implanted ions into electrically active sites in the crystal lattice.

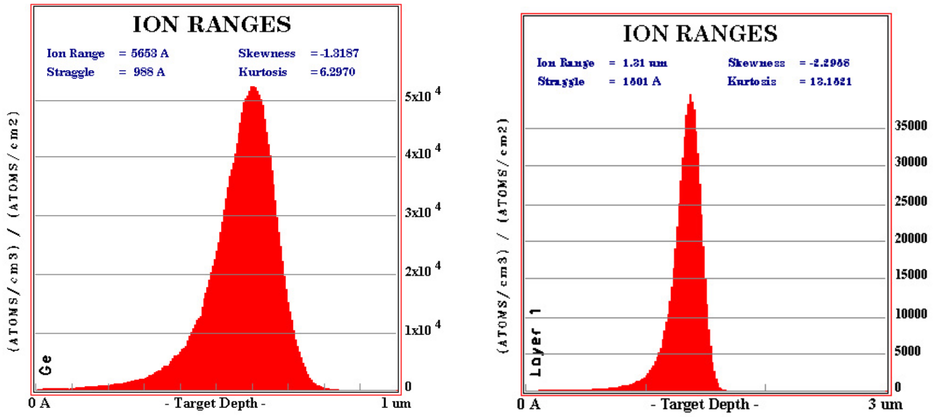

Figure 2.2. SRIM calculations of the depth profile of H^+ implanted into Ge at 80 keV (left) and 180 keV (right)

The implanted ions come to rest in the solid due to collisions with the solid lattice. The depth profile of implantation can be calculated using a free software tool called SRIM, the Stopping and Range of Ions in Matter. The SRIM calculations are based on the ion energy, and do not account for the dose. Shown in figure 2.2 are the SRIM simulations of the depth profile of H^+ in Ge for two different ion energies 80 keV and 180 keV. The peak implant position changes drastically between these two energies from 0.565 µm at 80 keV to 1.31 µm. In addition, the full width half maximum of the depth profile increases with the increase in energy.

2.2.2 Hydrogen Implantation Induced Layer Transfer

The layer transfer process is shown schematically in figure 2.3. This process enables the direct integration of two high-quality single crystal materials without misfit dislocation introduction. This method can accommodate any amount of lattice mismatch at the bond interface because the interface is incoherent rather than the forced coherency of an epitaxially grown interface. Extensive studies [32, 33, 34] have been done on the exfoliation of Si using implanted hydrogen, and more recent studies have focused on the same process in Ge [35].

First, the nature of the defect structure created upon hydrogen implantation was studied via cross-sectional transmission electron microscopy (XTEM). Two Ge wafers were implanted with 80 keV H^+ to a dose of 1×10^{17} cm $^{-2}$. One of the two samples was actively cooled during implantation to maintain the wafer at room temperature, so no in-situ an-

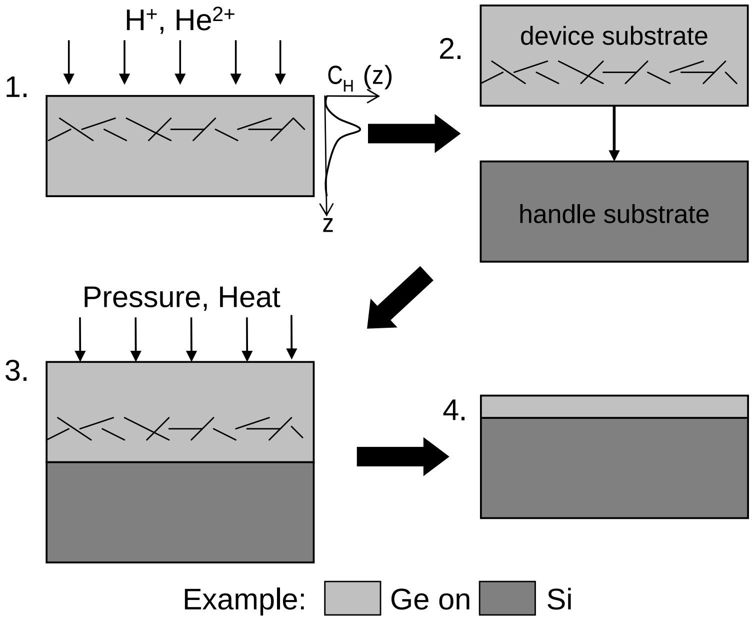

Figure 2.3. Schematic of the layer transfer process. First, the donor substrate is implanted with H^{+} and/or H^{2+}. Then both the donor and the handle substrates are cleaned and activated for bonding. Next, the two substrates are brought together, with bond initiation at either room temperature or elevated temperature. With the application of uniform pressure and heat, the implanted ions coalesce into micro-cracks within the substrate, splitting off a thin film from the donor substrate.

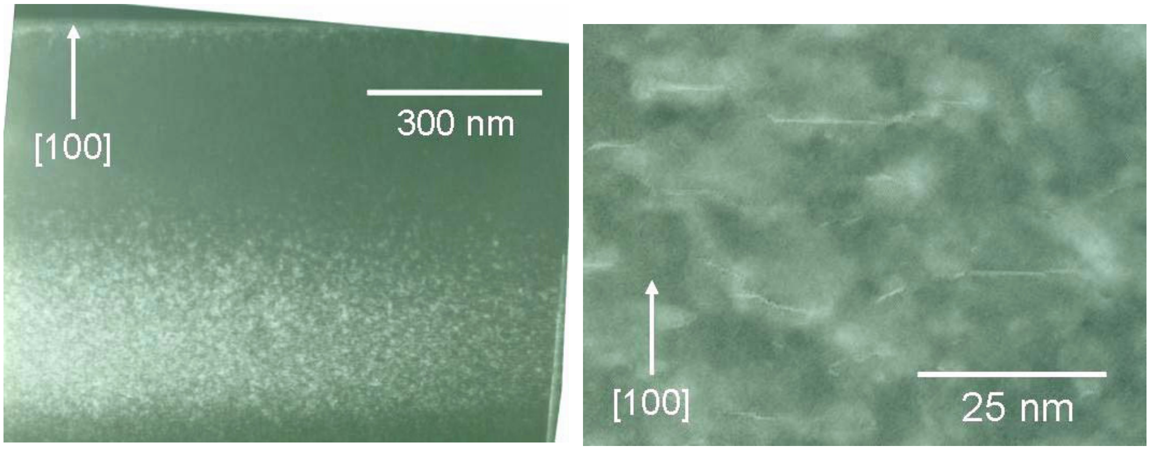

Figure 2.4. XTEM image of Ge implanted with 80 keV H^+ to a dose of 1×10^{17} cm $^{-2}$. The sample was actively cooled during implantation. The broad ion implantation induced damage layer can be clearly seen (left). Within the damaged region, (100) and some (111) platelet defects can be observed (right).

nealing occurred. The other was implanted without active cooling and then annealed for 10 minutes at 250°C. Figure 2.4 shows the sample that was actively cooled. The images show the broad implant induced damaged region. In addition, when the damaged region is viewed under higher magnification, (100) and a few (111) platelet defects can be seen. Upon annealing, these defects coalesce and form larger platelet structures as can be seen in figure 2.5. The nano-cracks that can be seen after annealing the implanted Ge are the basis for the micro-cracks that coalesce to split the film from the substrate. Atomic force microscopy (AFM) data provides further evidence for this. After implantation, the surface of the Ge is unchanged from the smooth polished surface. However, after annealing at 250°C for 10 minutes, the surface has many small bumps from the small blisters forming. After an additional 10 minutes annealing at 300°C, the surface shows clear evidence of exfoliated blisters (figure 2.6). Therefore, the exfoliation process is initiated with the formation of a dense network of micro-cracks around the peak range of the H-implant. Upon further annealing, blister rupture is observed. Rupture results in the crater-like structure found in the AFM image, most probably due to the accumulation and further increase of the internal gas pressure of the H_2 inside the blister.

Though the XTEM and AFM data provide insight into the mechanism of the layer transfer process in Ge, they do not explain the role of hydrogen in the process. Therefore,

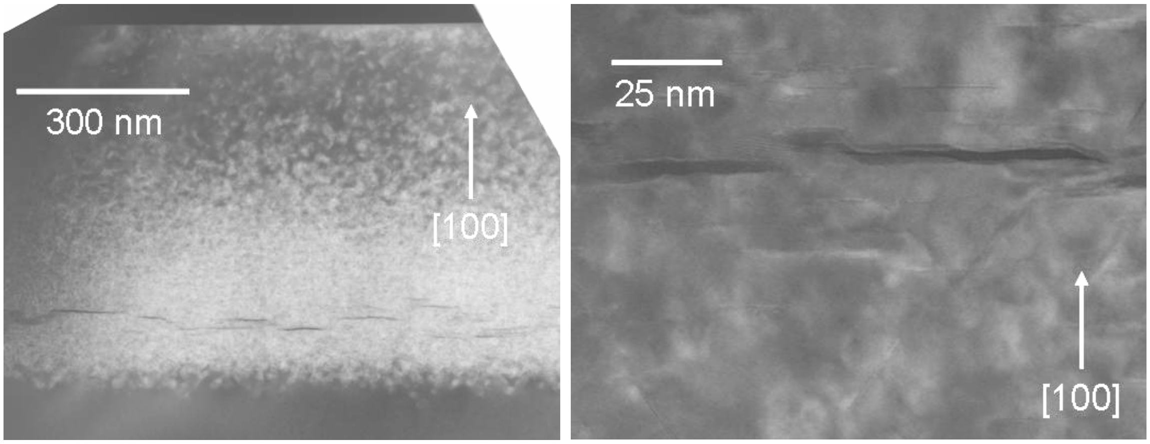

Figure 2.5. XTEM image of Ge implanted with 80 keV H^+ to a dose of 1×10^{17} cm $^{-2}$ without active cooling after a post-implantation anneal at 250°C for 10 minutes. The broad ion implantation induced damage layer can be clearly seen as can nano-cracks that are forming from the coalescence of the platelet defects(left). Within the damaged region, the nano-cracks can be seen as can remaining (100) and (111) platelet defects (right).

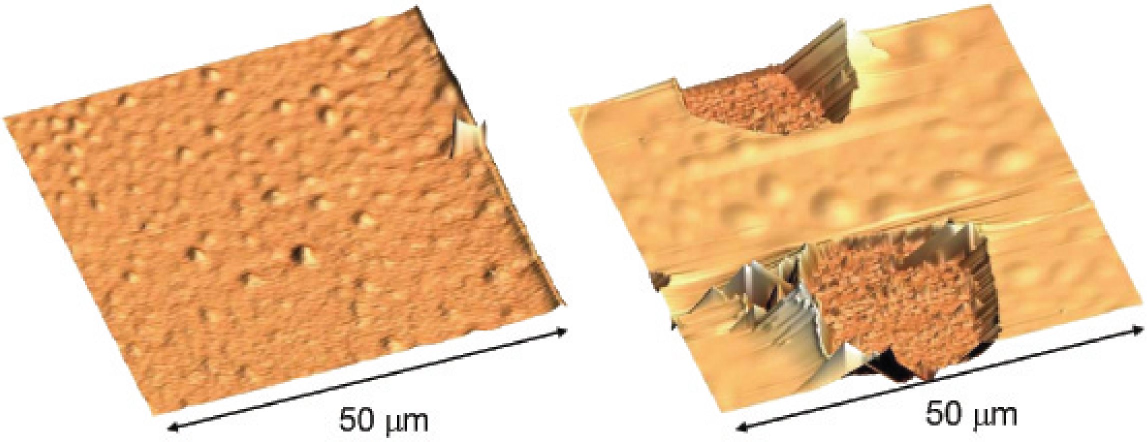

Figure 2.6. Contact-mode AFM of Ge implanted with H^+ at 80 keV to 1×10^{17} cm $^{-2}$ without active cooling after a post-implantation anneal at 250°C for 10 minutes (left). The same sample after further annealing for 10 minutes at 300°C (right).

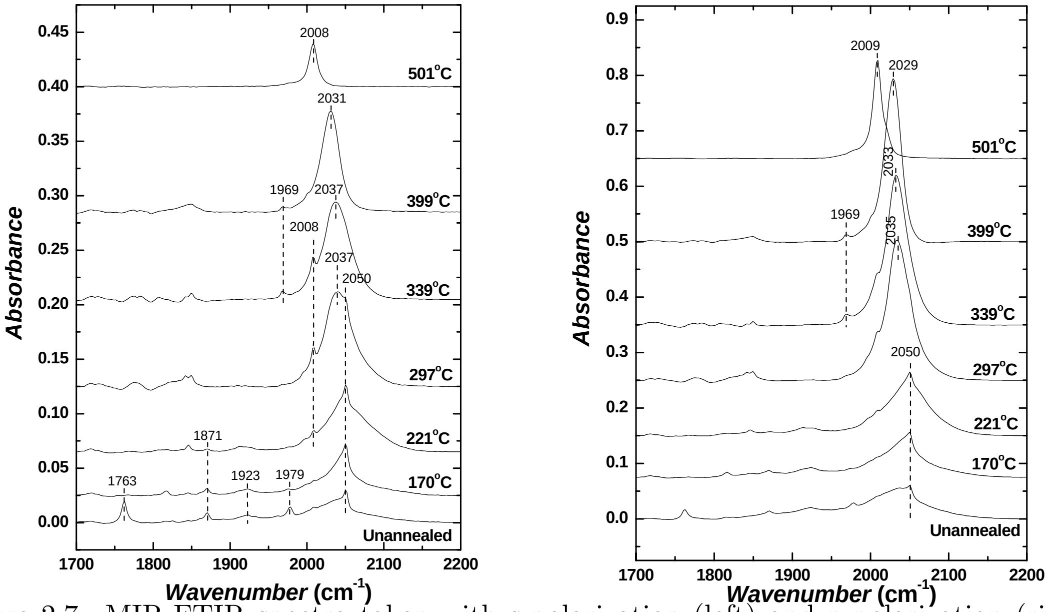

Figure 2.7. MIR-FTIR spectra taken with s-polarization (left) and p-polarization (right) for 2×10^{16} cm $^{-2}$ implanted Ge as a function of the annealing temperature

multiple internal reflection Fourier-transform infrared absorption spectroscopy (MIR-FTIR) was used to probe the chemical state of the implanted hydrogen. For FTIR analysis MIR samples were prepared measuring 15 mm by 40 mm with implantation doses of 2×10^{16} cm $^{-2}$ (too low to blister), 5×10^{16} cm $^{-2}$ (blistered above 500°C), and 1×10^{17} cm $^{-2}$ (exfoliated above 350°C). The MIR samples were then beveled at an angle of 45° on both ends to ensure efficient coupling of light in and out of the structure. All spectra were referenced to the spectrum measured for an un-implanted prism that was processed with the implanted prisms through all temperature steps. All implanted Ge pieces were annealed isochronally in a nitrogen atmosphere. Spectra were acquired following approximately 15 min isochronal annealing steps of 59°C, 131°C, 170°C, 221°C, 297°C, 339°C, 399°C, and 501°C in order to follow the evolution of the chemical state of hydrogen. The temperature of the sample while annealing was monitored with a Sensarray thermocouple instrumented wafer, accurate to 0.1°C. The three implantation doses used corresponded to three different behaviors. The temperature dependent spectra are shown in figures 2.7, 2.8, 2.9.

The medium dose sample (5×10^{16} cm $^{-2}$) is a good example to use to study the exfoliation process (figure 2.8). The implant dose is at the threshold for blistering and exfoliation, and therefore, can be used to study the process in a more controlled manner since it proceeds more slowly. As-implanted, the spectra show a broad background due to many hydrogenated

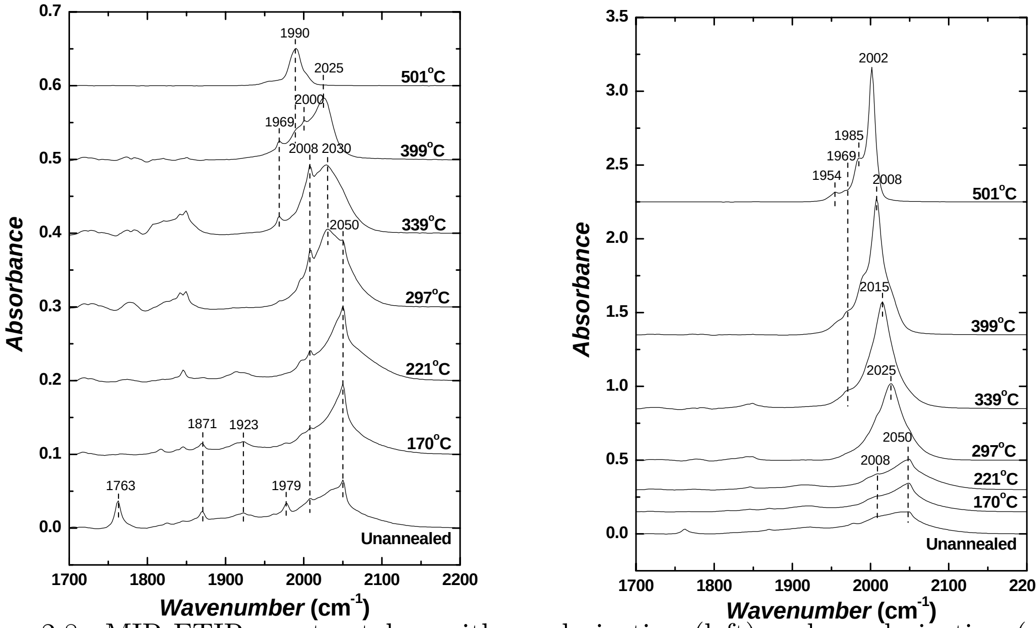

Figure 2.8. MIR-FTIR spectra taken with s-polarization (left) and p-polarization (right) for 5×10^{16} cm $^{-2}$ implanted Ge as a function of the annealing temperature

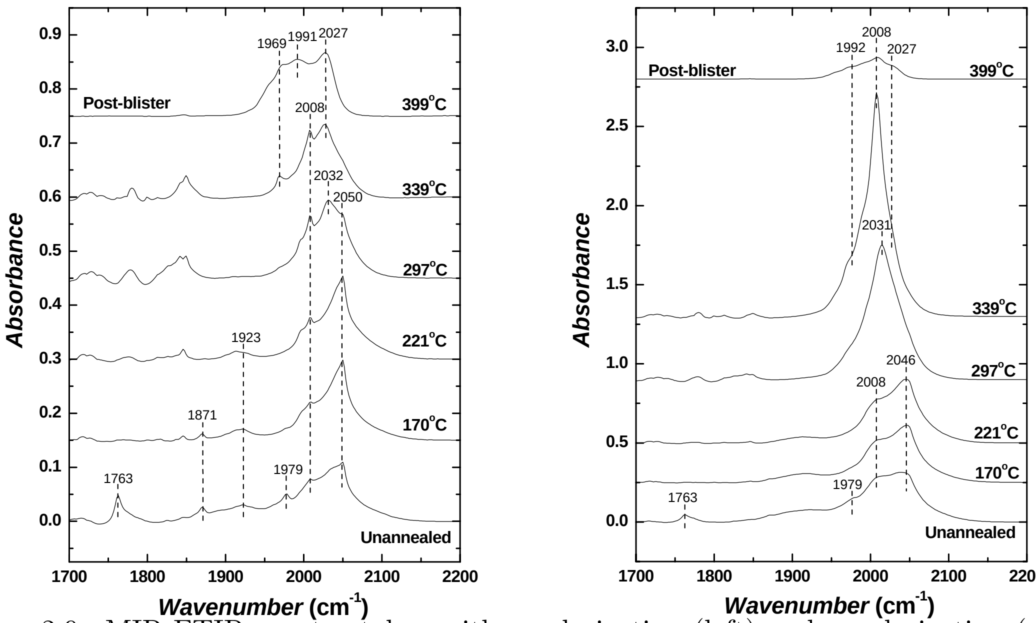

Figure 2.9. MIR-FTIR spectra taken with s-polarization (left) and p-polarization (right) for 1×10^{17} cm $^{-2}$ implanted Ge as a function of the annealing temperature

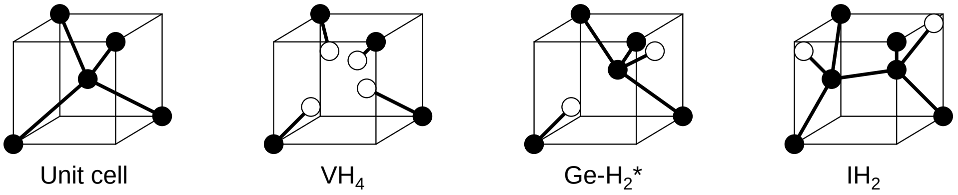

Figure 2.10. Basic schematics of the hydrogen in several configurations

vacancies, V_xH_y, and interstitial hydrogen, I_xH_y, modes. In addition, there are several distinct modes including: VH_4 (2050 cm $^{-1}$), V_xH_y (2008 cm $^{-1}$), Ge-H_2^* stretch (1978 cm $^{-1}$), and IH_2 (1870 cm $^{-1}$) (figure 2.10). Upon annealing to 170°C, there is a decrease in the broad background and a loss of the Ge-H_2^* stretch mode (1978 cm $^{-1}$). Simultaneously, there is an increase in the VH_4 mode (2050 cm $^{-1}$). Then upon further annealing to 221°C, the IH_2 mode (1870 cm $^{-1}$) is lost, while the V_xH_y mode (2008 cm $^{-1}$) has sharpened and grown. Next, at 297°C, there is further p-polarized enhancement, suggesting the presence of high index contrast in the sample. The V_xH_y mode (2008 cm $^{-1}$) continues to be enhanced and exfoliation "precursor" peaks corresponding to V_2H_6 (2026/2031 cm $^{-1}$) appear. The VH_4 (2050 cm $^{-1}$) peak is lost after annealing to 339°C. In addition, the V_xH_y mode (2008 cm $^{-1}$) continues to grow and the precursor peaks are red-shifted (2015/2029 cm $^{-1}$). Annealing to 399°C only continues the red shift of the precursor peaks (2008/2025 cm $^{-1}$) and sees a loss in the V_xH_y mode (2008 cm $^{-1}$). Finally, at 501°C, blistering has begun and the peaks at 2001/1990 cm $^{-1}$ are suggestive of (100) surface monohydrides on rough surfaces. The lower wavenumber modes correspond to (111) surface monohydrides.

These results show that the exfoliation process in Ge is very similar to that in Si. The implantation induces defects in the germanium crystal structure that trap hydrogen in the Ge-H_2^*, V_2H_6, and V_nH_{n+4} modes. After annealing, some of these modes are lost, allowing the hydrogen to diffuse to more stable modes like internal (100) and (111) surfaces. These surfaces act as the nucleation point for the nano-cracks that were observed via XTEM. As the micro-cracks appeared in XTEM, the vibrational frequencies associated with Ge(100) surface monohydride and dihydride appear in the FTIR spectra. These micro-cracks are coalescence points for H_2 and allow the internal pressure to build to a degree that causes wafer exfoliation.

2.3 Creating Ge/Si Epitaxial Templates

Ge/Si epitaxial templates were first created by my predecessor, James Zahler[10]. One of the main problems with the Ge/Si epitaxial templates was their thermal stability. Unfortunately, direct wafer bonding is the most difficult form of wafer bonding as the two bonding surfaces must be perfectly clean and atomically smooth. Any trapped particles in the bond will create voids in the interface. If any of these conditions are not met, then covalent bonds will not form between the two materials when they are annealed after bonding as other atoms contaminate the semiconductor surface. As copper[36] and palladium[37] have been shown to be very good materials for use as a bonding layer, palladium was used in the early stages of this work since it provided good thermal stability of the bond. However, MOCVD growth temperatures range from 600–750°C. At those temperatures diffusion of any metal through the Ge film is very high, and so the Pd would be inside the III-V grown layers. For this reason, alternative bonding layers were explored. We have had very good success with both amorphous Si and SiO_2.

Working with bonding layers has had an additional positive impact on our process. We are now able to show full 2" wafer layer transfer of Ge on Si. With the direct bonding work, particles often limited the transferred area, since the bonded interface provides the support necessary to force the micro-crack to expand laterally and not blister individually through the surface. In addition, with the use of a commercial bonding tool (Suss SB-6e) the success rate of our transferred films has increased to nearly 100%. Generally, every implanted Ge wafer succesfully transfers greater than 80% of the area. The exfoliation process is extremely sensitive to the conditions during ion implantation. If the wafer temperature is warmer or colder during implant, the exfoliation conditions can change significantly. Our primary vendor for ion implantation was Leonard Kroko, Inc., in Tustin, CA. Kroko does not have the capability to actively cool wafers during implant, therefore, we use a very low beam current to keep the wafer temperature down. Without active cooling or a low beam current, the doses we use would blister during implant due to internal heating. Another factor with ion implantation is deposition of material on the surface of samples. There is always a degree of surface deposition due to the implantation process. To protect the bonding surfaces from contamination, a 50 nm sacrificial SiO_2 film is sputtered onto the Ge wafers before sending it out for implant. The wafers after implant were typically discolored to a dark brown color.

The contamination could not be removed in aqueous or organic solvents (alcohols, hexanes, toluene, chloroform, and tetrahydrofuran). The contaminant layer could also inhibit SiO_2 removal during HF dip. Therefore, plasma ashing was performed to open voids in the contaminant layer to enable complete SiO_2 removal. SiO_2 was chosen as the sacrificial layer due to rapid removal in aqueous hydrofluoric acid (HF). Removal was typically achieved in 20 seconds, which ensured minimal substrate degradation.

The optimized process conditions for Ge/Si template preparation were as follows (where applicable, vendors are shown in parentheses):

1. Order Ge substrates (AXT, Umicore)
2. Order Si substrates with 300 nm thermal oxide (Silicon & Solar)
3. Sputter deposit 50 nm SiO_2 on Ge (Thin Film Concepts)
4. Implant Ge with H^+ to $1x10^{17}$ ions/cm^2 at 180 keV and 45 μA beam current (Leonard Kroko, Inc.)
5. Plasma ash the implanted Ge for 10 minutes
6. Remove the SiO_2 with a 20 s etch in 20% HF
7. Rinse in DI water
8. Spin dry
9. Sonicate both the Ge and the Si wafer in acetone for 5 minutes
10. Sonicate both the Ge and the Si wafer in methanol for 5 minutes
11. Rinse in DI water
12. Spin dry
13. Plasma activate the surfaces with 2 passes of an atmospheric nitrogen plasma at 300 W
14. Preheat the bonder to 200°C
15. Place the Si wafer on the bond platen

16. Position the flags on the wafer
17. Place the Ge wafer face-down on the flags
18. Place two pieces of carbon tape on top of the stack (they must be large enough to cover the full Ge sample size)
19. Place the 3” SiC plate on top
20. Move the platen into the bonding chamber
21. Begin the bonding recipe in the bonder

The bond recipe involves a 5 minute pause at 200°C to ensure the two wafers are at temperature. Then the center pin is lowered onto the stack and the flags are removed. Next, the top bonding plate comes down and applies a pressure of 3 MPa and the system pauses for 10 minutes. The temperature is then ramped to 250°C for 30 mintues to anneal the bond. Finally, the temperature is raised to 350°C for 30 minutes to induce exfoliation. The system then cools down slowly via radiative losses, as there is no active cooling. Finally, when the platens have cooled to less than 100°C, the top platen is removed and the sample can be unloaded. All of the cleaning and bonding steps were performed in a Class 10 cleanroom.

Initially, we made full 2” transfers, and cleaved them into quarters for post-processing and growth. However, due to the speed at which the growth platens rotate, we were losing about half of the samples we sent per growth run. Therefore, we started cleaving the implanted Ge and transferring quarter Ge wafers to full 2” Si wafers. That was the size of all our samples until the final round of growths where we wanted a high active area. There we returned to full 2” Ge on 2” Si.

2.4 Template Surface Preparation

2.4.1 Wet Chemical Etching

As seen in the previous section, the as-transferred thin film is not considered epi-ready. The ion implantation induced damage must be removed. In addition, the surface roughness must be brought below 1 nm to ensure high quality heteroepitaxy on these substrates. In an effort to develop an inexpensive and easy procedure for preparing the templates for epitaxial growth, the first technique that was explored was wet etching. The most common etchant for Ge is known as CP-4 (HNO_3:HF:CH_3COOH). It is generally used in a ratio of 1:1:1. However, it is a very fast etchant of Ge, and since the films were at most 1.4 µm, the etch rate needed retarding. Previous work by a SURF student in our lab, Darci Taylor, had shown that diluting the etchant with water seemed to make things worse (figure 2.11). Water is an anisotropic etchant of Ge, whereas CP4 is an isotropic etchant. Therefore, diluting CP4 with water would only serve to roughen the surface further. Since the acetic acid is acting as a buffer, the CP4 etch was re-examined using acetic acid as the diluent.

Before beginning the work of testing different dilutions of CP4 for removing the damaged layer and smoothing the surface roughness, a good method for comparing the surface morphology was needed. Generally, the root-mean-square (RMS) roughness is quoted when discussing surface roughness. First, the RMS roughness is actually the standard deviation of the roughness, and for very different surface morphologies the RMS value can be the same see figure 2.12. Constantoudis et al.[38] developed a quantitative way of describing the roughness of photoresist line edges using scaling and fractal concepts. Using their techniques, a Matlab routine was designed to calculate a correlation function from AFM data. From this, one can obtain the overall correlation length, ξ, and the roughness exponent, α. While Constantoudis developed this technique to better describe the line-edge roughness of photoresists, it can be applied to two-dimensional surfaces by effectively mapping the entire surface as a one dimensional line, i.e., the data from each horizontal scan is connected end to end into one large line scan. The equations correlate the distances of the various points from the average linear fit of the data at all points. The height-height correlation function $G(r)$ and the normalized autocorrelation function $R(r)$ defined at $r = md$ are defined as:

$$G(md) = \left[\frac{1}{N-m}\sum_{i=1}^{N-m}\left(\delta_{i+m}-\delta_i\right)^2\right]^{1/2} \tag{2.1}$$

$$R(md) = 1 - \left[\frac{G^2(md)}{2\sigma^2}\right] \tag{2.2}$$

Here, d is the distance between neighboring points; δ is the distance from the linear fit; N is the total number of points; and σ is the RMS roughness. From these equations, σ, ξ, and α can be obtained as shown in figure 2.13. As a check, RMS roughness was calculated and compared to the roughness obtained from the correlation length analysis.

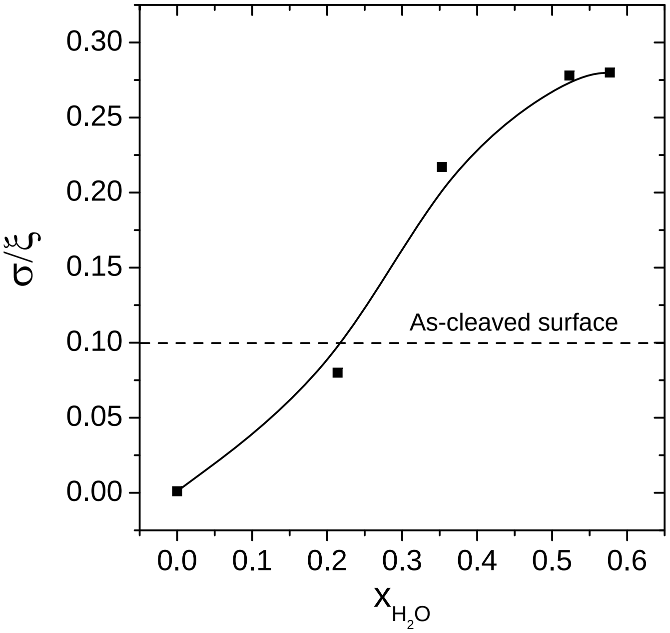

Figure 2.11. Initial work with the CP4 etch on bare Ge showing the σ/ξ value as a function of dilution with water

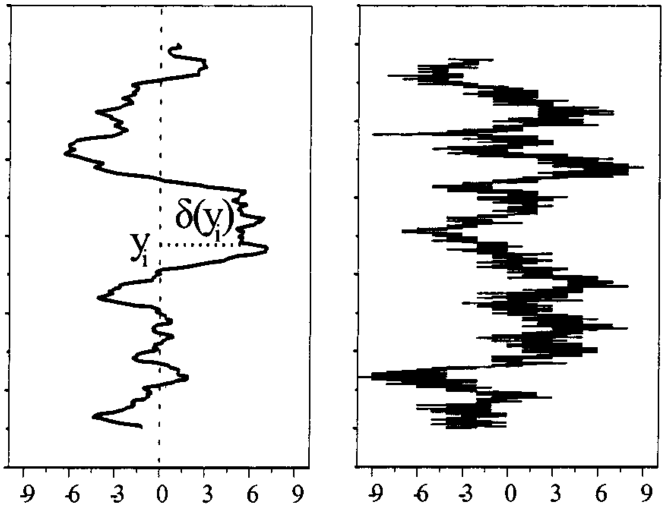

Figure 2.12. Two linescans with the same root mean square roughness value, but very different morphologies[38]

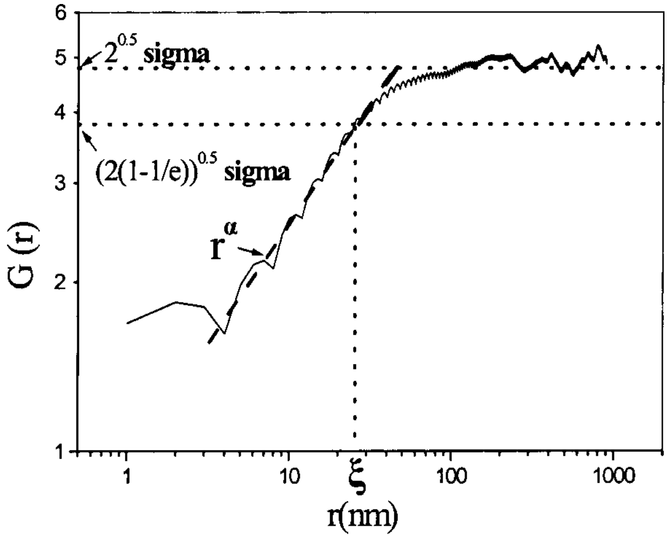

Figure 2.13. Correlation function $G(r)$ showing values σ, ξ, and α[38]

Only minor differences are observed between the two roughness values. σ/ξ provides a nice dimensionless figure of merit that incorporates the correlation length with the RMS value.

When the etching process was being developed, there was no good way to measure the etch rate. First, a computer-controlled system for creating staircase etched samples of SiO_2 was attempted with the Ge and the CP4 etch. Unfortunately, even the dilute etch solution has a significant vapor pressure, so though part of the sample was out of the etchant and the other part was immersed, both parts were etched (figure 2.14). In addition, these samples began as epi-ready Ge polished smooth surfaces. After being exposed to the etchant for 1 minute, the immersed portion had an RMS = 2.489 nm and $\sigma/\xi = 0.0313$. The portion that was above the solution had an RMS = 6.256 nm and $\sigma/\xi = 0.0138$.

In an attempt to suppress the etch solution vapor, vegetable oil was added to the top of the solution. However, the vegetable oil and the etchant reacted strongly, preventing the use of the etch solution. Since the staircase etch did not work, a physical mask using paraffin wax was attempted. Unfortunately, the wax was not fully resistant to the etch solution, and the area under the wax was etched again. However, the lines differentiating the waxed area from the exposed area was clearer with these samples than the staircase etch samples, so an approximate etch rate was measured for several dilutions of CP4 in an ice bath and at room temperature. The results can be seen in figure 2.15. Given these results, the 1:1:20 and 1:2:30 etch solutions were then tested on Ge donor wafers (bulk Ge samples that had been exfoliated and therefore showed mirror-image surfaces to the epitaxial templates). The

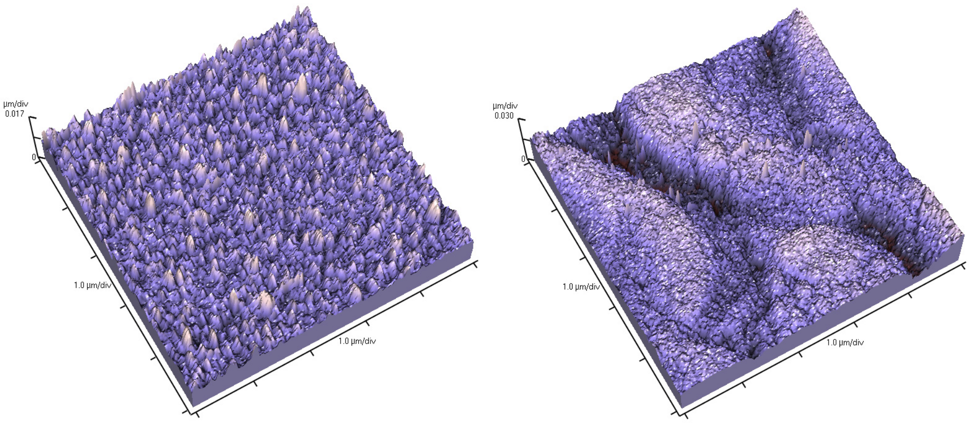

(a) (b)

Figure 2.14. Contact mode AFM scans of an epi-ready Ge sample immersed in (a) and above (b) 1:1:1 CP4 for 1 minute

donor wafer etch results showed lower RMS and σ/ξ values for the same amount of time in the 1:2:30 etch solution as compared to the 1:1:20 solution.

When etching epitaxial templates, the thickness of the Ge layer is simple to measure using spectroscopic ellipsometry. However, as the bonded templates were precious samples, we did not use them in the initial etch experiments. Using Ge/Si templates fabricated with Pd as a bonding layer, the etch rate and efficacy were tested. The etch rate was obtained by fitting spectroscopic ellipsometry data from 250–2300 nm with model for the optical properties of each of the materials in the ellipsometer software (figure 2.16). A Sentech SE850 ellipsometer with SpectraRay II software was used for this work. From data gathered with ellipsometry of the Ge/Pd/Si epitaxial templates, the etch rate of the 1:2:30 solution was approximated at 9.5 Å/s.

The AFM data for these samples is shown in figure 2.17. The RMS roughness was lower with prolonged etch time, as was the σ/ξ value. Next, the surfaces need to be tested in growth, as the RMS roughness is half the as-transferred value, but it is still about an order of magnitude higher than epi-ready polished substrates.

2.4.2 Epitaxial Growth and CMP

Ge homoepitaxy was explored as an option for further improving the surface morphology of the epitaxial templates. In addition, it was used as an in-house measure of whether the wet etch was achieving the necessary removal of the ion implantation induced defects as well as

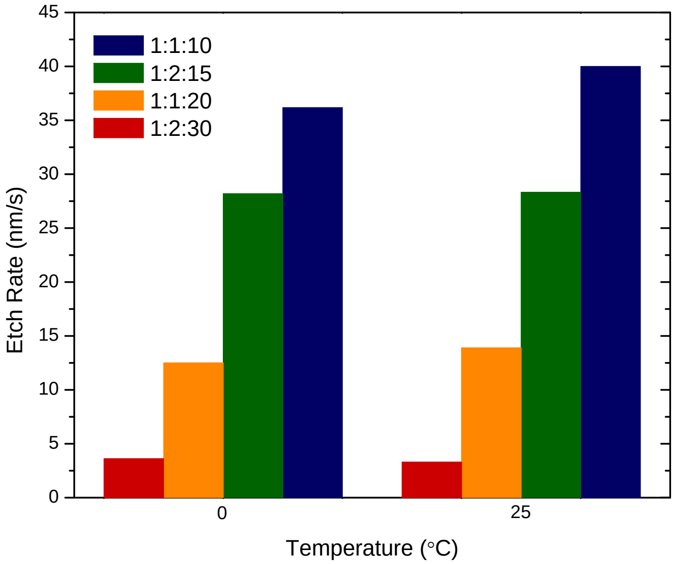

Figure 2.15. Etch rate of several CP4 dilutions in an ice bath and at room temperature

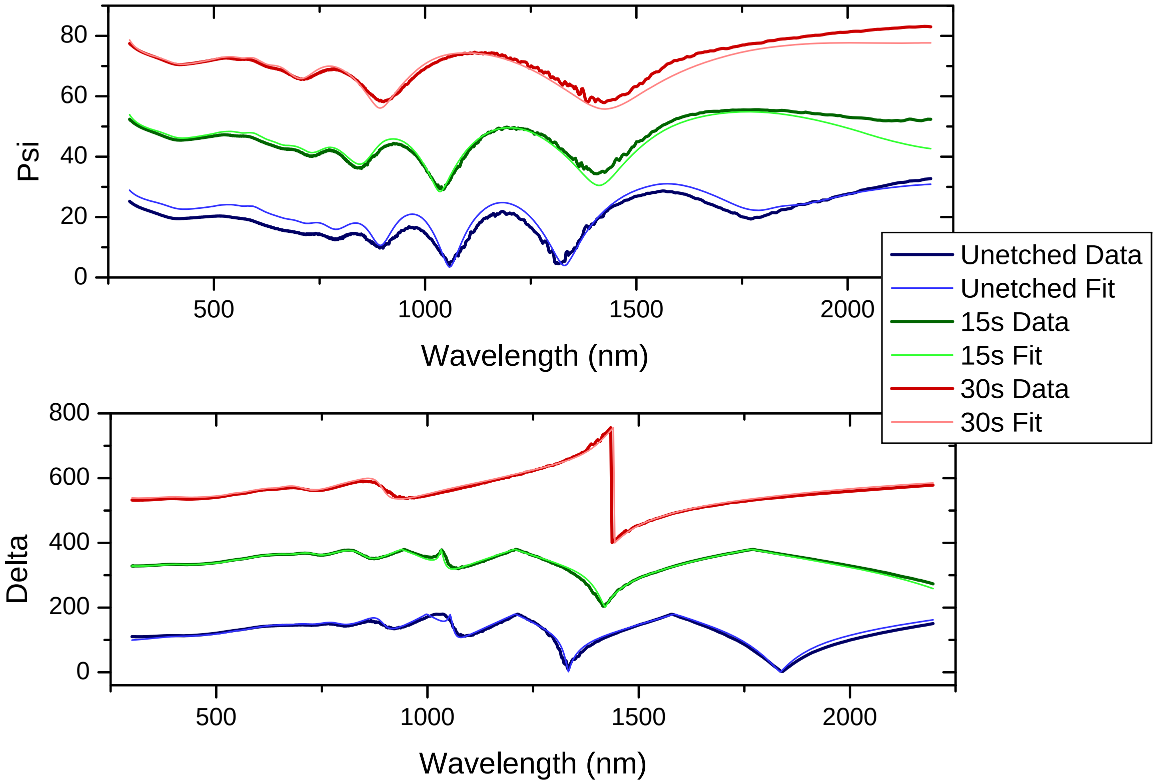

Figure 2.16. Ellipsometry data and fits for a Ge/Pd/Si epitaxial template etched for 0 s, 15 s, and 30 s; corresponding to Ge layer thicknesses of 531 nm, 395 nm, and 229 nm, respectively. The curves for the 15 s etch and the 30 s etch have been shifted up for clarity.

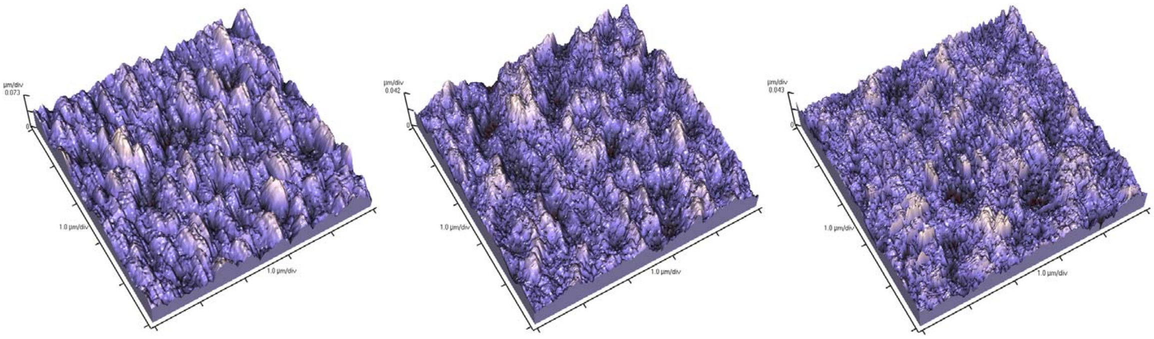

(a) Unetched
RMS = 19.6 nm
σ/ξ = 0.120

(b) 15s Wet Etch
RMS = 10.8 nm
σ/ξ = 0.0608

(c) 30s Wet etch
RMS = 9.1 nm
σ/ξ = 0.0575

Figure 2.17. Contact mode AFM scans of a Ge/Pd/Si epitaxial template

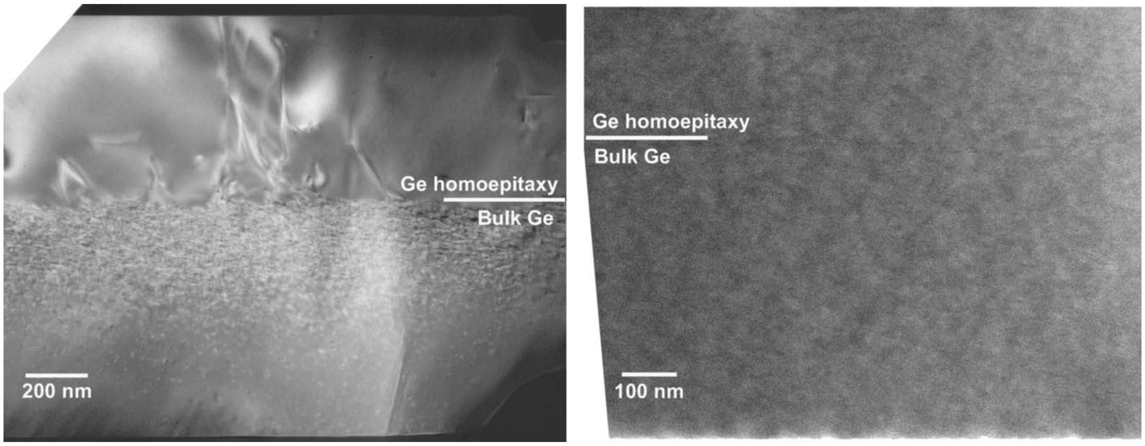

Figure 2.18. XTEM of two Ge epitaxial templates with Ge homoepitaxy layers. One sample is as-transferred (left); the other has been treated with a 30 s wet etch (right).

reducing the surface roughness. Figure 2.18 shows a comparison between an as-transferred Ge epitaxial template with Ge homoepitaxy and a sample with a 30 s wet etch. The as-transferred sample shows a high defect density in the epitaxial layer, primarily coming from propagation of implant induced defects. However, the wet etched sample shows very high quality Ge homoepitaxy.

The surface morphology of the Ge/Si samples changes with Ge homoepitaxy. Shown in figure 2.19 are AFM scans of the three surface morphologies. Epitaxial templates were prepared with these three methods and sent to our collaborators at Spectrolab for GaAs and GaInP double heterostructure growth (figure 2.20). Double heterostructures were chosen for the first round of growths due to the simple layer structure. In addition, the quality of double heterostructures can be readily assessed via photoluminescence measurements.

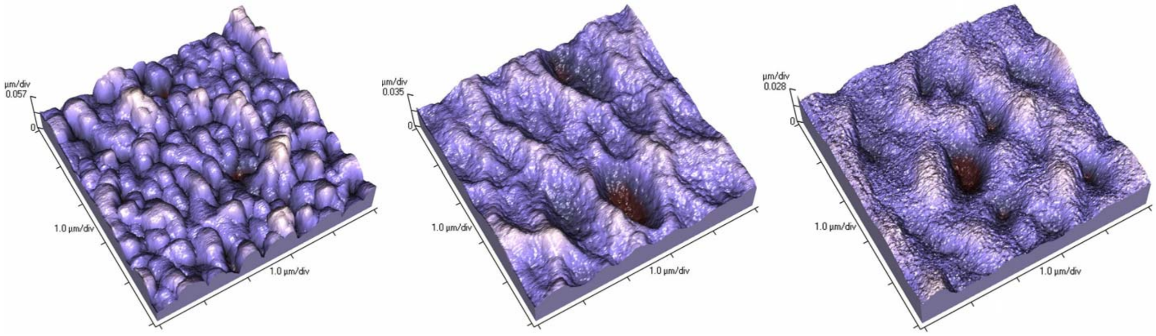

(a) Unetched
RMS = 20.47 nm
σ/ξ = 0.106

(b) 30s Wet Etch
RMS = 9.45 nm
σ/ξ = 0.0323

(c) Wet etch + Ge homoepitaxy
RMS = 7.66 nm
σ/ξ = 0.0246

Figure 2.19. Contact mode AFM of the three surface morphologies corresponding to three different preparations

The grown structures were evaluated for growth quality by photoluminescence spectrum mapping (figure 2.21,2.22), minority carrier lifetime (table 2.1), and cross-sectional TEM (figure 2.23). Unfortunately, we discovered in the XTEM work that there was a problem with the tunnel junction transition during growth of the GaInP double heterostructures that dominated the performance of our devices (figure 2.24). Therefore, the different surface preparations were compared using the XTEM data and lifetime data. The surfaces prepared with Ge homoepitaxy did not show marked improvement in defect density compared to the wet etch only samples, so homoepitaxy was removed from our template preparation process. As the method for depositing the homoepitaxy was by molecular beam epitaxy under ultra-high vacuum, it also is not a cost effective process. In addition, the epitaxial template used without any surface treatment showed an expected increase in defect density compared with those that were treated; we eliminated untreated surfaces from our options. Abbreviations: TL = transferred layer, DW = donor wafer, CIT = California Institute of Technology, SL = Spectrolab.

From the previous work, the 30 s etch condition was chosen. For the next round of double heterostructure growths, we added several “control” samples. To isolate the effects of surface morphology from strain induced by coefficient of thermal expansion mismatch, the donor Ge wafers that produced the epitaxial templates were processed using the same surface preparation. Also, an epi-ready Ge sample was wet etched and included in the growth run to understand whether the etch process itself was contributing to reduced device quality. After the growths at Spectrolab, the structures were tested with photoluminescence

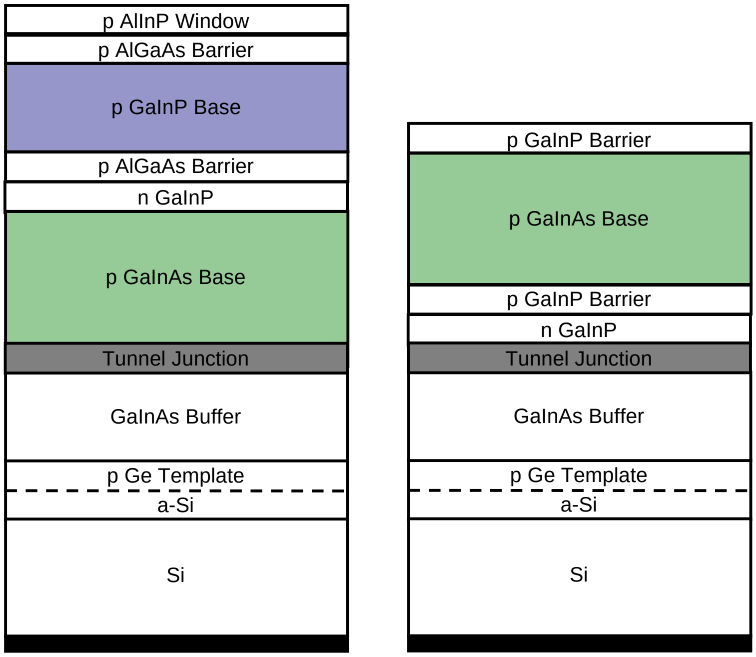

Figure 2.20. Schematic of the GaInP (left) and GaAs (right) double heterostructures grown by Spectrolab

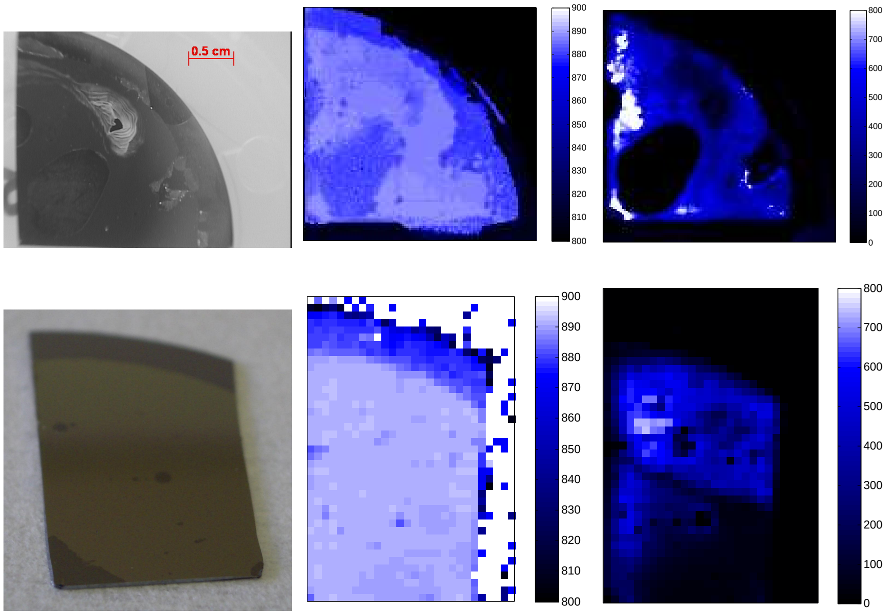

Figure 2.21. Optical images (left), peak photoluminescence wavelength maps (middle), and peak photoluminescence wavelength intensity maps (right) for GaAs DH on Ge/Si epitaxial templates prepared with 15 s etch plus 200 nm homoepitaxy (top) and 30 s etch only (bottom)

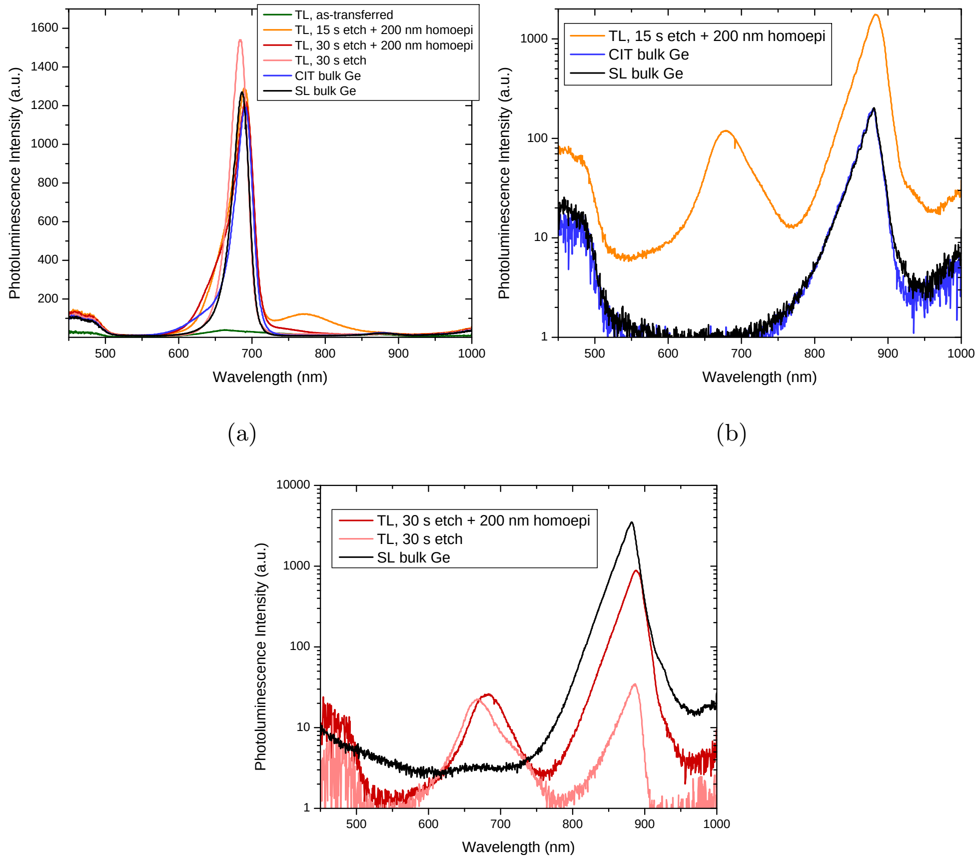

(a)

(b)

(c)

Figure 2.22. Photoluminescence spectra corresponding to the maximum intensity peak from each sample. The GaAs DH data is plotted in two separate graphs as they correspond to two different growth runs (3 samples were lost in the reactor in each run). The control data corresponding to the 15 s etch plus 200 nm homoepitaxy appears lower in intensity because the signal was saturating the detector when the same experimental set up was used for the control as for the transferred layer, so the slits on the detector were closed significantly to reach a signal that would not saturate.

Table 2.1. Minority carrier lifetime measurements from time-resolved photoluminescence performed at NREL by Wyatt Metzger

GaInAs DH sample	Lifetime (ns)	Control Lifetime (ns)
15s etch + homoepi	0.273	188
30s etch + homoepi	0.371	104
30s etch	1.02	104

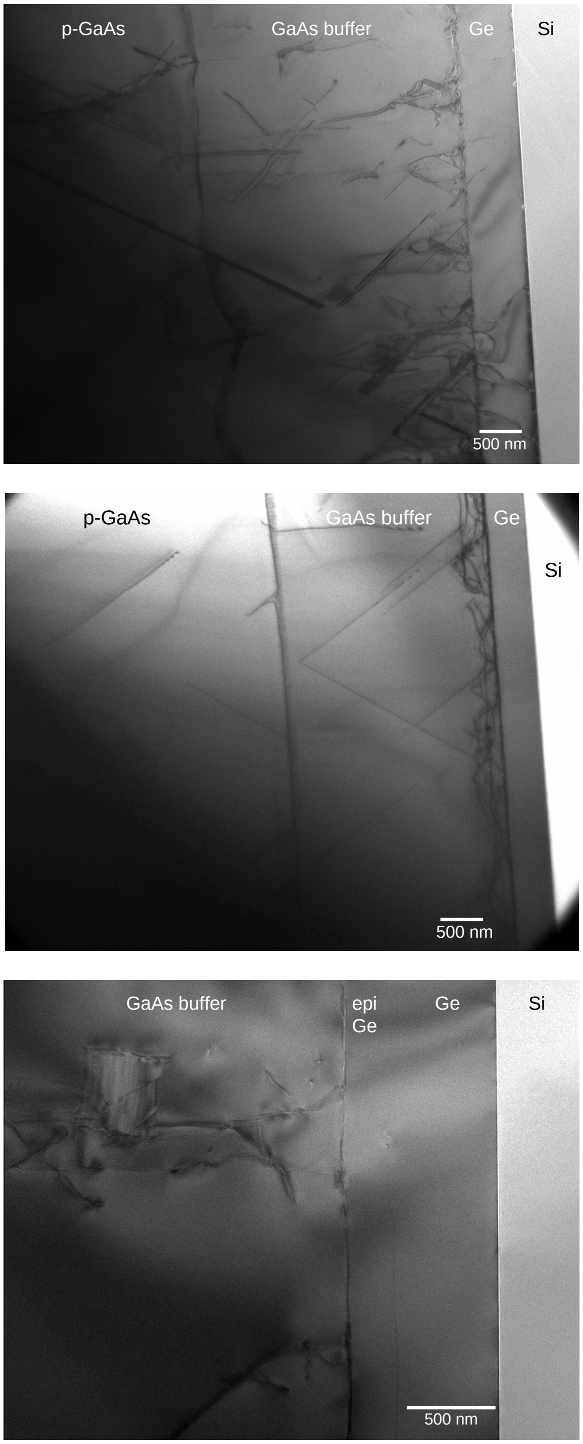

Figure 2.23. Representative XTEM of epitaxial templates after growth of GaInP double heterostructures corresponding to as-transferred (top), 30 s wet etch (middle), and 30 s wet etch plus 200 nm Ge homoepitaxy (bottom)

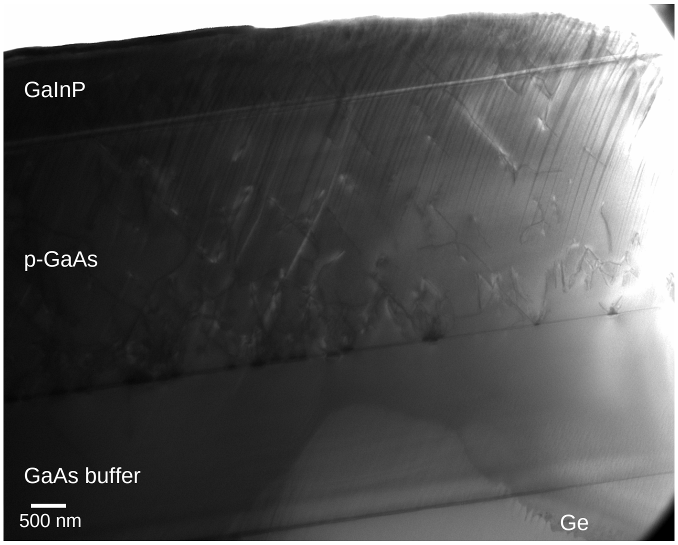

Figure 2.24. XTEM image of the Spectrolab bulk Ge control sample from the GaInP DH growth, showing a large density of defects nucleating at the tunnel junction transition

Table 2.2. Minority carrier lifetime measurements from time-resolved photoluminescence performed at NREL by Wyatt Metzger

Sample	GaInP DH Lifetime (ns)	GaAs DH Lifetime (ns)
Control	4.78	112
Epi-ready + Wet Etch	1.87	85.6
Ge/Si Wet Etched	1.89	0.124
Donor Wet Etched	0.799	0.104

mapping (figure 2.25, 2.26) and lifetime (table 2.2) measurements.

From these results, it is clear that GaInP is less sensitive to surface preparation than GaAs. GaInP double heterostructures show uniform emission over large template areas that is only an order of magnitude lower in intensity than the control substrates. The lifetimes calculated from time-resolved photoluminescence measurements are approximately one-fifth of the controls. The GaAs double heterostructures show uniform emission over large template areas that is significantly lower in intensity than the control substrates. The lifetimes calculated from time-resolved photoluminescence measurements are low, but approached 1 ns.

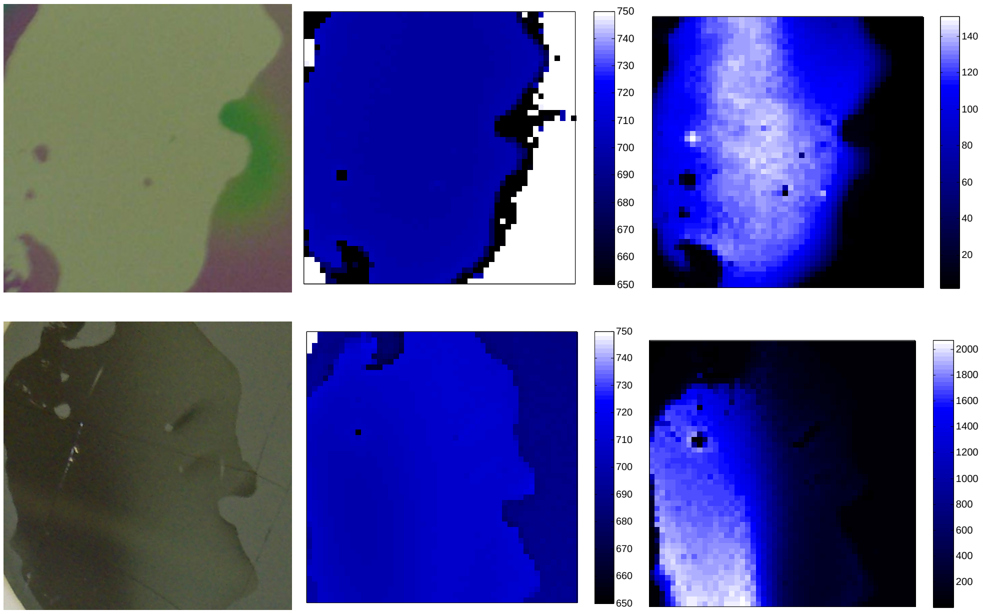

Figure 2.25. Optical images (left), peak photoluminescence wavelength maps (middle), and peak photoluminescence wavelength intensity maps (right) for GaInP DH on Ge/Si epitaxial templates prepared with 30 s etch (top) and on Ge donor wafer perpared with 30 s etch (bottom)

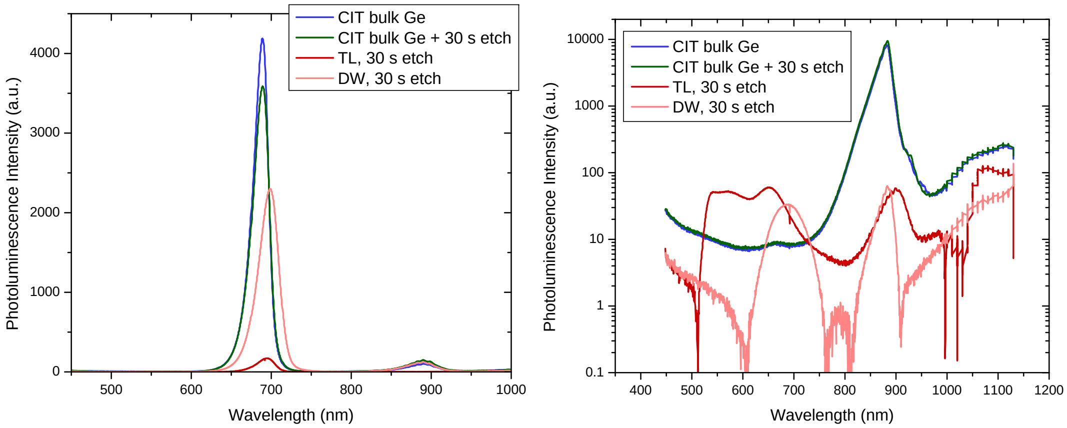

(a) (b)

Figure 2.26. Photoluminescence spectra corresponding to the maximum intensity peak from each sample

TEM results show many defects initiating at the epitaxial template surface. To further improve the surface morphology, chemical mechanical polishing (CMP) was explored. Early work by James Zahler with polishing was unsuccessful due to a weak bond strength in the epitaxial templates. However, the bond strength of the samples prepared above was much higher, so CMP was expected to significantly reduce surface roughness and defects. A Logitech PM5 polisher with PP5 jig was used to polish samples. Logitech proprietary silica slurry SF-1 was used, as recommended by Logitech for polishing Ge. Initial CMP experiments were performed using donor wafers cleaved into ~1 cm ^{2} samples. These samples were mounted with wax onto a 3" diameter glass polishing plate. It was found that after over an hour of polishing, the surface roughness could be reduced to approximately 2 nm. To reduce polishing time the samples were wet etched as described above to remove most of the damaged layer. The wet etch also provided an initial surface roughness reduction. The combined wet etch and CMP resulted in <1 nm surface roughness within approximately 2 minutes of polishing.

While surface roughness abatement had been achieved, material removal rate was not known. The removal rate was investigated by milling small squares (50 μm×50 μm) into the surface using a focused ion beam instrument (FEI Nova 600). Trench depth was measured using a profilometer before and after polishing. Unfortunately, the data was extremely inconsistent. It appeared the slurry was being trapped in the trenches and polishing due to the mixing of the slurry particles. As alternative methods failed, transferred films were used to determine material removal. The initial test samples were substrates with relatively poor layer transfer (~75% or less transferred). The substrates were 1/4 Ge wafers on 2" Si. The polishing rate seemed to slow drastically and the surface roughness became difficult to reduce below 1 nm. In addition, the samples showed signs of being ripped from the sharp corner of each 1/4 wafer. The jig downforce was calculated based on the approximate area of Ge in contact. Therefore, differences in polish rate must be due to edge/corner effects. To minimize edge and corner artifacts, full 2" Ge on 2" Si samples were tested. Film damage was significantly reduced; however, the etch/polish rate also decreased.

The optimum process for epitaxial template surface preparation was to use full 2" Ge on 2" Si with 30 s wet etch in dilute CP4 (1:2:30) to remove ion implantation induced damage, followed by a touch polish on the polisher at 45 rpm, 100 g downforce for 5 minutes. After polishing, residual slurry was removed from the surface with a CO_2 Sno-Gun. The final surface has an RMS = 0.459 nm and $\sigma/\xi = 0.00239$.

2.5 Conclusion

In this chapter, the process for creating thermally stable Ge/Si epitaxial templates was described. In addition, the importance of surface preparation was demonstrated through the performance and quality of Ge homoepitaxy grown using these templates as well as through GaAs and GaInP double heterostructures. Heteroepitaxial growth was significantly more sensitive to surface morphology than homoepitaxial growth. The primary reason for this sensitivity is the polarity of the atoms in III-V materials. Anti-phase domains and defects propagate easily when the surface is not ideal for growth. For example, in growth of III-V materials on bulk Ge, the miscut of the wafer can play an important role in the final composition and ordering of the films. Therefore, the surface morphology of our epitaxial templates must closely mimic bulk Ge.

Chapter 3

Cell Modeling

3.1 Introduction

In this chapter, the techniques used for modeling the performance of the proposed four junction cell design are described. The most common method for modeling multijunction solar cell designs uses Detailed Balance calculations developed by Shockley and Quiesser[39, 40, 41]. Detailed Balance calculations assume that cells are at the radiative limit, where absorbed light radiation is the only source of parasitic loss. They assumed every photon with energy greater than or equal to the band gap energy is absorbed and produces a single electron hole pair. In this manner, all other aspects of solar cell performance were ignored, and the theoretical efficiency limit was obtained. This is a good method when a rough comparison between different research approaches is needed. For example, when deciding which four band gaps to pursue for the four junction design, Detailed Balance calculations were used[10]. These calculations provide an upper thermodynamic limit to the performance of any solar cell. Detailed balance calculations provide the thermodynamic limit to efficiency of solar cells as Carnot cycle calculations do for heat engines. However, as an upper bound on efficiency, these calculations do not provide insight into the realistic performance of these devices nor into important material parameters.

However, when looking to understand material properties that limit the performance of real photovoltaic devices, it would be useful to have a model that incorporates their effects. In particular, we would like to understand the effect of individual cell material quality on overall device performance. For example, could one cell be of lower material quality without significantly reducing overall performance? Conversely, could one material significantly reduce performance with slightly lower material quality? Minority carrier diffusion length was used as a proxy for material quality (high quality materials typically exhibit long diffusion lengths). In addition, a quantitative understanding of the effects of series resistance under concentration, as well as alternative electrical connections, was desired. Models of single junction silicon solar cells have been developed with good models for sources of non-ideality. The most commonly used of these are AMPS[42] and PC1D[43]. These models have been extended over time to include more sophisticated understandings of the physics involved in silicon solar cells. Multijunction solar cell modeling is complicated by requiring current matching between cells in the device. This is due to the cells being connected in series. In addition, the wealth of experimental optical and physical data available for silicon is not available for many of the III-V materials of interest. For these reasons, great interest in realistic models of III-V multijunction solar cells has emerged. Several models have been created to fill this void: the commercial software from Silvaco, ATLAS[44], has been shown to be effective in modeling two-dimensional photogeneration and providing similar current-voltage (IV) characteristics to experimental solar cells. In addition, the model Syracuse[45] has been developed to effectively model the performance of any III-V multijunction solar cell anywhere in the world. The model includes an extensive library of spectral irradiance data (both experimental and theoretical). However, neither of these models allows for device structure optimization. With current matching limitations, the thickness of each subcell is extremely important to ensure optimum performance. A group in Kuwait has developed a model[46] that allows for optimization of various parameters of the device, although many approximations were introduced to emulate experimentally observed behavior.

3.2 Models Using the Depletion Approximation

3.2.1 The Equations

The current density, $\vec{J}$, in a photovoltaic device can be found by solving the drift/diffusion equations, continuity, and Gauss' Law simultaneously[47].

$$\vec{J} = \vec{J_n} + \vec{J_p} \tag{3.1}$$

where $\vec{J_n}$ and $\vec{J_p}$ are the current densities in the n- and p-type regions.
From Diffusion/Drift:

$$\vec{J_n} = qn\mu_n\vec{\xi} + qD_n\vec{\nabla}n \tag{3.2}$$

$$\vec{J_p} = qp\mu_p\vec{\xi} - qD_p\vec{\nabla}p \tag{3.3}$$

where q is electronic charge, n and p are the electron and hole concentrations, $\mu_{n/p}$ is the carrier mobility, $\vec{\xi}$ is the electric field, and $D_{n/p}$ is carrier diffusivity.

From continuity:

$$\frac{\partial n}{\partial t} - \vec{\nabla} \cdot \frac{\vec{J_n}}{q} = G_n - U_n \tag{3.4}$$

$$\frac{\partial p}{\partial t} + \vec{\nabla} \cdot \frac{\vec{J_p}}{q} = G_p - U_p \tag{3.5}$$

where $G_{n/p}$ is carrier generation and $U_{n/p}$ is carrier recombination. The generation term can be solved by assuming that each absorbed photon creates an electron-hole pair, $G_n = G_p$ and assumming exponential light absorption.

$$G(\lambda, x) = \alpha(\lambda)\,\Gamma_o(\lambda)\exp(-\alpha(\lambda)\,x) \tag{3.6}$$

where $\alpha(\lambda)$ is the absorption coefficient and $\Gamma_o(\lambda)$ is the solar flux hitting the top of the cell. Also, assuming that charge neutrality must hold, the recombination term becomes:

$$U_n = U_p = \frac{n - n_o}{\tau_n} = \frac{p - p_o}{\tau_p} \tag{3.7}$$

where n_o and p_o are the thermal equilibrium carrier concentrations and $\tau_{n/p}$ is the minority carrier lifetime.

From Gauss' Law:

$$\vec{\nabla} \cdot \vec{\xi} = \frac{\rho}{\epsilon} \tag{3.8}$$

where ρ is the net charge and ϵ is the static dielectric constant.

As written, these differential equations have no known analytical solution and are difficult to solve using numerical methods. A tractable solution can be obtained by invoking the depletion approximation. The depletion approximation states that there is a finite size depletion region in a pn junction. Outside of the depletion region, the overall charge state is neutral, otherwise known as the quasi-neutral regions. Inside the depletion region, the charge is non-neutral. The transition between charge neutrality and non-neutrality is assumed to be a step function. Though the depletion approximation helps make the differential equations more workable, more simplifying assumptions were required to get an analytical solution to the transport equations. The first was to assume the junction doping profile was abrupt. The second was to assume depletion region recombination was caused by

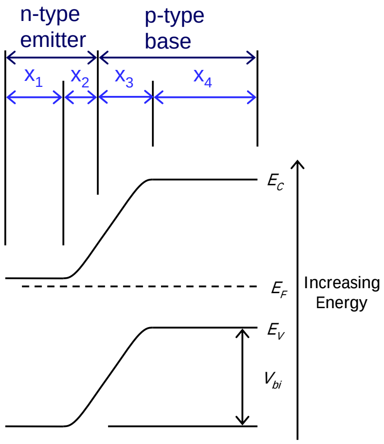

Figure 3.1. A schematic of the band diagram of a cell showing the four different regions of the device

a single trap at mid-gap level using the model developed by Sah, Noyce, and Shockley[48]. Recombination outside of the depletion region is described using the Shockley-Read-Hall recombination model[49]. Finally, one-dimensional carrier transport was assumed.

The emitter layer was assumed to be n-type, while the base was p-type. Each cell is divided into four regions, the quasi-neutral region of the emitter (thickness = x_1), the depletion region of the emitter (thickness = x_2), the depletion region of the base (thickness = x_3), and the quasi-neutral region of the base (thickness = x_4). The emitter has doping N_D and the base has N_A. Shown in figure 3.1 is a schematic drawing of the cell design along with the band diagram.

First, the thicknesses of the four regions of the cell must be defined along with the built-in voltage. The total emitter thickness is assumed fixed, as is the base thickness. However, the depletion region thickness must be calculated as it is a function of the applied bias, V. In order to do this, continuity of the electric field is applied. Since

$$\frac{d\xi}{dx} = -\frac{d^2V}{dx^2} = \frac{q}{\epsilon}N_D \tag{3.9}$$

$$\frac{d\xi}{dx} = -\frac{d^2V}{dx^2} = \frac{q}{\epsilon}N_A \tag{3.10}$$

then

$$\xi\left(x\right) = \frac{qN_D\left(x - x_1\right)}{\epsilon} \tag{3.11}$$

$$\xi\left(x\right) = -\frac{qN_A\left(x - x_1 - x_2 - x_3\right)}{\epsilon} \tag{3.12}$$

ξ must be continuous at the junction ($x = x_1 + x_2$); therefore,

$$N_Dx_2 = N_Ax_3 \tag{3.13}$$

Also,

$$V_{bi} - V = \frac{qN_Ax_3^2}{2\epsilon} + \frac{qN_Dx_2^2}{2\epsilon} \tag{3.14}$$

where

$$V_{bi} = \frac{kT}{q}log\left(\frac{N_AN_D}{n_i^2}\right) \tag{3.15}$$

where n_i is the intrinsic carrier concentration. Substituting for x_2 yields:

$$V_{bi} - V = \frac{qN_A}{2N_D}x_3^2\left[\frac{N_D + N_A}{\epsilon}\right] \tag{3.16}$$

Therefore,

$$x_2\left(V\right) = \sqrt{\left(\frac{2N_A\epsilon\left(V_{bi} - V\right)}{qN_D\left(N_D + N_A\right)}\right)} \tag{3.17}$$

$$x_3\left(V\right) = \sqrt{\left(\frac{2N_D\epsilon\left(V_{bi} - V\right)}{qN_A\left(N_D + N_A\right)}\right)} \tag{3.18}$$

In the quasi-neutral regions (x_1 and x_4), the electric field is assumed to be zero. Therefore, by using the diffusion/drift equations with the continuity equations, gives the inhomogeneous Helmholtz equation of the form (shown for the p-type base):

$$\frac{d^2n'}{dx^2} - \frac{n'}{L_n^2} = -\frac{\alpha\Gamma_o}{D_n}\exp\left(-\alpha x\right) \tag{3.19}$$

where $n' = n_p - n_{p0}$, $L_{n/p}$ is the diffusion length, and $L_{n/p}^2 = D_{n/p}\tau_{n/p}$, with boundary conditions at $x = 0$,

$$n' = n_{p0}\left(\exp\left(\frac{qV}{k_BT}\right) - 1\right) \tag{3.20}$$

and at $x = x_4$,

$$S_n n' = -D_n \frac{dn'}{dx} \tag{3.21}$$

where k_B is Boltzmann's constant, T is temperature, and $S_{n/p}$ is the surface recombination velocity. This equation gives a solution of the form:

$$n'(x) = A \exp\left(\frac{x}{L_n}\right) + B \exp\left(-\frac{x}{L_n}\right) + C \exp(-\alpha x) \tag{3.22}$$

By substituting this solution into the original differential equation, C is shown to be:

$$C = \frac{\alpha \Gamma_o}{D_n \left(\alpha^2 - L_n^{-2}\right)} = \frac{\Gamma_o}{\alpha D_n \left(1 - \alpha^{-2} L_n^{-2}\right)} \tag{3.23}$$

The constants of integration can be found using the boundary conditions, and the solution can then be split into two parts: the light current

$$\begin{aligned} J_l^p = &-\left(\frac{q\Gamma_0 \exp\left(-\alpha\left(x_1 + x_2 + x_3\right)\right)}{1 - \alpha^{-2} L_p^{-2}}\right) \times \\ &\times\left\{1 - \left(\frac{1}{\alpha L_n}\right)\left[\frac{\left(S_n L_n / D_n\right)\left[\cosh\left(x_4/L_n\right) - \exp\left(-\alpha x_4\right)\right] + \left(1/\alpha D_n\right)\sinh\left(x_4/L_n\right) + \alpha L_n \exp\left(-\alpha x_4\right)}{\left(S_n L_n / D_n\right)\sinh\left(x_4/L_n\right) + \cosh\left(x_4/L_n\right)}\right]\right\} \end{aligned} \tag{3.24}$$

and the dark current

$$J_0^p = -\left(\frac{qD_n}{L_n}\right) n_0 \left(\frac{\left(S_n L_n / D_n\right)\cosh\left(x_4/L_n\right) + \sinh\left(x_4/L_n\right)}{\left(S_n L_n / D_n\right)\sinh\left(x_4/L_n\right) + \cosh\left(x_4/L_n\right)}\right) \tag{3.25}$$

Similarly for the n-type quasi-neutral region, the dark current is:

$$J_0^n = -\left(\frac{qD_p}{L_p}\right) p_0 \left(\frac{\left(S_p L_p / D_p\right)\cosh\left(x_1/L_p\right) + \sinh\left(x_1/L_p\right)}{\left(S_p L_p / D_p\right)\sinh\left(x_1/L_p\right) + \cosh\left(x_1/L_p\right)}\right) \tag{3.26}$$

and the light current is:

$$J_l^n = -\left(\frac{q\Gamma_0}{1-\alpha^{-2}L_p^{-2}}\right)\times$$
$$\times\left(\frac{(S_p/\alpha D_p)+1-\left[(S_p/\alpha D_p)\cosh\left(x_1/L_p\right)+(1/\alpha D_p)\sinh\left(x_1/L_p\right)\right]\exp\left(-\alpha x_1\right)}{(S_pL_p/D_p)\sinh\left(x_1/L_p\right)+\cosh\left(x_1/L_p\right)}-\exp\left(-\alpha x_1\right)\right) \tag{3.27}$$

In the depletion region, it is assumed that all absorbed photons produce electron-hole pairs that are collected. Therefore, the light current in the depletion region is:

$$J_g^{dep}\left(V\right) = -q\Gamma_0\exp\left(-\alpha x_1\right)\left(1-\exp\left(-\alpha x_2\left(V\right)-\alpha x_3\left(V\right)\right)\right) \tag{3.28}$$

The recombination current in the depletion region may be approximated by assuming a potential that is changing linearly with x in the depletion region. Then the recombination current for the whole region is assumed to be the maximum recombination rate times a small volume about this maximum recombination point:

$$J_r^{dep} = -q\frac{\int_0^x dx\int_0^y dy\int_0^{\frac{\pi k_BT}{q(V_{bi}-V)}} dz\frac{n_i}{\sqrt{\tau_n\tau_p}}\sinh\left(\frac{qV}{2k_BT}\right)}{\int_0^x dx\int_0^y dy} \tag{3.29}$$

which simplifies to:

$$J_r^{dep}\left(V\right) = -\frac{qn_i\left(x_2+x_3\right)}{\sqrt{\tau_{n0}\tau_{p0}}}\left[\frac{2\sinh\left(qV/2kT\right)}{q\left(V_{bi}-V\right)/kT}\right]\frac{\pi}{2} \tag{3.30}$$

Now, the current density can be defined as a sum of the light and dark currents[47]:

$$J = \left(J_0^p+J_0^n\right)\left(\exp\left(qV/kT\right)-1\right)+J_{dep}^r\left(V\right)-J_l^p-J_l^n-J_{dep}^g\left(V\right) \tag{3.31}$$

The current-bias curves are calculated for each individual cell using the equations above and an incident solar flux that is filtered by absorption of the cells above. Then current matching is enforced[50].

$$V\left(J\right) = \sum_{i=1}^{m} V_i\left(J\right) \tag{3.32}$$

One of the main questions in concentrator multi-junction solar cells is the effect of temperature and doping concentration on performance. Currently, we include a Drude model for free-carrier absorption[51].

$$\alpha_{fca} = \frac{q^2 \lambda^2 n_c}{4\pi^2 c^3 \epsilon_0 n_r m_c \tau_c} \tag{3.33}$$

where

$$\tau_c = \frac{m_c \mu_c}{q} \tag{3.34}$$

where λ is photon wavelength, n_c is carrier concentration, n_r is refractive index, m_c is carrier effective mass, ϵ_0 is permittivity of free space, and μ_c is carrier mobility. A more sophisticated free carrier absorption model incorporating inter-and intra-valley absorption processes was considered[51]. The derivation of the more sophisticated model included an error; therefore, the Drude model was chosen for its simplicity even though it over-estimates free carrier absorption. Material constants can be found in table B.1.

In addition, we have accounted for the temperature and doping concentration effects on carrier mobility using the empirical model developed by Sotoodeh et al.[52].

$$\mu_{LF}(N,T) = \mu_{min} + \frac{\mu_{max}(300K)\,(300K/T)^{\theta_1} - \mu_{min}}{1 + \left[\frac{N}{N_{ref}(300K)(T/300K)^{\theta_2}}\right]} \tag{3.35}$$

where all constants are fit parameters, N is carrier concentration, and T is temperature in Kelvin. The parameters used in this model are shown in table B.2. The model provides a good fit to well understood semiconductor materials, therefore, it provides a reasonable estimate for all four materials used in this study.

One of the largest challenges in a multijunction device model involves the limitations that current matching imposes. When a multijunction solar cell is made up of series connected subcells, the subcell thicknesses have a large impact on the device performance (see figure 3.2). Changing subcell thickness adjusts which cell is current-limiting. In this way, a thorough understanding of diffusion length effects on overall cell performance cannot be obtained without optimizing subcell thicknesses for each set of conditions. Unfortunately, this is a difficult multivariate optimization routine with many local optima. The optimization routine was run with many different starting positions in an attempt to ensure sufficient sampling of the efficiency surface. Subcell thickness was constrained to 0.2 µm<t<5 µm.

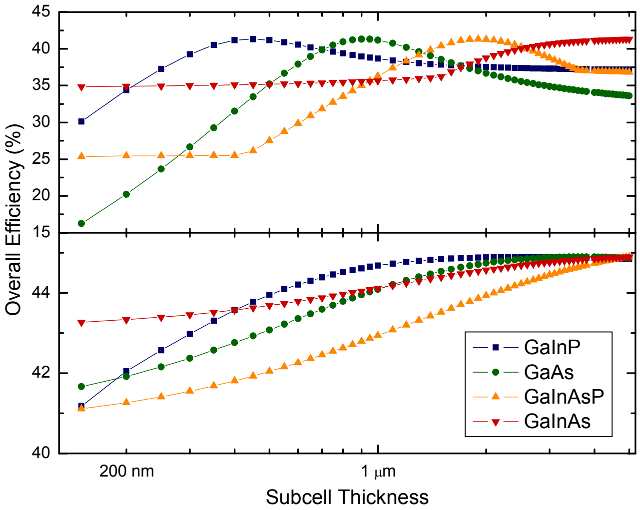

Figure 3.2. Overall cell efficiency as a function of subcell thickness. The subcell thicknesses were all set to the near optimum values for the series connected cell in the top graph and the independently connected cell in the bottom graph; then each subcell thickness was varied individually demonstrating the near-optimum values that are obtained in the series connected case.

The lower bound was defined based on the thickness of the fully depleted junction thickness for these doping conditions. All data presented within this chapter were calculated to be as close to optimum as possible, but are probably only near optimum. All observed trends were correct, and the maximum efficiency values were very close (within 0.1%) to the true optimums.

Before testing our model for four junction solar cell heterostructures, we performed preliminary calculations to verify the physical parameters and models correlated with known behaviors. To achieve this, the diffusion length was varied in one subcell at a time (figure 3.3). As expected, open circuit voltage drops off before short circuit current with a reduction in diffusion length.

3.2.2 The Effects of Series Connection

We explored the effect of electrical connection configuration (series or independent) on cell performance. It is well known that series connection can limit cell performance, but we wanted to quantify the effect, and explore whether an independent electrical configuration would provide sufficient gain to justify the added cost and complexity. Therefore, we con-

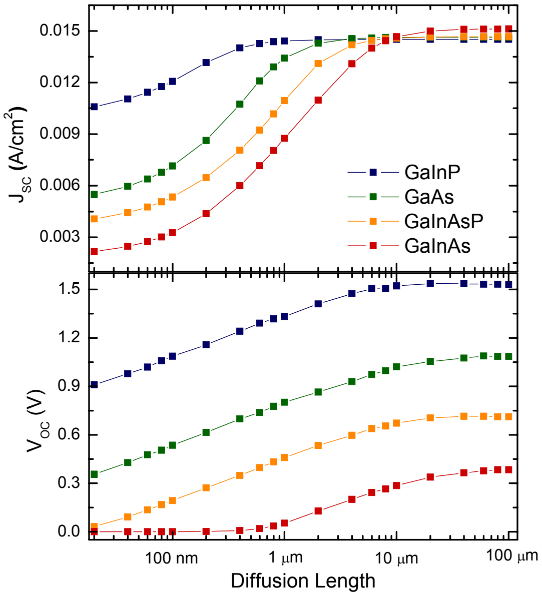

Figure 3.3. Short circuit current (J_{SC}) and open circuit voltage (V_{OC}) of the individual subcells as a function of the subcell diffusion length

sidered three different electrical connections shown in figure 3.4: a fully series connected device, a device with 2 independent connections separating the top two subcells from the bottom two, and a fully independently connected device. The first test was to co-vary the diffusion length in all four subcells together and investigate overall device efficiency (see figure 3.4). Interestingly, the 2 independent connection configuration provides 75% of the gain achieved from total independent connections, and is more feasible. Additionally, if the material quality is poor (<2 µm), the alternative electrical connections do not show enhanced performance relative to the two-terminal device.

In addition, electrical connection effects were explored further using reference Hot Sunny Day[53] spectral data to simulate the overall power output change in a full day/night cycle. By optimizing the device for the peak flux of the day, then calculating the performance over the course of the day we can elucidate the true differences in the three electrical connections. As can be seen in figure 3.5, the efficiency roll off in the early and late hours of the day is much less significant in the device with four independent connections. In terms of power density produced, the four independent connections cell provides a ~9% gain, and the 2 independent connections cell produces ~5.5%.

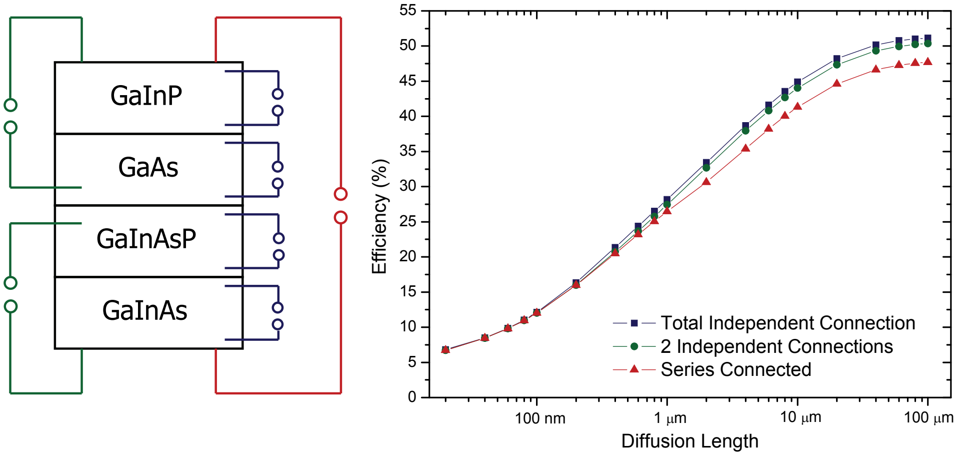

Figure 3.4. Overall cell efficiency as a function of the diffusion length in all four subcells for 3 different electrical connections

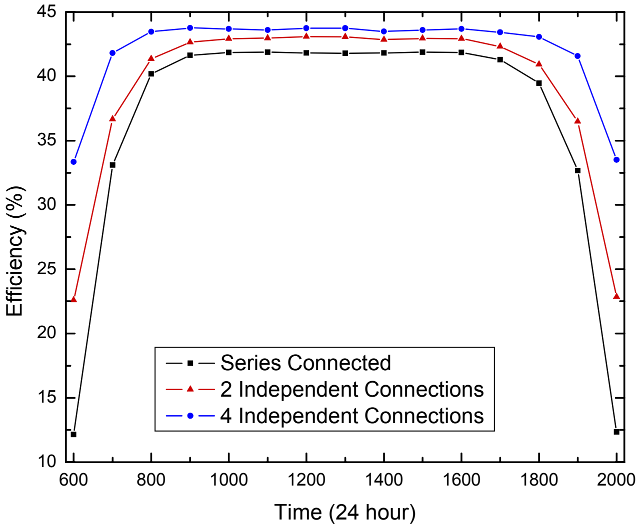

Figure 3.5. Overall cell efficiency as a function of time, using the reference fluxes for a Hot Sunny Day

3.2.3 The Effects of Changing Operating Temperature

One of the goals in building this model was to include the effects of changing device temperature on the intrinsic device performance. With increasing temperature, cell performance decreases (see figure 3.6). Temperature effects the band gap, intrinsic carrier concentration, and mobility in semiconductors. The empirical mobility model developed by Sotoodeh et al.[52], described previously, contains the carrier mobility temperature dependence required for this calculation. Additional corrections for band gap and intrinsic carrier concentrations were required. The temperature dependence of the band gap of each material was found using the universal expression[54]:

$$E_g\left(T\right) \approx E_g\left(0\right) - \frac{\alpha T^2}{T+\beta} \tag{3.36}$$

The constants α and β are fitting constants to experimental data. The values used are shown in table B.3. The values for $\mathrm{Ga}_{0.19}\mathrm{In}_{0.81}\mathrm{As}_{0.37}\mathrm{P}_{0.63}$ were found by interpolation.

The intrinsic carrier concentration temperature dependence can be found using the following[54]:

$$n_i = \left(\frac{k_B T}{2\pi\hbar^2}\right)^{3/2} \left(m_n m_p\right)^{3/4} \exp\left(\frac{-\left(E_g\left(0\right) - \frac{\alpha T^2}{T+\beta}\right)}{2k_B T}\right) \tag{3.37}$$

In the model, the effects of temperature on band gap are implemented by shifting the absorption coefficient of the materials by the change in E_g. From these equations, mobility will decrease in each material with increasing temperature and intrinsic carrier concentration will increase. As intrinsic carrier concentration is proportional to recombination current, all of these temperature effects serve to lower the overall performance of the device with increasing temperature. The temperature effect on overall device performance, assuming constant diffusion length of 10 µm in each cell is shown in figure 3.6.

3.2.4 Spectral Variation Effects

The design of multijunction cells is generally constrained by current matching. Therefore, one could imagine that spectral variations could cause these devices to move well outside of optimum operating conditions. To explore this idea, data collected for several reference solar flux datasets (“nice day”, “hot sunny day”, “hot cloudy day”, “cold sunny day”, and

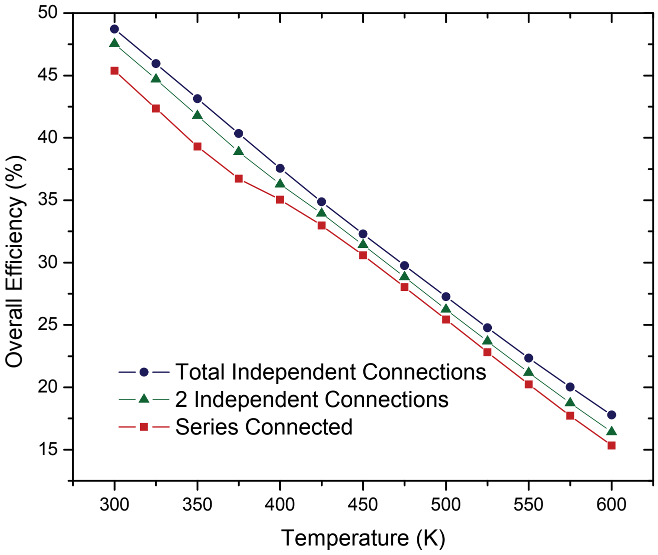

Figure 3.6. Overall cell efficiency as a function of temperature

“cold cloudy day”) were used as input solar flux instead of the AM1.5G spectrum. The cold day spectra were taken during winter, and the hot day spectra in summer. In addition to significant variations in total flux at any given time of the day, the relative intensities of different portions of the spectrum change as well. The total flux from each spectra is shown in figure 3.7[53].

Given the large changes in solar flux over the course of a day, the cell must be optimized for the diurnal cycle rather than the peak flux (typically at 1300hrs/1:00pm). When optimized off-peak (0900hrs), more power is extracted over the course of the day; 1.2% total power gain over the course of hot sunny day, 1.5% gain for the nice day spectrum (see figure 3.8). Fortunately, a cell optimized for any of the three sunny spectra had strong performance over all three days (see figure 3.9). The total power density produced over the day cycle ranges from 39.6–40.4% of the total power available each day. However, as one could imagine, by changing the electrical connections of the cell, the performance is enhanced over the entire day/night cycle since the operating points of the individual cells can shift with the change in solar flux (see figure 3.10). For example if there is more blue in the spectrum early in the day, the top GaInP cell is producing more current than when the spectrum is red-shifted.

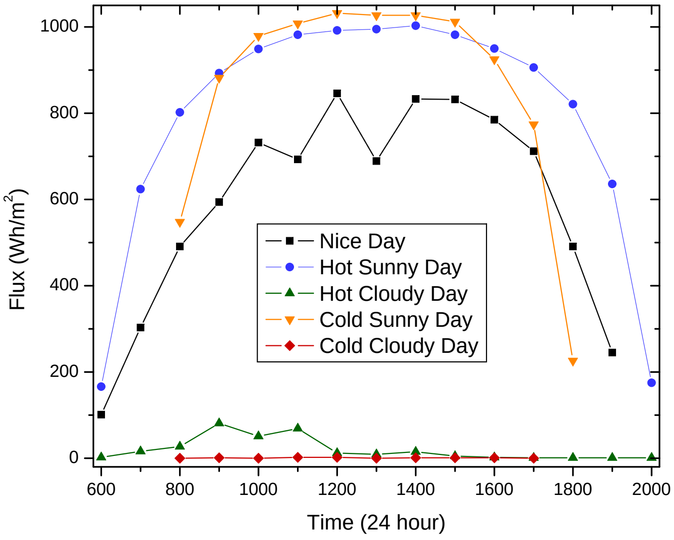

Figure 3.7. Direct solar flux for different reference spectra as a function of the time of day

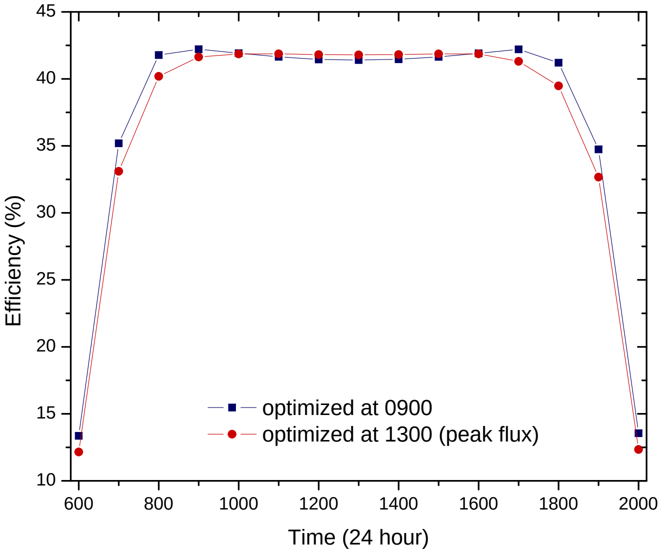

Figure 3.8. Efficiency of a four junction solar cell at different times of the day when optimized for the peak and off-peak spectra

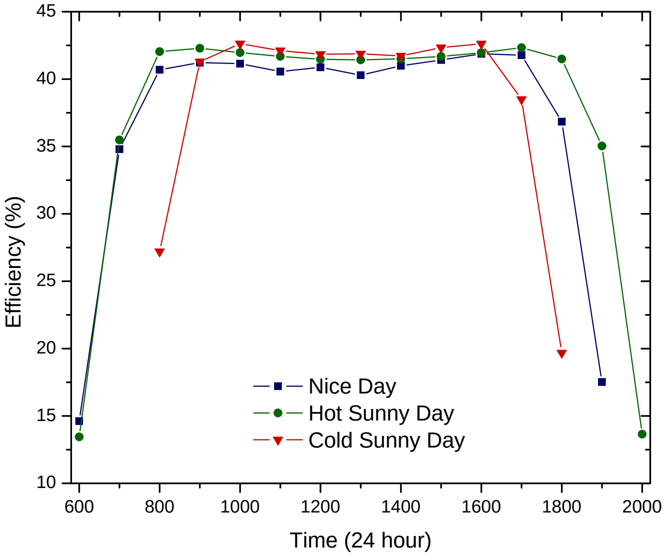

Figure 3.9. Performance of a single four junction cell design optimized for the Hot Sunny Day

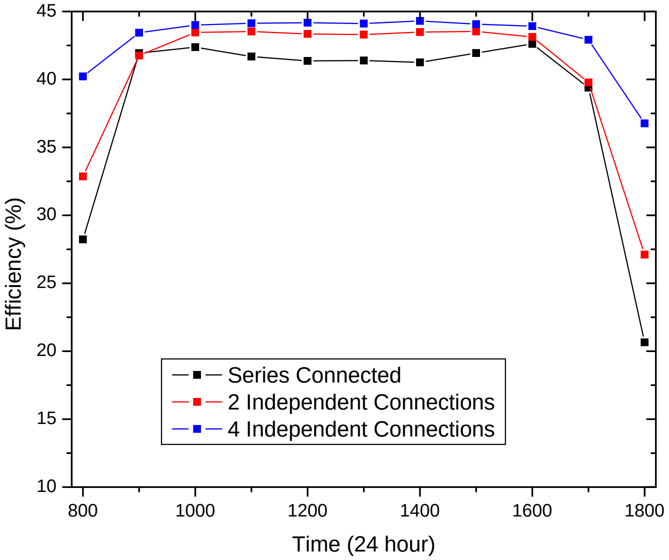

Figure 3.10. Efficiency versus time of day for three different cell designs: series connected, 2 independent connections, and total independent connections

Table 3.1. Maximum power density over the day cycle as a function of the electrical connections of each device

		Total Power (mW/cm^2)			2ind/4ind (%)
Nice Day	Series	330.66			
	Two Independent	346.53	4.80	% gain	
	Total Independent	358.35	8.37	% gain	57.31
Hot Sunny Day	Series	477.21			
	Two Independent	494.26	3.57	% gain	
	Total Independent	511.75	7.24	% gain	49.36
Hot Cloudy Day	Series	9.345			
	Two Independent	9.556	2.226	% gain	
	Total Independent	10.047	7.51	% gain	30.06
Cold Sunny Day	Series	380.57			
	Two Independent	395.98	4.05	% gain	
	Total Independent	411.07	8.01	% gain	50.52
Cold Cloudy Day	Series	0.205			
	Two Independent	0.208	1.46	% gain	
	Total Independent	0.217	5.85	% gain	25.00

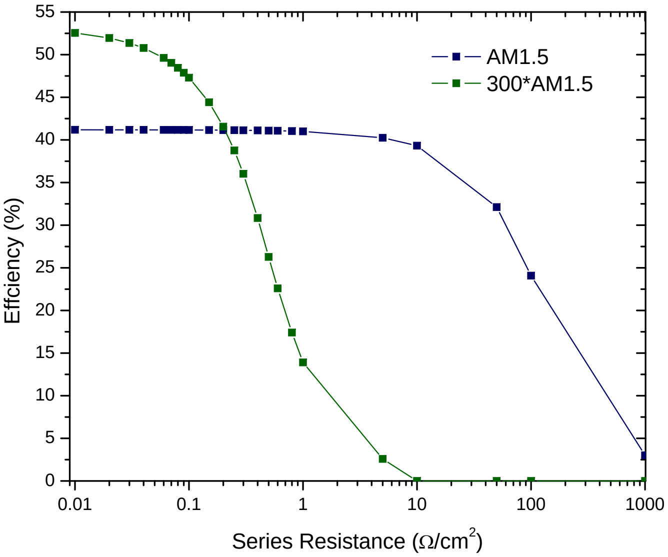

Figure 3.11. Efficiency of the four junction device as a function of overall series resistance for one sun and 300 sun illuminations

3.2.5 Series Resistance

One of the main challenges in designing multijunction solar cells is creating tunnel junctions with low resistance and low free carrier absorption. Generally, tunnel junctions are very highly doped, but kept extremely thin to minimize free carrier absorption. With increasing solar flux concentration, the maximum allowed series resistance in a device decreases significantly since current densities go up with concentration (V=IR). In order to better understand this phenomenon and define series resistance limitations on these devices an effective series resistance was added to the entire device. Essentially, all series resistances (3 tunnel junctions, front and back contacts, etc.) were lumped into one overall series resistance. As can be seen from figure 3.11 the device is relatively insensitive to series resistances up to about 10 Ω/cm^2 under one sun illumination. However, when solar flux concentration is increased to 300 suns, device performance begins to fall off with any increase in series resistance from 0.01 Ω/cm^2, with significant efficiency reduction above approximately 0.1 Ω/cm^2.

To confirm the overall series resistance calculation was working as expected, IV curves for several of the points shown in figure 3.11 were examined. These are shown in figure 3.12. As expected, the curves show a strong departure from vertical at high biases. This departure results in lower FF and hence lower efficiency.

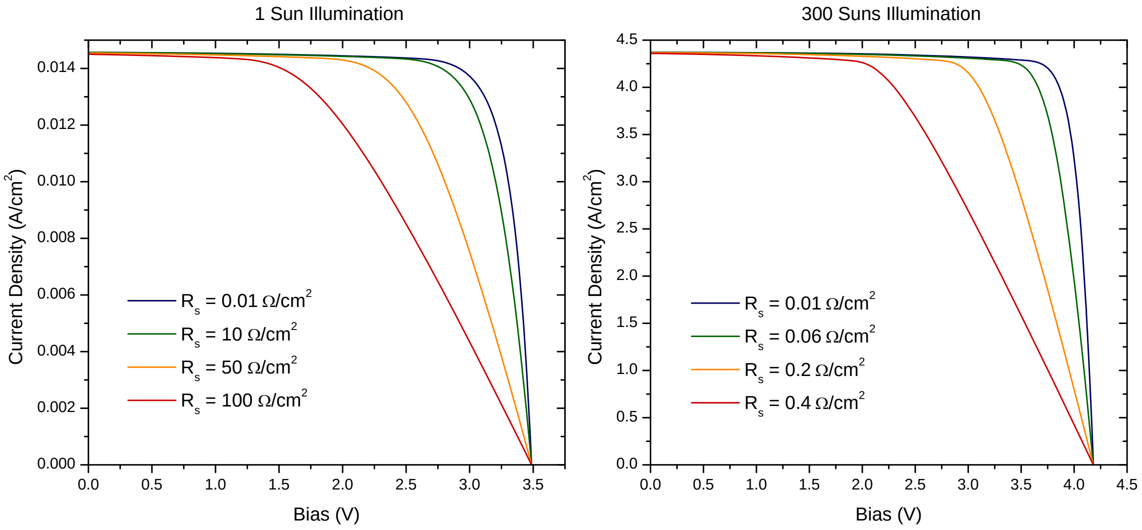

Figure 3.12. IV curves for the four junction device as a function of overall series resistance for one sun and 300 sun illuminations

Unfortunately, the assumptions in the depletion approximation are quite large. More specifically, the recombination rate within the depletion region as a single Shockley-Read level at mid gap is invalid for direct-gap semiconductors and high illumination. The boundary condition at the depletion layer edge which assumes that all photogenerated carriers are collected by the built-in field is also invalid for direct gap semiconductors and high illumination. In CdTe it results in an over-estimate of the light generated current of 2%. Finally, the expression for the diffusion of hot carriers within the depletion region does not account for thermalization effects. These assumptions are commonly used and consistent with Shockley diode theory, but they are inadequate for this application. Attempts to extend this model to account for the detailed effects of tunnel junctions and back surface fields would be lost in the rounding. We have reached the limit of phenomena we can understand with the current model and must look for alternatives to the depletion approximation for solving the carrier transport equations.

3.3 Finite Element Modeling

3.3.1 COMSOL Multiphysics

In order to move away from analytical solutions to the transport equations, a finite element method was needed. Attempts to model the devices within the COMSOL (formerly

FEMLAB) modeling environment were undertaken. The main advantage of COMSOL was a relatively low learning curve. Therefore it was quite straightforward to set up complex transport problems and geometries, and allow the built-in solvers to do the complex math.

Initial investigations used a single-junction (GaAs) solar cell. The model was constructed very similarly to the built-in model of a pn-junction. The p-type base was 5 µm×5 µm and the n-type emitter was 200 nm×5 µm. The entire bottom surface of the base (boundary 2) was designated as a contact. Three discrete contacts were placed on the top surface of the emitter. Two were 200 nm from the edges and 500 nm wide (boundaries 6 and 10). The third was 500 nm wide and in the center of the top surface (boundary 8). The constants used can be found in Appendix B tables B.4 and B.5. Three application modes were employed, electrostatics (es), and two convection and diffusion modes: one for holes (cp) and the other for electrons (cn). As COMSOL does not have a method for illuminating the device with light, which is key for solar cells, a Matlab m-file was written to describe the generation of electron hole pairs as a function of depth in the device. The scalar expressions used in the model can be seen in table 3.2.

In order to calculate the device current density, two boundary expressions were defined using Lagrange multipliers. The electron current density was defined as $Jn = -q * lm3$ at the top and bottom contacts (boundaries 2, 6, 8, 10). The hole current density was defined as $Jp = q * lm4$ at the contacts. The next step was to define the physics in the 3 application modes. There was one scalar constant defined in the electrostatics mode, the permittivity of free space, epsilon0=8.854187817e-12 F/m. All of the boundary conditions were defined as zero charge/symmetry except the junction boundary, which was defined using continuity, and the contacts which were defined as -V_junction/2 at the bottom, and -V_junction/2+Va at the top. The subdomain physics were defined using the constitutive relation $\mathbf{D} = \epsilon_0 \epsilon_r \mathbf{E}$, where the relative permittivity, ϵ_r = epsilonr, and the space charge density, ρ = q*(cp-cn-Na) in the p-type material, and ρ = q*(cp-cn+Nd) in the n-type material. The initial value of the electric potential was defined as phi_init.

Next, convection and diffusion application modes were defined assuming isotropic diffusion, where diffusivity was defined as Dn for electrons and Dp for holes. The reaction rate was -RSRH for both. The x and y velocities were defined in terms of first partial derivatives of the electric potential, mun*phix and mun*phiy for electrons and -mup*phix and -mup*phiy for holes. The boundary conditions were defined as insulation/symmetry

Table 3.2. Scalar Expressions used in COMSOL modeling work

Name	Expression	Description
RSRH	(cp*cn-ni^2)/(taup*(cn+ni)+taun*(cp+ni))	Shockley-Read-Hall Recombination
G	absorption(y)	Generation function
n0	ni*exp((q*phi0+X+0.5*Eg)/(k*T)	Initial electron concentration
p0	ni*exp(-(q*phi0+X+0.5*Eg)/(k*T))	Initial hole concentration
phi_init	A*(y-5e-6)^2+B*(y-5e-6)+C	Initial built-in field

boundaries for all boundaries except the junction and the contacts. The junction was defined by continuity and the contacts were defined as constant concentration boundaries, where there were minority and majority carriers defined by the doping conditions.

As written, the model does not come to a convergent solution. In order to find a solution at zero applied bias, first the built-in potential (from the junction) must be slowly increased to the full value (∼1.4 V) using the parametric solver. Next, the real zero bias case must be solved using the UMFPACK direct solver. Finally, the parametric solver can be used to solve for the condition under different applied biases. When solving for the carrier concentrations in the device, negative values were always obtained upon applying an external bias (figure 3.13 and 3.14). The solver algorithms within COMSOL were not designed for semiconductor device physics. Within these devices the carrier concentrations range over many orders of magnitude and change rapidly in very narrow regions of the devices. Many attempts were made at working around the sharp change in concentration including shifting the concentration to the log of the concentration as well as lowering the initial doping levels and slowly increasing them to the true levels.

When we revisited the built-in pn junction model, we discovered that this problem of negative concentrations was there as well. COMSOL technical support does not view this problem as a problem. However, if we would like to get a real understanding of the operation of these devices, the negative concentrations need to be eliminated, or significantly reduced. Having negative concentrations that approach the same magnitude as the maximum positive concentrations was unacceptable. We would strongly recommend against using COMSOL for semiconductor device modeling until suitable solver algorithms are developed.

3.3.2 Synopsys TCAD Sentaurus

Due to these limitations, our modeling effort is now focused on building our devices in a package by Synopsys called Sentaurus. Sentaurus was originally developed for modeling Si semiconductor devices. However, it has built-in capabilities for changing the materials in the devices to a wide range of semiconductor materials. In addition, new materials can be added to the program by end users. Unfortunately, with more powerful software packages, comes a much steeper learning curve. We are still in the early stages of developing a model in this software. However, from talking with others who have worked with this software for GaAs devices, one problem that will need careful attention is that whenever there is

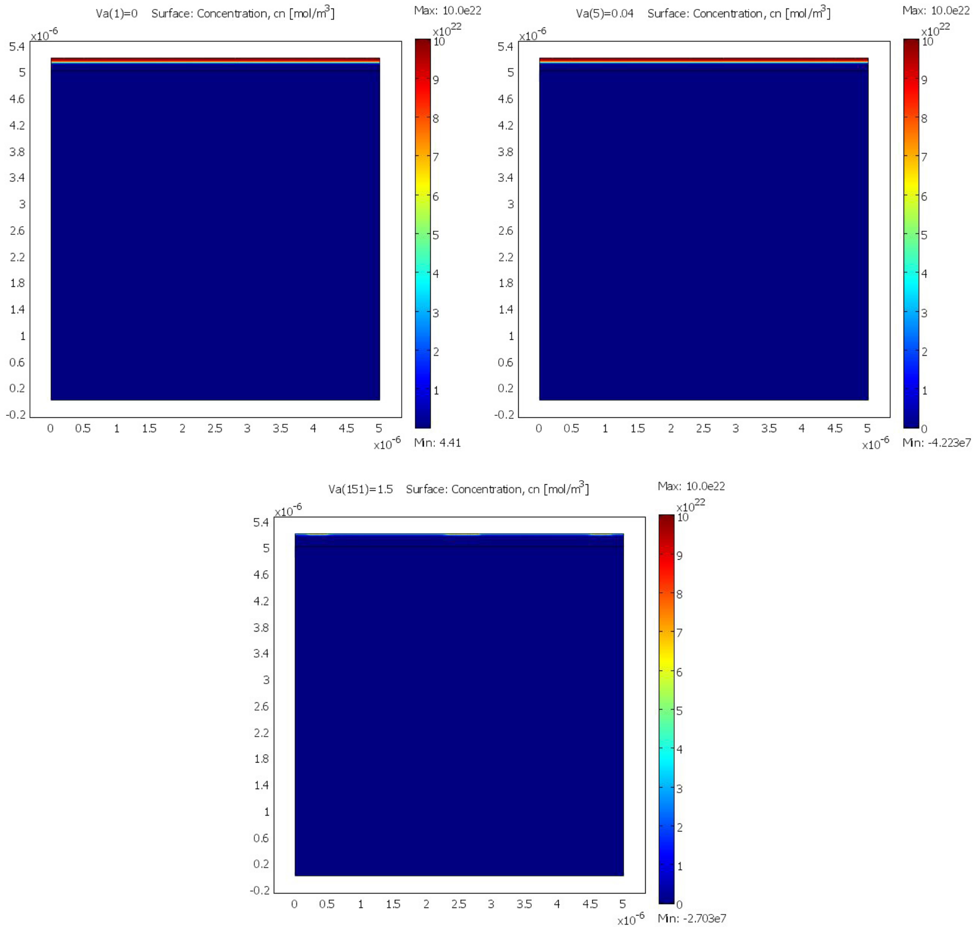

Figure 3.13. Plot of the electron concentration in the device for 0 V (top left), 0.04 V (top right), and 1.5 V (bottom) applied bias. The onset of negative concentrations of electrons corresponds to 0.04 V applied bias.

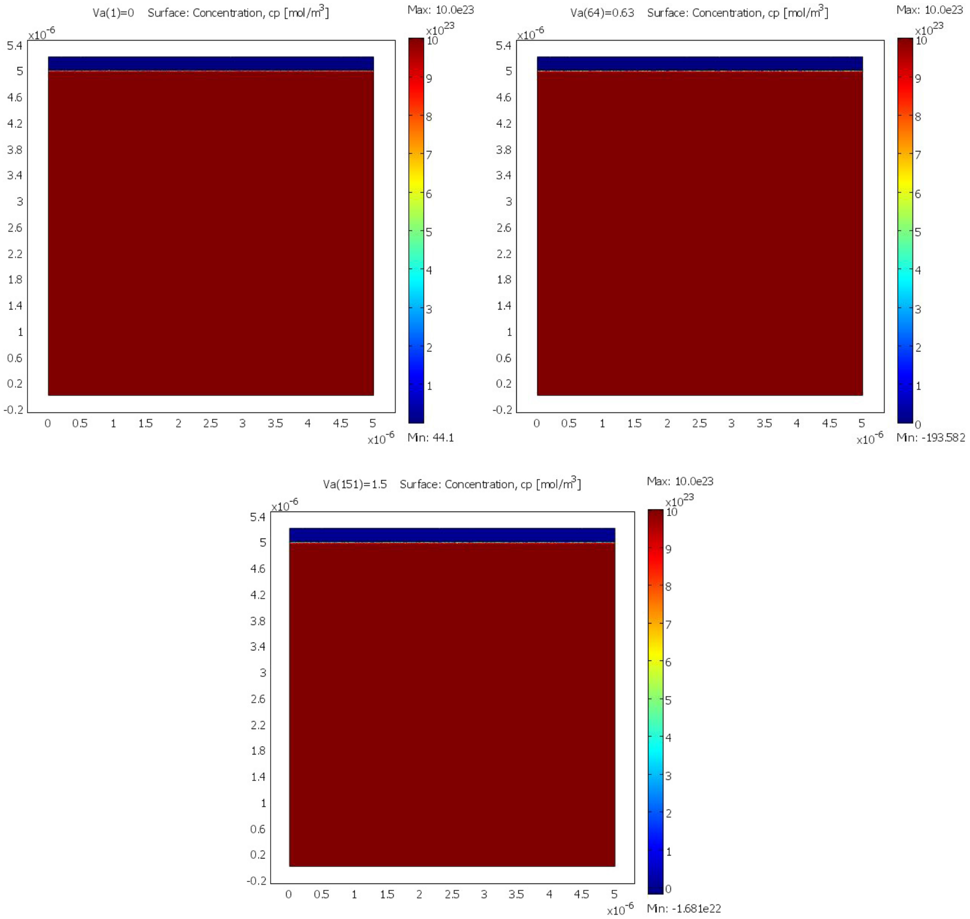

Figure 3.14. Plot of the hole concentration in the device for 0 V (top left), 0.63 V (top right), and 1.5 V (bottom) applied bias. The onset of negative concentrations of holes corresponds to 0.63 V applied bias.

a material property missing, the program treats the material as if it were silicon. Since the III-V materials are very different from silicon, this could produce significant errors. One of the first steps will be to carefully examine the materials data files for GaAs and potentially to create data files for the other III-V materials. However, there have been reports from Fraunhofer Institute[55, 56] that Sentaurus can be used to successfully model GaAs solar cells, so there is clear potential for success in modeling III-V solar cells using this package. In addition, Sentaurus includes several options for simulating illumination of the device from Maxwell's equations to simple ray tracing. The one limitation in device illumination is that though a spectrum can be given as the input, the response of the device is calculated for each wavelength specified, so the simulation time increases linearly with specified wavelengths.

3.4 Conclusion

We have constructed an analytical model in MATLAB for simulating the performance of complex (>2 junction) III-V multijunction solar cells. The model allowed us to explore the complex multivariate space that governs device performance to better understand which parts of the device will benefit most from improvement. We have explored the creation of a 2 independent connection device that indicates a benefit relative to a series connected structure. In addition, we have proposed that the next step in this work is to develop a similar model within Synopsys TCAD Sentaurus, which does not require large assumptions like the depletion approximation.

Chapter 4

III-V Cells

4.1 Introduction

This chapter presents results from dual junction solar cells grown on Ge/Si epitaxial templates.

4.2 GaInP Single Junction Solar Cells

GaInP/GaAs dual junction solar cells were grown on Ge/Si epitaxial templates by our collaborators, Spectrolab (figure 4.1). Chapter 2 described template preparation. All Ge/Si templates prepared for single and/or dual junction growth employed a SiO_2 bonding layer. This required all electrical contacts to be placed on the front side of the structure. The first round of growths used the contacts placed on the top of the structure and at the tunnel junction between the GaInP and GaAs cells. In this manner, the GaAs cell is essentially inactive and the structure performs as a single junction GaInP cell, but with an extra thick buffer layer from the substrate surface.

In this first round of growths, the epitaxial templates were 1/4 2" Ge wafers on 2" Si wafers prepared with just a 30 s wet etch. In addition, the the donor wafer that created each epitaxial template was included. The donor wafers were prepared with the same wet etch treatment. The cells were tested using light current-voltage (IV) measurements (figure 4.2) as well as spectral response measurements (figure 4.2). After all electrical testing was complete, the cells were examined by XTEM (figure 4.3).

Initial cell results were without anti-reflective coating and without optimized growth parameters. Spectral response measurements were taken on the GaInP top cell and converted to external quantum efficiency. The Ge/Si template showed about the same overall quantum efficiency as the donor wafer. Surface preparation dominated device performance,

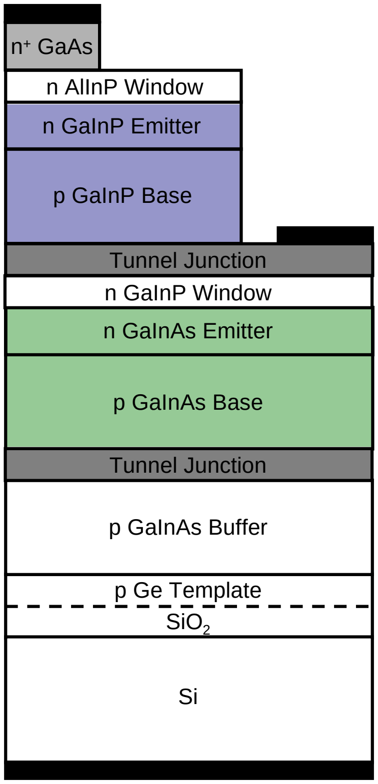

Figure 4.1. Schematic of the cell structure grown in round 1. The bonded interface is denoted by the dashed line. The solid black rectangles are the metal contacts.

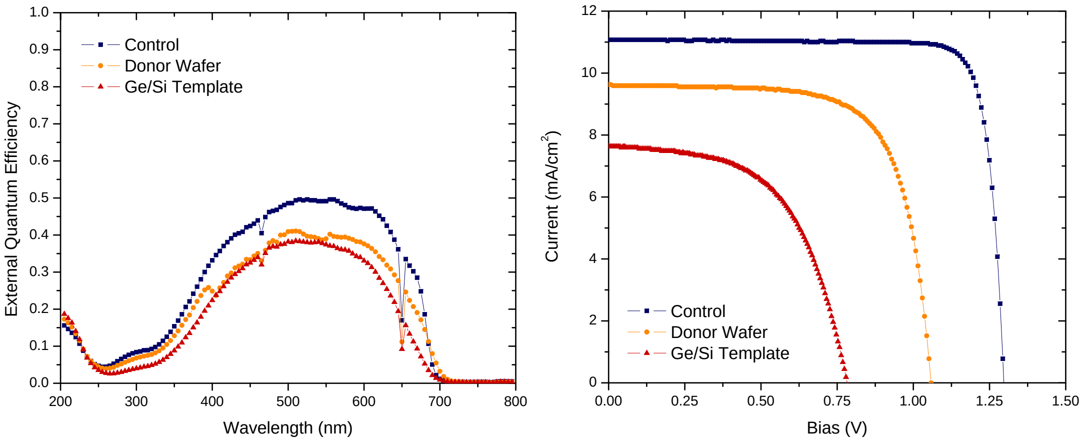

Figure 4.2. External quantum efficiency and light IV measurements on GaInP solar cells grown on Ge/Si epitaxial templates

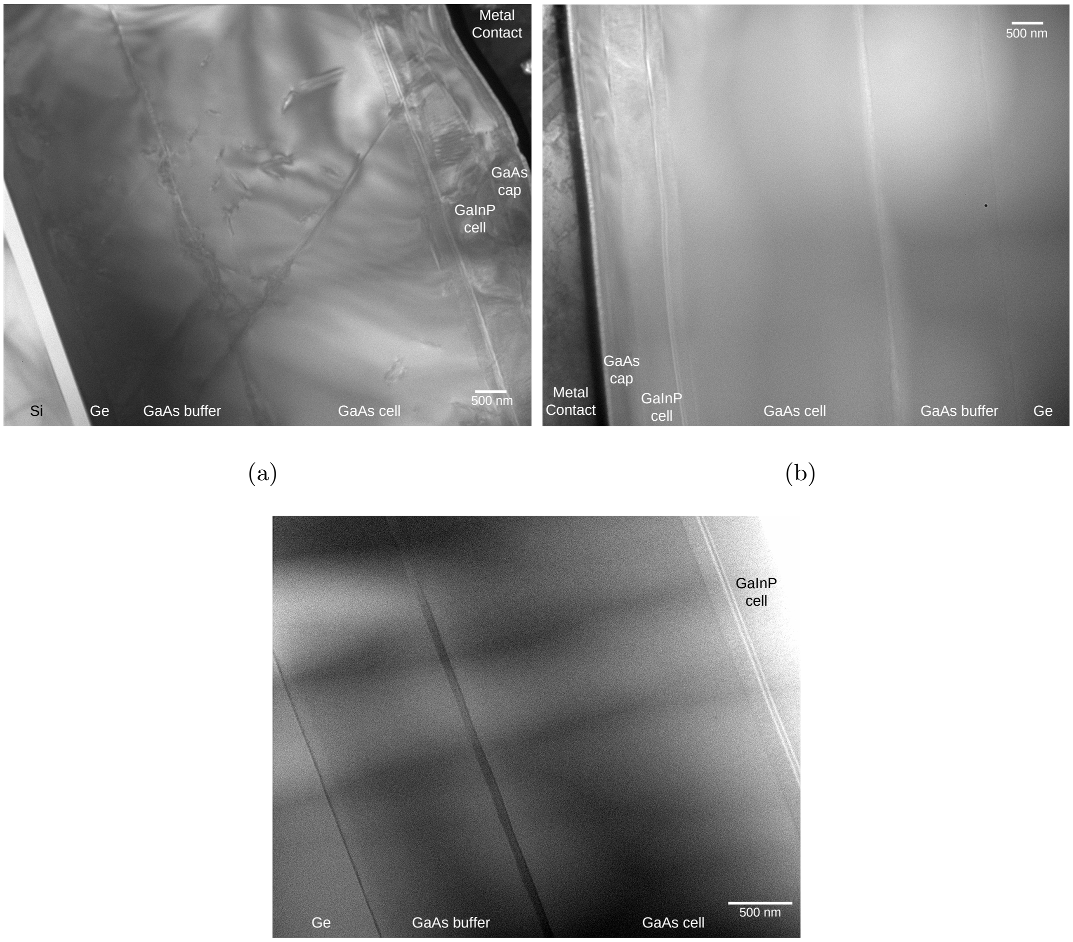

(a)

(b)

(c)

Figure 4.3. XTEM overview images of the grown structure corresponding to the (a) Ge/Si substrate, (b) Ge donor wafer, (c) bulk Ge control sample

not strain induced by coefficient of thermal expansion mismatch. The light IV data does show a significant drop in open circuit voltage, as well as in short circuit current. This is characteristic of poor quality material. Work by Zahler et al.[35] on single junction InGaAs cells grown on InP/Si epitaxial templates indicated wet etching to ∼10 nm RMS roughness was sufficient to achieve very high quality epitaxial growth. However, a significant difference is that the epitaxial template was polar, whereas the Ge is not. Therefore, anti-phase domains are less common defects in polar on polar lattice-matched growth than in polar on non-polar growth. XTEM was performed to understand where defects initiated on these Ge/Si templates.

The XTEM images show the drastic difference in light IV behavior between the donor wafer and Ge/Si template corresponded to significantly different defect densities. The donor wafer and Ge/Si templates present almost identical surfaces for heteroepitaxial growth. Therefore, the high defect density from Ge/Si templates could be due to non-optimum growth conditions. In the next growth run, Spectrolab adjusted the growth parameters to better suit epitaxial growth on Ge/Si templates. In addition, the cell processing wet etch processes was changed to contact the tunnel junction below the GaAs cell as shown in figure 4.4. Electrical characterization of these devices (figure 4.5) shows the growth was well tuned to bulk Ge and donor wafer substrates, but not to transferred layer substrates. The primary difference during growth between donor wafer and template was substrate surface temperature. The donor wafer behaves as a bulk Ge wafer, whereas the template is primarily a thick silicon substrate. As the MOCVD tool uses IR heating, the difference in thickness and IR absorption causes significant surface temperature differences. However, overall the second growth round was very disappointing. The open-circuit voltage corresponded to that of a single junction GaInP cell, rather than the dual junction that was grown, as evidenced by the spectral response measurements. The growth process was re-evaluated at Spectrolab to look for reasons for this behavior.

The third growth round used Ge/Si templates with different CMP processes and was a single junction GaInP solar cell growth (like round 1, but without the GaAs subcell). To simplify the growth structure, only single junction GaInP solar cells were grown and tested. Unfortunately, the first few template structures that were used showed significant delamination (figure 4.6). High-resolution x-ray diffraction (HRXRD) showed the grown structure was not well lattice matched. Tensile strain induced due to lattice mismatch caused the templates to fail. Further growth parameter refinement enabled lattice matched material growth. As can be seen in figure 4.7, the device performance and thus material quality was significantly improved. However, the active area of the samples was limited as we were conserving implanted Ge by using one 2” Ge wafer to make 4 Ge/Si epitaxial templates.

4.3 GaInP/GaAs Dual Junction Solar Cells

Having shown high-quality growth on CMP prepared epitaxial templates, the next goal was growth and testing of dual junction cells. Also, the work with double heterostructures

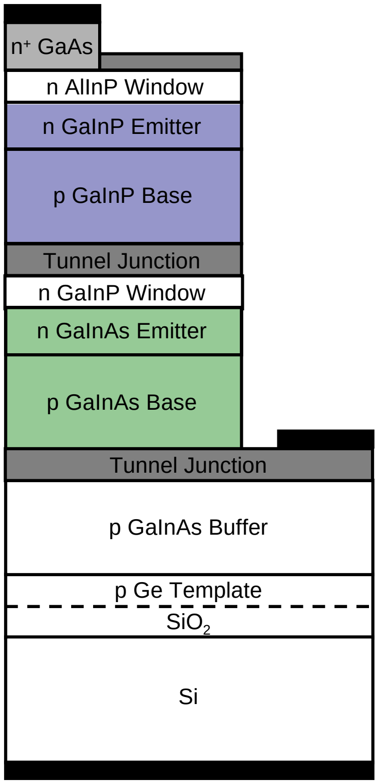

Figure 4.4. Schematic of the cell structure grown in round 2. The bonded interface is denoted by the dashed line. The solid black rectangles are the metal contacts.

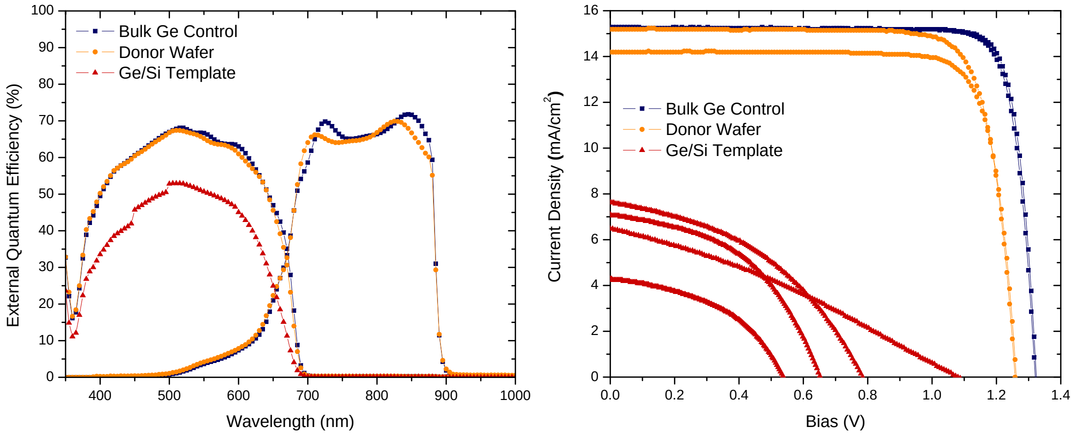

Figure 4.5. External quantum efficiency and light IV measurements on GaInP/GaAs dual junction solar cells grown on Ge/Si epitaxial templates

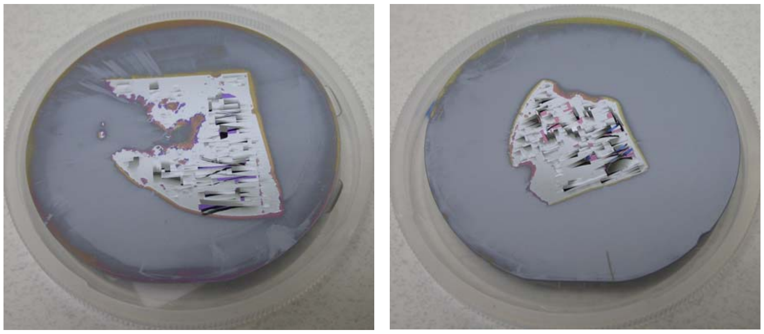

Figure 4.6. Two Ge/Si templates after MOCVD growth of lattice mismatched material adding tensile strain

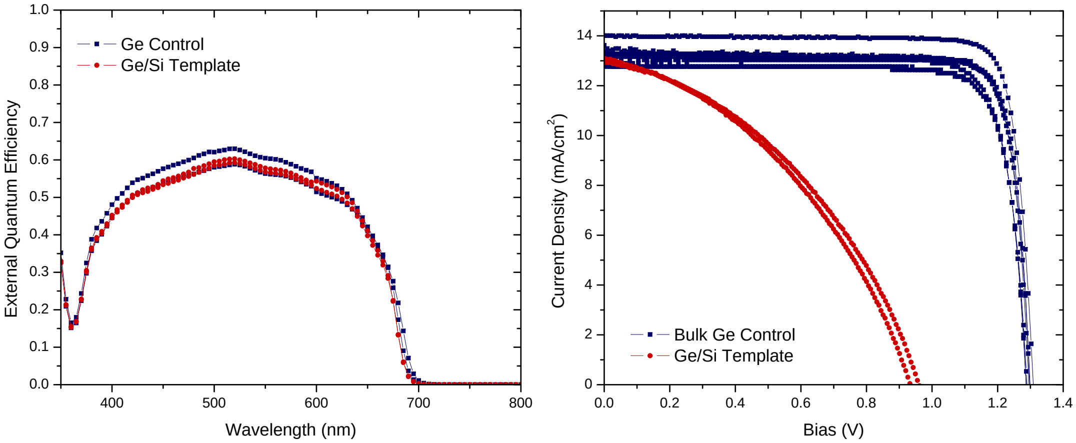

Figure 4.7. External quantum efficiency and light IV measurements on GaInP solar cells grown on Ge/Si epitaxial templates

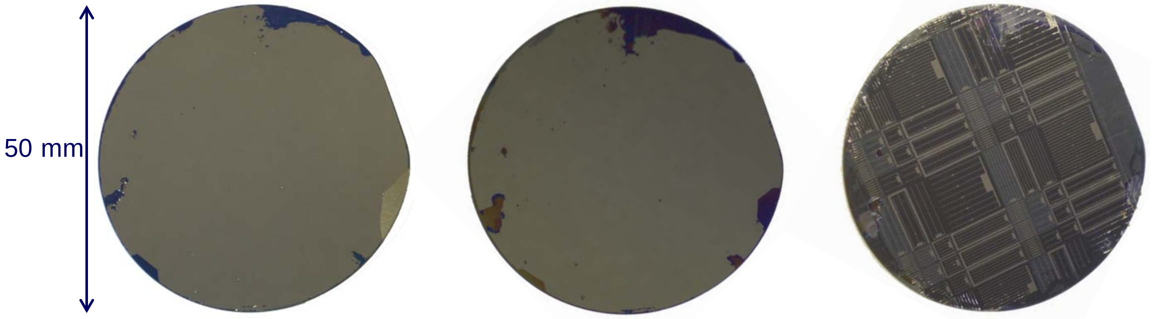

Figure 4.8. Pictures of the Ge/Si epitaxial template as-transferred, processed for growth, and after growth and cell processing (left to right)

showed GaAs to be more sensitive than GaInP. The next round of growths used full 2" Ge/Si templates (figure 4.8). With quarter wafer transferred layers, there were at most four solar cells per sample for testing. By increasing the transferred area, the number of cells available for testing was increased. It also offered greater insight into uniformity of Ge/Si templates. The dual junction structure grown was teh same as that used in round 2 (figure 4.4).

Again, light IV and SR measurements were used to evaluate growth quality (figure 4.9). In this round of growth, we saw comparable performance between the control cells and Ge/Si template cells. The light IV data show comparable short circuit current between some control devices grown on a bulk Ge substrate and some devices grown on a Ge/Si template. However, open circuit voltage is slightly lower (1.97-2.08 V versus 2.16 V) in the devices grown on the Ge/Si template. Overall, the device performance is comparable to the control with no loss in fill factor (FF) compared with the control (FF = 0.79). After AR coating, the control cell showed an efficiency of 17.2-19.9%, whereas the Ge/Si templates had an efficiency of 15.5-15.7%. Spectral response measurements indicate the GaInP cell band gap has shifted approximately 60 meV from ∼1.74 to ∼1.8 eV. This band gap shift was due to GaInP composition change. The Ge substrate used for the control sample in these growths was (100) oriented with a miscut of 6° toward the ⟨011⟩ orientation, whereas the Ge wafer used to make the Ge/Si template was (100) oriented with a miscut of 9° toward the ⟨011⟩ orientation. Higher miscut substrates have lower In composition for the same growth conditions[57]. Shown in figure 4.10 is the HRXRD data for the control sample and Ge/Si template sample. The scan on the control sample shows the top cell to be compressively strained 691 s, which corresponds to an indium composition of about

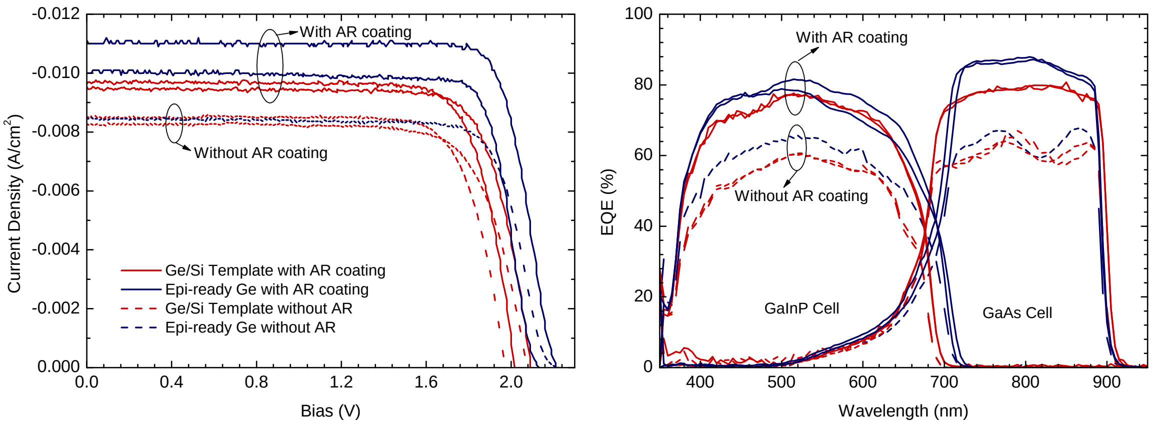

Figure 4.9. Light IV and SR measurements for cells on Ge/Si templates as well as bulk Ge

53%, assuming 100% strain. On the other hand, the Ge/Si sample was lattice matched, which corresponded to an indium composition of 49.5%. Increasing indium composition by 3.5% decreases the band gap by ∼64 meV[58], which correlates well with the spectral response measurements. Though this explains the band gap shift seen in spectral response well, the loss in open circuit voltage is larger than this difference. In addition, a "good" GaInP/GaAs dual junction cell should achieve close to 28% efficiency, not under 20%. For this reason, additional factors must be occurring during growth. The growth was tuned for the epitaxial templates, it could be non-optimal for the bulk Ge control sample. In order to fully understand growth parameter changes and the effects on device performance, a plentiful supply of template substrates is needed. Dual junction cell growth should be optimized separately for Ge/Si templates and bulk Ge. At that stage, a fair comparison could be made. In addition, cross-sectional TEM may offer insight to where the additional loss in open circuit voltage on template samples were originating.

To put the preceding results in perspective, images of all Ge/Si epitaxial templates after growth are shown in figure 4.11. The final appearance of the 2" wafers is very different between the different wafers. In addition, the mask that was used to define the individual cells allows for a maximum of 23 testable cells on each wafer. The gold u-shape which surrounds about half of the cells is the bottom contact. Only those cells with that bottom contact can be tested.

Of all 110 testable cells on these six samples, five showed performance that was comparable to the controls: two on one and three on another epitaxial template. The data from all the cells tested on the template with the two best performing cells are shown in figure 4.12.

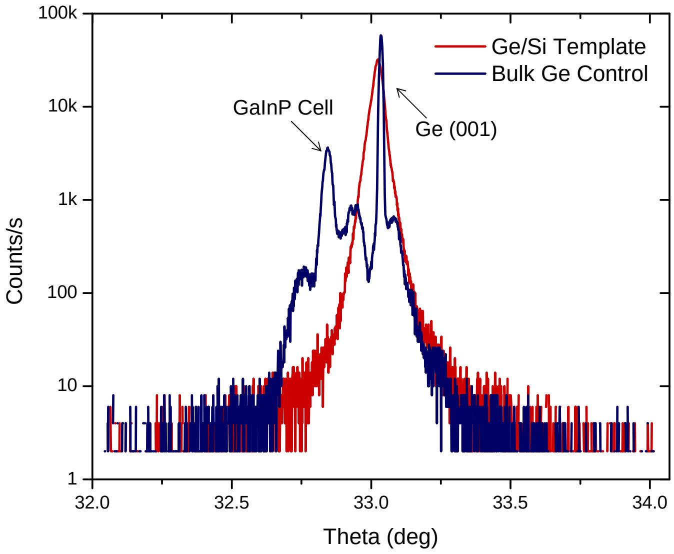

Figure 4.10. High resolution XRD rocking curves about the Ge (001) peak showing the lattice matched structure on the Ge/Si templates and the lattice mismatch of the GaInP on the bulk Ge substrate

The main problem with the poor performing cells on the Ge/Si templates was shunting, as can be seen from the light IV curves. The diffeernce between good and bad cells can be seen easily with an optical microscope. Figure 4.13 shows one of the top performing cells as compared to one that exhibited significant shunting. These two cells were side by side on the wafer.

4.4 Alternative Substrates

Though the results from the last dual junction cell growth looked very promising, the drop in open circuit voltage between the control and the template cells was not fully explained by the GaInP band gap shift. Therefore, we would like to better understand the effects of template strain state on cell performance and III-V material growth. Searching CTEs of suitable substrate materials indicated several alternatives. Sapphire has a higher CTE than Ge (6.95 ppm/K versus 5.8 ppm/K respectively), whereas the CTE of Si is 2.6 ppm/K. Therefore, making templates with sapphire substrates would allow us to compare the different strain states even if we could not quantify the strain. In addition, thin Si (100 μm) is more flexible than traditional thick Si substrates, which could accommodate some degree of strain. The plan was to perform wafer curvature measurements made with the CGS300 system in the

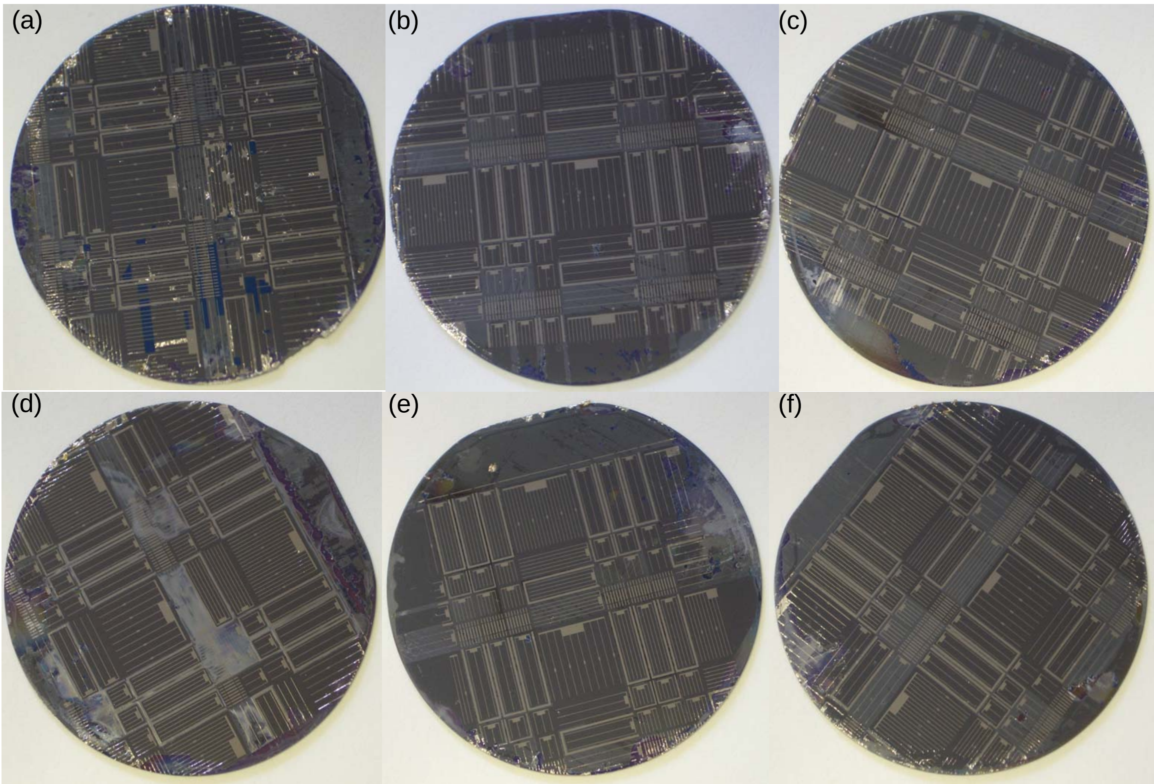

Figure 4.11. Optical images of the 6 epitaxial templates used in the final round of growths. All templates were given the same CMP treatment as described in chapter 2. Two growth runs were performed, in the first samples (a) and (b) were used which were both etched for 60 s before CMP. The second growth run included the rest of the samples which were etched for (c) and (d) 90 s, and (e) and (f) 30 s.

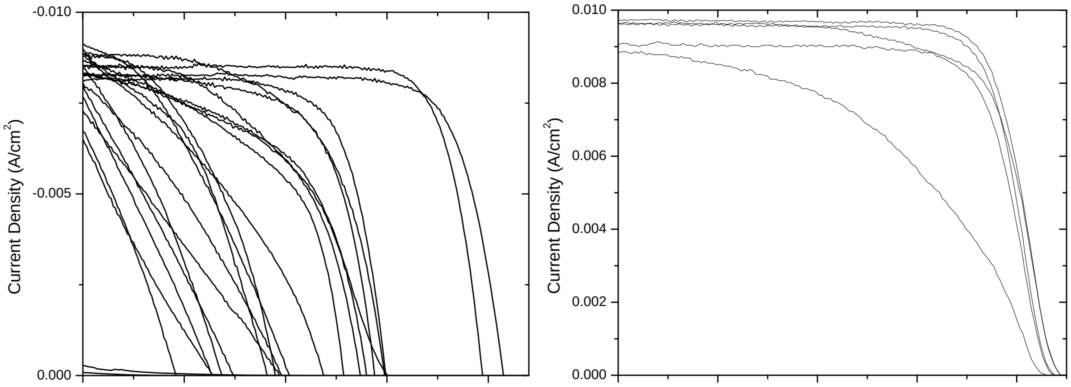

Figure 4.12. Light IV data for all 22 cells on the template that was etched for 30 s and had the best 2 cells of the 110 (left) and data for 5 cells on the bulk Ge control sample (right)

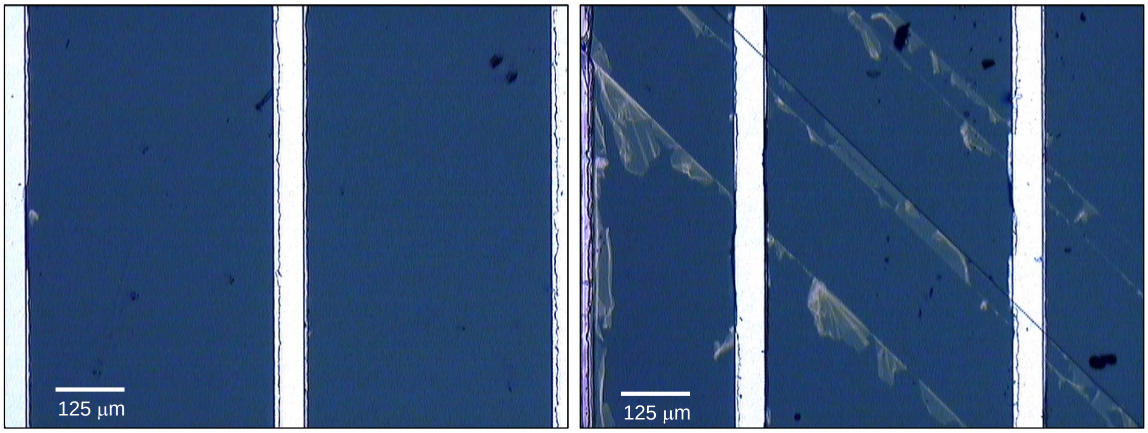

Figure 4.13. Optical micrographs of a good cell (left) and a bad cell (right) showing the source of shunting that is seen in the light IV data. The white bars are the gold top contacts, and the blue area is the III-V active region surface.

Rosakis lab[59] to calculate the stress in the films at each stage of processing. Therefore, measurements would be taken of the sapphire, thin silicon, and thick silicon substrates before bonding, after layer transfer and surface preparation, after growth, and after cell processing. The change in curvature between each step would be used to calculate the stress in the films. Though the before measurements were all taken successfully, layer transfer became a difficulty (see below). Therefore, measurements were taken of older templates that had not been used yet before sending them to Spectrolab for growth. Due to timing difficulties, the samples were not re-measured until after growth and cell processing. At that stage, the surfaces were not consistently reflective enough to provide reasonable data.

When making the epitaxial templates for this final round of growths, ion implantation became a significant problem. In the previous growth rounds no more than six 2" Ge wafers were sent at once to Kroko for ion implantation. For the final round, 16 2" Ge wafers were sent for implant. This was to create templates in sufficient quantity for MOCVD growth optimization for each of the three substrates (Ge/Si, Ge/thin Si and Ge/Al_2O_3). Ion implantation for all 16 wafers took 3 months for Kroko to complete. Unfortunately, layer transfer completely failed on 13 of the 16 wafers. Three Ge wafers transferred as expected. The three wafers were all implanted in the same batch. Two Ge/Si and one Ge/sapphire templates were made. The ion implantaton vendor claimed all 16 wafers were treated identically, whereas the high failure rate and other failed implants from the Atwater group suggested otherwise. The significant cost of ion implantation could not be justified with such a failure rate with no plausible explanation, therefore, a new vendor was sought. Core Systems could not duplicate the process used by Kroko for reasonable cost due to the 9 hour implantation time with low beam current. However, Core Systems has active cooling options (water cooling and liquid N_2 cooling). Minimizing annealing due to implant heating was considered the priority to avoid in-situ exfoliation, so liquid nitrogen cooling with high beam current was chosen. This combination ensured wafer temperatures remained below ambient at all times while minimizing implant time (and hence cost). Unfortunately, following the bonding and exfoliation recipe detailed in Chapter 2 did not result in any exfoliation. To check that the wafers were implanted, a piece of one wafer was placed in the flame of a bunsen burner, which should exceed any needed exfoliation temperature. As expected, the piece did exfoliate completely. Using a standard laboratory hot plate, it was determined that temperatures above 425°C were required for exfoliation. The previous process annealed at 350°C to induce exfoliation. Prior experience showed that the needed exfoliation temperature was higher in the Suss bonder when under pressure than on a hot plate. Therefore, a new process was developed that ramped to 500°C for exfoliation. Around this time Aonex Technologies was heavily using their bonder and the SiC bonding plate broke in the middle of testing this new process.

Though we had preliminary success in creating Ge/sapphire templates, equipment down time and vendor difficulties made it impossible to create the number of substrates needed to properly tune the growth parameters for the different substrates. The primary difficulty with using sapphire is that the heaters in the MOCVD reactor are IR heaters. Therefore, the transparent sapphire substrates do not reach the same temperatures in the reactor as the bulk Ge substrates. In order to properly tune the growth parameters for this type of substrate, several growth runs were needed. In addition, to eliminate the miscut as a variable in further experiments, all Ge was standardized to 6° miscut. Unfortunately, the thin Si cracked in the bonder during processing. This left one growth run with one sapphire template and two thick silicon substrates. The light IV and SR data can be see in figure 4.15. Insufficient samples did not allow for growth optimization; therefore, these samples appear much worse than the previous round. Interestingly, the GaInP cell on the sapphire substrate showed the best external quantum efficiency of the three template samples.

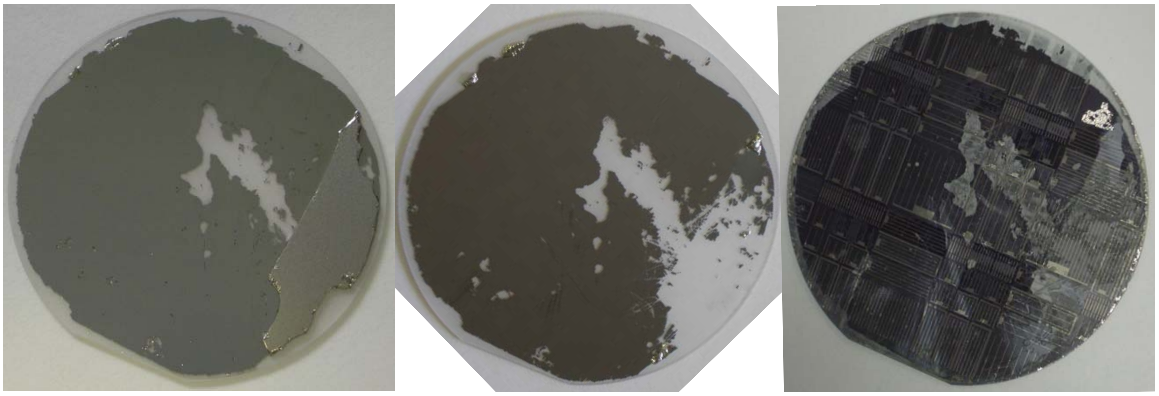

Figure 4.14. Pictures of the Ge/sapphire epitaxial template as-transferred, processed for growth, and after growth and cell processing (left to right)

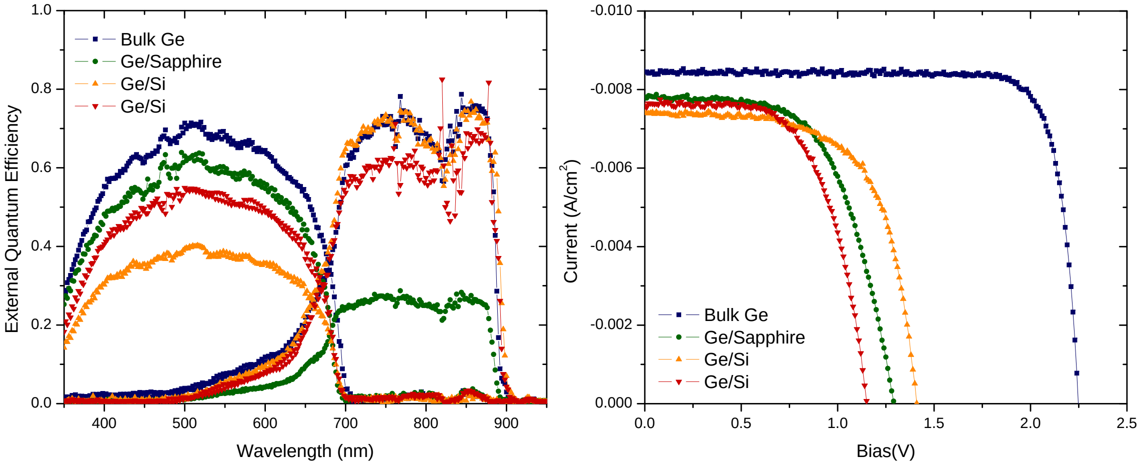

Figure 4.15. Light IV and SR data for Ge/sapphire and Ge/Si epitaxial templates

4.5 Conclusion

Results from four different III-V MOCVD growth rounds have been presented. Through this work significant improvements in performance of devices grown on Ge/Si templates as compared to bulk Ge in the same run have been seen until the devices on epitaxial templates showed comparable performance to those on bulk Ge substrates. However, a thorough understanding of the effects of the coefficient of thermal expansion mismatch and the engineered strain state are still missing from this analysis. All templates were bonded at elevated temperatures, shifting the zero strain state away from room temperature. In an attempt to better understand this effect, Ge/sapphire templates were successfully fabricated, but not in sufficient quantity to optimize growth conditions, primarily the growth temperature.

Chapter 5

Outlook

5.1 Unanswered Questions

5.1.1 Strain Effects

In this thesis, we have shown the first GaInP/GaAs dual junction solar cells on Ge/Si epitaxial templates with comparable performance to cells grown on bulk epi-ready Ge. However, all cells on both Ge/Si templates and bulk Ge were inferior to typical cells grown on bulk Ge. This opens two primary questions; first is whether growth parameters were too far from optimum for a "good" GaInP/GaAs growth on bulk Ge. As this is primarily a MOCVD optimization task, it would be best performed by MOCVD experts such as Spectrolab. The second is what effect the strain state of the overall structure has on device performance. A preliminary attempt was made into understanding the strain state by using Ge/sapphire as well as Ge/Si. Another potential substrate is Ge/Ge templates. In the same way that sputtered SiO2 was applied to the sapphire substrates as a bonding layer, sputtered SiO2 could be used in the creation of Ge/Ge epitaxial templates. Though the structure appears redundant initially, it would provide a substrate with comparable surface properties and no CTE mismatch induced strain.

The only way to fully answer the question of strain effects is to meet two conditions: the growth must be optimized fully for each alternative substrate investigated and the stress must be measured quantitatively. The first requirement translates into a need for many epitaxial templates to be available for test growth runs. In addition, careful substrate temperature measurement for each type of template is required for full growth optimization. The second requirement could be fulfilled by using the CGS300 system in the Rosakis lab[59]. In addition, non-uniformities could be taken into account using an extended form of analysis beyond the Stoney formula, developed in the Rosakis lab[60, 61, 62].

5.1.2 Back Surface Fields and Tunnel Junctions

The analytical model of multijunction solar cells presented here made many assumptions in enabling an analytical solution. The estimated error of these assumptions is comparable to the effects of adding additional physics to the model. In particular, back surface fields and tunnel junctions are crucial in designing good multijunction solar cells. Therefore, further work is needed using finite element modeling approaches to capture the physics of these devices. Synopsys TCAD Sentaurus looks promising for this application. However, the materials data files need careful attention for all materials other than silicon. This includes built-in models for changes in optical properties with doping, and incorporating tunnel junction optical properties. One limitation in working with Sentaurus is that the performance of the device is calculated for each wavelength individually. Therefore, modeling using AM1.5 data would be very computationally intensive as simulation time should increase linearly with each additional wavelength. Judicious spectrum averaging or binning could significantly reduce simulation time while still capturing essential device performance. No optimization routines exist within TCAD Sentaurus making subcell thickness optimization as presented in Chapter 3 difficult. A sensible approach to subcell thickness optimization would be to perform perturbation analysis of the optimum thicknesses obtained from the MATLAB model. This would explore the local efficiency surface. Another key challenge is incorporating material quality changes. Whereas the MATLAB code used minority carrier diffusion length as a proxy for material quality, no equivalent exists in TCAD. Alternative material data files would have to be developed to explore poorer quality materials.

Additionally, incorporating a free carrier absorption model with better accuracy than the Drude model will be important. The Drude model provides an upper limit on losses due to free carrier absorption. Alternative models have been proposed[51]; however, careful inspection reveals potential inconsistencies and therefore difficult implementation.

5.2 Device Integration Possibilities

5.2.1 Lattice Mismatch Accommodation

Unlike metamorphic growth techniques, wafer bonding and layer transfer can readily accommodate any degree of lattice mismatch. For this reason, any combination of materials could be brought together to optimize the performance of the device. Silicon can be used in combination with III-V materials as all restrictions placed on device design by the crystal grower's chart are removed with this technique. This is most important for devices with more than three junctions. Metamorphic growth methods have produced good quality triple junction devices. However, the limitations of metamorphic growth become a problem as more junctions are considered. Larger mismatch is required than metamorphic techniques have been shown to effectively accommodate. The material systems that can be explored to push the efficiencies of multijunction solar cells ever higher are significantly increased when evaluating them in terms of a bonded structure rather than a monolithic epitaxial structure.

5.2.2 Independent Connections

In addition to accommodating any amount of lattice mismatch, wafer bonding and layer transfer open a path for the realization of some of the alternative device electrical connections discussed in the modeling portion of this thesis. For example, the four junction cell proposed in this work, has two lattice matched cells on top of another two lattice matched cells with a wafer bond connecting the two. With this type of design, it is straightforward to imagine independently contacting the top two cells from the bottom two cells; and therefore, setting the operating points of each separately. As shown in chapter 3, this type of connection provides the majority of performance gains achieved by independently connecting each of the four subcells.

5.3 Conclusion

Results have been presented for both experimental and theoretical work on multijunction high efficiency solar cells. The experimental work demonstrated the viability of wafer bonding and layer transfer for creating good quality multijunction solar cells. Critical to this was developing effective processes for remediation of ion implantation induced damage. This was achieved using a combination of chemical etching and chemical mechanical polishing. In addition, this work demonstrated the difficulties associated with high quality III-V MOCVD growth. The growth parameters that produce high quality solar cells on 6° miscut, 300 nm thick epi-ready Ge wafers, are not universal. Optimum growth parameters for any given substrate must be carefully optimized to achieve high quality devices.

In addition, modeling work predicts stable performance over the diurnal cycle if the cell is optimized for off-peak irradiation. The theoretical work also showed that exploring alternative electrical connections other than the two-terminal design currently used could allow for significant performance increases, up to five absolute percent. The model has also shown the dependence on the acceptable series resistance within the device as a function of concentration.

Appendix A

MatLab Codes

In developing a model for multijunction solar cells in Matlab, I divided the calculation into several separate functions. At the outermost level, the model calls a built-in optimization routine (Listing A.1). Unfortunately, the built-in routine has a tendency to get stuck in local minima, so I have designed this function to run multiple times with very different starting points to force the solver to look in different areas of the multivariate space. The final thicknesses of each pn-junction and the overall performance are all saved as the routine runs. This optimization routine calls a function (Listing A.2) that calculates the performance of an overall multijunction device given the IV curves of the individual subcells. The performance of the subcells is calculated in two separate subroutines (Listing A.3 and Listing A.4). The second subroutine is simply a refinement of the initial calculation of the cell IV characteristics in a well-defined bias range. The spectrum that is used by the subcell functions is calculated based on the spectrum output from the subcell above it. To understand this graphically, see Figure A.1.

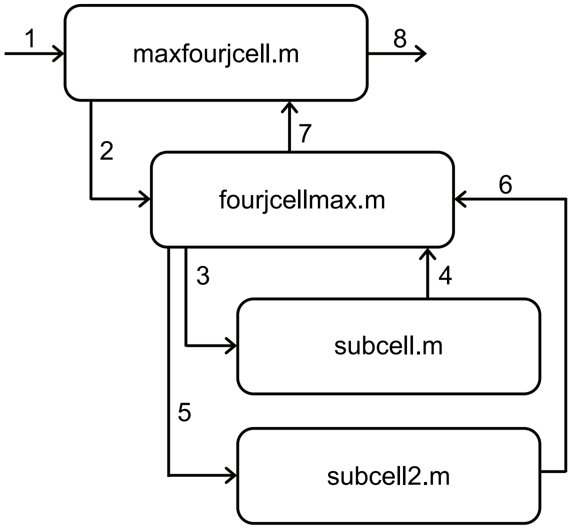

Figure A.1. Flowchart of the order in which the Matlab programs are called. Inputs and outputs are as follows: 1 — diffusion length (global variable), cell thickness initial guess, maximum and minimum cell thicknesses; 2 — cell thicknesses; 3 — solar flux, absorption coefficient, energy vector corresponding to those values, diffusion length, intrinsic carrier concentration, acceptor doping level, donor doping level, empirical mobility model constants, surface recombination velocity, window width, static dielectric constant; 4 — current density, bias, flux out; 5 — solar flux, absorption coefficient, energy vector corresponding to those values, diffusion length, intrinsic carrier concentration, acceptor doping level, donor doping level, empirical mobility model constants, surface recombination velocity, window width, static dielectric constant, new bias range; 6 — current density, bias, flux out; 7 — maximum power; 8 — initial guess, final cell thicknesses, diffusion lengths, maximum power.

Listing A.1. maxfourjcell.m

```
clear all
format short g
tic
global Ln1 Ln2 Ln3 Ln4

L0v=[4e-5,6e-5,8e-5,10e-5,12e-5,14e-5,16e-5,18e-5,20e-5,22e-5,24e-5,26e-5,
     28e-5,30e-5,32e-5,34e-5,36e-5,38e-5,40e-5,42e-5,44e-5,46e-5,48e-5];
Lnv=[2e-6,4e-6,6e-6,8e-6,1e-5,2e-5,4e-5,6e-5,8e-5,1e-4,2e-4,4e-4,6e-4,8e-4,
     1e-3,2e-3,4e-3,6e-3,8e-3,1e-2];

mm=length(L0v);
nn=length(Lnv);
Constants=zeros(6,nn*mm);
%Lv=zeros(4,nn*mm);
maxP=zeros(nn*mm,3);



for k=1:mm;
    for j=1:nn;
        Ln1=Lnv(j);
        Ln2=Lnv(j);
        Ln3=Lnv(j);
        Ln4=Lnv(j);
        L0=[L0v(k);L0v(k);L0v(k)];
        lb=[2e-5;2e-5;2e-5];
        ub=[5e-4;5e-4;5e-4];
        options = optimset('TolX',1e-9);
        [L,fval,exitflag,output] = fmincon(@fourjcellmax_v3,L0,[],[],[],[],lb,
                                           ub,[],options);
        Constants(:,j+(k-1)*nn)=[L0v(k);Ln1;L;5e-4];
        maxP(j+(k-1)*nn,:)=[L0v(k),Ln1,fval];
    end
end

%save('Lv', 'Lv');
save (strcat('L','.txt'), 'Constants', '-ascii');
save (strcat('P','.txt'), 'maxP', '-ascii');
toc
```

```
t=toc
save('t_maxfourjcell.txt', 't', '-ascii');
```

Listing A.2. fourjcellmax.m

```
function [maxP1] = fourjcellmax_v3(L)

load E_flux_alpha
load Constants9
global Ln1 Ln2 Ln3 Ln4



%Cell 1 - GaInP
[J1,bias1,fluxout1] = subcell_v3(E, flux, alpha1, L(1), ni1, Nd1, Na1,
     munmax1, munmin1, Nnref1, lambdan1, theta1n1, theta2n1, mupmax1,
     mupmin1, Npref1, lambdap1, theta1p1, theta2p1, Sn1, Sp1, windowwidth1,
     Ln1, epsilon1, Eg1, Egtot);

%Cell 2 - GaAs
[J2,bias2,fluxout2] = subcell_v3(E, fluxout1, alpha2, L(2), ni2, Nd2, Na2,
     munmax2, munmin2, Nnref2, lambdan2, theta1n2, theta2n2, mupmax2,
     mupmin2, Npref2, lambdap2, theta1p2, theta2p2, Sn2, Sp2, windowwidth2,
     Ln2, epsilon2, Eg2, Egtot);

%Transferred layer
%[fluxoutw] = window(E, fluxout2, alphaw, Lw, windowwidthw);

%Cell 3 - InGaAsP
[J3,bias3,fluxout3] = subcell_v3(E, fluxout2, alpha3, L(3), ni3, Nd3, Na3,
     munmax3, munmin3, Nnref3, lambdan3, theta1n3, theta2n3, mupmax3,
     mupmin3, Npref3, lambdap3, theta1p3, theta2p3, Sn3, Sp3, windowwidth3,
     Ln3, epsilon3, Eg3, Egtot);

%Cell 4 - InGaAs
[J4,bias4,fluxout4] = subcell_v3(E, fluxout3, alpha4, 5e-4, ni4, Nd4, Na4,
     munmax4, munmin4, Nnref4, lambdan4, theta1n4, theta2n4, mupmax4,
     mupmin4, Npref4, lambdap4, theta1p4, theta2p4, Sn4, Sp4, windowwidth4,
     Ln4, epsilon4, Eg4, Egtot);
```

```
if ((sum(J1>-0.5))==length(bias1)&&sum(J1>0.5)==0)
    bias1new=bias1(sum(J1>0.5)+1:sum(J1>-0.5));
elseif ((sum(J1>-0.5))<length(bias1)&&sum(J1>0.5)==0)
    bias1new=bias1(sum(J1>0.5)+1:sum(J1>-0.5)+1);
elseif ((sum(J1>-0.5))==length(bias1)&&sum(J1>0.5)>0)
    bias1new=bias1(sum(J1>0.5)+1:sum(J1>-0.5));
else
    bias1new=bias1(sum(J1>0.5):sum(J1>-0.5)+1);
end
if ((sum(J2>-0.5))==length(bias2)&&sum(J2>0.5)==0)
    bias2new=bias2(sum(J2>0.5)+1:sum(J2>-0.5));
elseif ((sum(J2>-0.5))<length(bias2)&&sum(J2>0.5)==0)
    bias2new=bias2(sum(J2>0.5)+1:sum(J2>-0.5)+1);
elseif ((sum(J2>-0.5))==length(bias2)&&sum(J2>0.5)>0)
    bias2new=bias2(sum(J2>0.5)+1:sum(J2>-0.5));
else
    bias2new=bias2(sum(J2>0.5):sum(J2>-0.5)+1);
end
if ((sum(J3>-0.5))==length(bias3)&&sum(J3>0.5)==0)
    bias3new=bias3(sum(J3>0.5)+1:sum(J3>-0.5));
elseif ((sum(J3>-0.5))<length(bias3)&&sum(J3>0.5)==0)
    bias3new=bias3(sum(J3>0.5)+1:sum(J3>-0.5)+1);
elseif ((sum(J3>-0.5))==length(bias3)&&sum(J3>0.5)>0)
    bias3new=bias3(sum(J3>0.5)+1:sum(J3>-0.5));
else
    bias3new=bias3(sum(J3>0.5):sum(J3>-0.5)+1);
end
if ((sum(J4>-0.5))==length(bias4)&&sum(J4>0.5)==0)
    bias4new=bias4(sum(J4>0.5)+1:sum(J4>-0.5));
elseif ((sum(J4>-0.5))<length(bias4)&&sum(J4>0.5)==0)
    bias4new=bias4(sum(J4>0.5)+1:sum(J4>-0.5)+1);
elseif ((sum(J4>-0.5))==length(bias4)&&sum(J4>0.5)>0)
    bias4new=bias4(sum(J4>0.5)+1:sum(J4>-0.5));
else
    bias4new=bias4(sum(J4>0.5):sum(J4>-0.5)+1);
end

clear J1 J2 J3 J4 bias1 bias2 bias3 bias4 fluxout1 fluxout2 fluxout3 fluxout4
```

```
%Cell 1 — GaInP
[J1,bias1,fluxout1] = subcell2_v3(E, flux, alpha1, L(1), ni1, Nd1, Na1,
     munmax1, munmin1, Nnref1, lambdan1, theta1n1, theta2n1, mupmax1,
     mupmin1, Npref1, lambdap1, theta1p1, theta2p1, Sn1, Sp1, windowwidth1,
     Ln1, epsilon1, Eg1, Egtot, bias1new);

%Cell 2 — GaAs
[J2,bias2,fluxout2] = subcell2_v3(E, fluxout1, alpha2, L(2), ni2, Nd2, Na2,
     munmax2, munmin2, Nnref2, lambdan2, theta1n2, theta2n2, mupmax2,
     mupmin2, Npref2, lambdap2, theta1p2, theta2p2, Sn2, Sp2, windowwidth2,
     Ln2, epsilon2, Eg2, Egtot, bias2new);

%Transferred layer
%[fluxoutw] = window(E, fluxout2, alphaw, Lw, windowwidthw);

%Cell 3 — InGaAsP
[J3,bias3,fluxout3] = subcell2_v3(E, fluxout2, alpha3, L(3), ni3, Nd3, Na3,
     munmax3, munmin3, Nnref3, lambdan3, theta1n3, theta2n3, mupmax3,
     mupmin3, Npref3, lambdap3, theta1p3, theta2p3, Sn3, Sp3, windowwidth3,
     Ln3, epsilon3, Eg3, Egtot, bias3new);

%Cell 4 — InGaAs
[J4,bias4,fluxout4] = subcell2_v3(E, fluxout3, alpha4, 5e—4, ni4, Nd4, Na4,
     munmax4, munmin4, Nnref4, lambdan4, theta1n4, theta2n4, mupmax4,
     mupmin4, Npref4, lambdap4, theta1p4, theta2p4, Sn4, Sp4, windowwidth4,
     Ln4, epsilon4, Eg4, Egtot, bias4new);

bias1=bias1(J1<0.5);
bias2=bias2(J2<0.5);
bias3=bias3(J3<0.5);
bias4=bias4(J4<0.5);

J1=J1(J1<0.5);
J2=J2(J2<0.5);
J3=J3(J3<0.5);
J4=J4(J4<0.5);

bias1=bias1(J1>—0.5);
```

```
bias2=bias2(J2>-0.5);
bias3=bias3(J3>-0.5);
bias4=bias4(J4>-0.5);

J1=J1(J1>-0.5);
J2=J2(J2>-0.5);
J3=J3(J3>-0.5);
J4=J4(J4>-0.5);

J=[J1,J2,J3,J4];
J=sort(J);
J=-J;
J=sort(J);
J=-J;
dJ=J(2:length(J))-J(1:(length(J)-1));
J=[J(dJ≠0),J(length(J))];

V1=spline(J1,bias1,J);
V2=spline(J2,bias2,J);
V3=spline(J3,bias3,J);
V4=spline(J4,bias4,J);

V=V1+V2+V3+V4;

%Vr=V-(Rs.*J);

P=J.*V;
P(P<0)=0;
[maxP,posn]=max(P);

maxP1=-maxP;
```

Listing A.3. subcell.m

```
function [J,bias,fluxout] = subcell_v3(E, flux, alpha, L, ni, Nd, Na, munmax,
     munmin, Nnref, lambdan, theta1n, theta2n, mupmax, mupmin, Npref, lambdap,
     theta1p, theta2p, Sn, Sp, windowwidth, Ln, epsilon, Eg, Egtot)
```

```
n=length(E)-1;
dE=(E(2:(n+1))-E(1:n));
alpha2=alpha(2:(n+1));
alpha1=alpha2;

gammaA=flux(2:(n+1));

%Define constants
q=1.60219e-19;
kB=1.3807e-23;
T=300;

%Low-field mobility model M.Sotoodeh
mun=munmin+(munmax*((300/T)^theta1n)-munmin)/
                    (1+((Nd/(Nnref*((T/300)^theta2n)))^lambdan));
mup=mupmin+(mupmax*((300/T)^theta1p)-mupmin)/
                    (1+((Na/(Npref*((T/300)^theta2p)))^lambdap));

Dn=kB*T/q*mun;
Dp=kB*T/q*mup;

sigman=1e-15;   %electron capture cross-section
sigmap=sigman;  %hole capture cross-section
vth=1e7;    %doesn't matter as it is multiplied and divided out

Nr=Dn/(Ln^2*sigman*vth);    %trap density
taun0=1/(sigman*Nr*vth);    %lifetime = Ln^2/Dn
taup0=1/(sigmap*Nr*vth);
taun=taun0;
taup=taup0;
Lp=sqrt(taup*Dp);

epsilon0=8.85418e-14;
epsilonp=epsilon*epsilon0;
epsilonn=epsilon*epsilon0;

np0=ni^2/Na;
pn0=ni^2/Nd;
Vbimax=kB*T/q*log(Na*Nd/ni^2);
```

```
V=linspace(-2*Vbimax,99/100*Vbimax);

NN=length(V);
Vbi=zeros(1,NN);
bias=zeros(1,NN);

x2maxmax=sqrt(2*epsilonn*epsilonp*Na*Vbimax/(q*Nd*(Na*epsilonp+Nd*epsilonn)));
x3maxmax=sqrt(2*epsilonn*epsilonp*Nd*Vbimax/(q*Na*(Na*epsilonp+Nd*epsilonn)));

if x2maxmax>windowwidth
    windowwidth=x2maxmax;
end

if (x2maxmax+x3maxmax)≥L
    x2j=x2maxmax*L/(x2maxmax+x3maxmax);
    x3j=x3maxmax*L/(x2maxmax+x3maxmax);
    windowwidth=x2j;
    Vbi(:)=q*Nd/(2*epsilonn)*x2j^2+q*Na/(2*epsilonp)*x3j^2;
    Vbin=q*Nd/(2*epsilonn)*x2j^2+q*Na/(2*epsilonp)*x3j^2;
    bias=linspace(-2*Vbin,99/100*Vbin);
else
    Vbi(:)=Vbimax;
    bias(:)=V(:);
end



x2max=sqrt(2*epsilonn*epsilonp*Na*(Vbi-bias)/(q*Nd*(Na*epsilonp+Nd*epsilonn)));
x3max=sqrt(2*epsilonn*epsilonp*Nd*(Vbi-bias)/(q*Na*(Na*epsilonp+Nd*epsilonn)));

x1=zeros(1,NN); %initializing the thickness vectors
x2=zeros(1,NN);
x3=zeros(1,NN);
x4=zeros(1,NN);

aa=find((x2max+x3max)≥L);
aa2=find((x2max+x3max)<L);
bb = find(x2max(aa2)≥windowwidth);
cc = find(x2max(aa2)<windowwidth);
if size(aa,2)>0
```

```
    x4(aa)=0;
    x1(aa)=0;
    x2(aa)=windowwidth;
    x3(aa)=L−windowwidth;
    if size(bb,2)>0
        x1(bb+max(aa))=0;
        x2(bb+max(aa))=x2max(bb+max(aa));
        x3(bb+max(aa))=x3max(bb+max(aa));
        x4(bb+max(aa))=L−x1(bb+max(aa))−x2(bb+max(aa))−x3(bb+max(aa));
    end
    if size(cc,2)>0
        x1(cc+max(aa))=windowwidth−x2max(cc+max(aa));
        x2(cc+max(aa))=x2max(cc+max(aa));
        x3(cc+max(aa))=x3max(cc+max(aa));
        x4(cc+max(aa))=L−x1(cc+max(aa))−x2(cc+max(aa))−x3(cc+max(aa));
    end
else
    if size(bb,2)>0
        x1(bb)=0;
        x2(bb)=x2max(bb);
        x3(bb)=x3max(bb);
        x4(bb)=L−x1(bb)−x2(bb)−x3(bb);
    end
    if size(cc,2)>0
        x1(cc)=windowwidth−x2max(cc);
        x2(cc)=x2max(cc);
        x3(cc)=x3max(cc);
        x4(cc)=L−x1(cc)−x2(cc)−x3(cc);
    end
end
if size(aa,2)<NN && size(bb,2)==0 && size(cc,2)==0
    disp('error')
    return
end

d1=x1+x2;
d2=x3+x4;
gammaC=(flux(2:(n+1))*ones(1,NN)).*exp(−alpha1*d1−alpha2*x3);
```

```
JlAperE=-((q*gammaA.*dE./(1-alpha1.^(-2)*Lp^(-2))*ones(1,NN)).*
     (((Sn./(alpha1*Dp))*ones(1,NN)+ones(n,NN)-exp(-alpha1*x1).*
        ((Sn./(alpha1*Dp))*cosh(x1./Lp)+(1./(alpha1*Lp))*sinh(x1./Lp)))./
           (ones(n,1)*(Sn*Lp/Dp.*sinh(x1./Lp)+cosh(x1./Lp)))-exp(-alpha1*x1)));
JlCperE=-(((q*dE./(1-alpha2.^(-2)*Ln^(-2))*ones(1,NN)).*gammaC).*
     (1-1./(alpha2*Ln)*ones(1,NN).*
          ((Sp*Ln/Dn*(ones(n,1)*cosh(x4/Ln)-exp(-alpha2*x4)))
               +ones(n,1)*sinh(x4./Ln)+alpha2*ones(1,NN)*Ln.*exp(-alpha2*x4))./
                    (ones(n,1)*(Sp*Ln/Dn*sinh(x4/Ln)+cosh(x4/Ln)))));
JdepperE=-q*gammaA.*dE*ones(1,NN).*exp(-alpha1*x1).*
                                        (1-exp(-alpha1*x2-alpha2*x3));


JlA=sum(JlAperE,1);
JlC=sum(JlCperE,1);
Jgdep=sum(JdepperE,1);


J0A=-q*Dp*pn0/Lp*(Sn*Lp/Dp*cosh(x1/Lp)+sinh(x1/Lp))./
                    (Sn*Lp/Dp*sinh(x1/Lp)+cosh(x1/Lp));
J0C=-q*Dn*np0/Ln*(Sp*Ln/Dn*cosh(x4/Ln)+sinh(x4/Ln))./
                    (Sp*Ln/Dn*sinh(x4/Ln)+cosh(x4/Ln));


Jrdep=-q*ni.*(x2+x3)./sqrt(taun0*taup0).*
          (2.*sinh(q.*bias./(2*kB*T))./(q.*(Vbi-bias)./(kB*T))).*pi/2;


fluxout=flux(1:(n+1)).*exp(-alpha*windowwidth-alpha*(L-windowwidth));


ii=find(bias>Vbi);
if size(ii,2)>0
    J0A(min(ii):NN)=0;
    J0C(min(ii):NN)=0;
    JlA(min(ii):NN)=0;
    JlC(min(ii):NN)=0;
    Jgdep(min(ii):NN)=0;
    Jrdep(min(ii):NN)=0;
    bias(min(ii):NN)=0;
end


Jl=JlA+JlC+Jgdep;
J0=J0A+J0C;
```

```
J=(J0.*(exp(q*bias/(kB*T))-1)-Jl+Jrdep);
```

Listing A.4. subcell2.m

```
function [J,bias,fluxout] = subcell2_v3(E, flux, alpha, L, ni, Nd, Na, munmax,
     munmin, Nnref, lambdan, theta1n, theta2n, mupmax, mupmin, Npref, lambdap,
     theta1p, theta2p, Sn, Sp, windowwidth, Ln, epsilon, Eg, Egtot, V1)

n=length(E)-1;
dE=(E(2:(n+1))-E(1:n));
alpha2=alpha(2:(n+1));
alpha1=alpha2;

gammaA=flux(2:(n+1));

%Define constants
q=1.60219e-19;
kB=1.3807e-23;
T=300;

%Low-field mobility model M.Sotoodeh
mun=munmin+(munmax*((300/T)^theta1n)-munmin)/
                              (1+((Nd/(Nnref*((T/300)^theta2n)))^lambdan));
mup=mupmin+(mupmax*((300/T)^theta1p)-mupmin)/
                              (1+((Na/(Npref*((T/300)^theta2p)))^lambdap));

Dn=kB*T/q*mun;
Dp=kB*T/q*mup;

sigman=1e-15;
sigmap=sigman;
vth=1e7;

Nr=Dn/(Ln^2*sigman*vth);
taun0=1/(sigman*Nr*vth);
taup0=1/(sigmap*Nr*vth);
taun=taun0;
taup=taup0;
```

```
Lp=sqrt(taup*Dp);

epsilon0=8.85418e-14;
epsilonp=epsilon*epsilon0;
epsilonn=epsilon*epsilon0;

np0=ni^2/Na;
pn0=ni^2/Nd;
Vbimax=kB*T/q*log(Na*Nd/ni^2);
V=linspace(min(V1),max(V1),200);

NN=length(V);
Vbi=zeros(1,NN);

x2maxmax=sqrt(2*epsilonn*epsilonp*Na*Vbimax/(q*Nd*(Na*epsilonp+Nd*epsilonn)));
x3maxmax=sqrt(2*epsilonn*epsilonp*Nd*Vbimax/(q*Na*(Na*epsilonp+Nd*epsilonn)));

if x2maxmax>windowwidth
    windowwidth=x2maxmax;
end

if (x2maxmax+x3maxmax)≥L
    x2j=x2maxmax*L/(x2maxmax+x3maxmax);
    x3j=x3maxmax*L/(x2maxmax+x3maxmax);
    windowwidth=x2j;
    Vbi(:)=q*Nd/(2*epsilonn)*x2j^2+q*Na/(2*epsilonp)*x3j^2;
    Vbin=q*Nd/(2*epsilonn)*x2j^2+q*Na/(2*epsilonp)*x3j^2;
else
    Vbi(:)=Vbimax;
end

bias=V;
x2max=sqrt(2*epsilonn*epsilonp*Na*(Vbi-bias)/(q*Nd*(Na*epsilonp+Nd*epsilonn)));
x3max=sqrt(2*epsilonn*epsilonp*Nd*(Vbi-bias)/(q*Na*(Na*epsilonp+Nd*epsilonn)));

x1=zeros(1,NN); %initializing the thickness vectors
x2=zeros(1,NN);
x3=zeros(1,NN);
x4=zeros(1,NN);
```

```
aa=find((x2max+x3max)≥L);
aa2=find((x2max+x3max)<L);
bb = find(x2max(aa2)≥windowwidth);
cc = find(x2max(aa2)<windowwidth);
if size(aa,2)>0
    x4(aa)=0;
    x1(aa)=0;
    x2(aa)=x2max(aa)*L/(x2max(aa)+x3max(aa));
    x3(aa)=x3max(aa)*L/(x2max(aa)+x3max(aa));
    if size(bb,2)>0
        x1(bb+max(aa))=0;
        x2(bb+max(aa))=x2max(bb+max(aa));
        x3(bb+max(aa))=x3max(bb+max(aa));
        x4(bb+max(aa))=L−x1(bb+max(aa))−x2(bb+max(aa))−x3(bb+max(aa));
    end
    if size(cc,2)>0
        x1(cc+max(aa))=windowwidth−x2max(cc+max(aa));
        x2(cc+max(aa))=x2max(cc+max(aa));
        x3(cc+max(aa))=x3max(cc+max(aa));
        x4(cc+max(aa))=L−x1(cc+max(aa))−x2(cc+max(aa))−x3(cc+max(aa));
    end
else
    if size(bb,2)>0
        x1(bb)=0;
        x2(bb)=x2max(bb);
        x3(bb)=x3max(bb);
        x4(bb)=L−x1(bb)−x2(bb)−x3(bb);
    end
    if size(cc,2)>0
        x1(cc)=windowwidth−x2max(cc);
        x2(cc)=x2max(cc);
        x3(cc)=x3max(cc);
        x4(cc)=L−x1(cc)−x2(cc)−x3(cc);
    end
end
if size(aa,2)<NN && size(bb,2)==0 && size(cc,2)==0
    disp('error')
    return
```

```
end


d1=x1+x2;
d2=x3+x4;
gammaC=(flux(2:(n+1))*ones(1,NN)).*exp(-alpha1*d1-alpha2*x3);


JlAperE=-((q*gammaA.*dE./(1-alpha1.^(-2)*Lp^(-2))*ones(1,NN)).*
     (((Sn./(alpha1*Dp))*ones(1,NN)+ones(n,NN)-exp(-alpha1*x1).*
        ((Sn./(alpha1*Dp))*cosh(x1./Lp)+(1./(alpha1*Lp))*sinh(x1./Lp)))./
           (ones(n,1)*(Sn*Lp/Dp.*sinh(x1./Lp)+cosh(x1./Lp)))-exp(-alpha1*x1)));
JlCperE=-(((q*dE./(1-alpha2.^(-2)*Ln^(-2))*ones(1,NN)).*gammaC).*
     (1-1./(alpha2*Ln)*ones(1,NN).*
          ((Sp*Ln/Dn*(ones(n,1)*cosh(x4/Ln)-exp(-alpha2*x4)))
               +ones(n,1)*sinh(x4./Ln)+alpha2*ones(1,NN)*Ln.*exp(-alpha2*x4))./
                    (ones(n,1)*(Sp*Ln/Dn*sinh(x4/Ln)+cosh(x4/Ln)))));
JdepperE=-q*gammaA.*dE*ones(1,NN).*exp(-alpha1*x1).*
                                        (1-exp(-alpha1*x2-alpha2*x3));


JlA=sum(JlAperE,1);
JlC=sum(JlCperE,1);
Jgdep=sum(JdepperE,1);


J0A=-q*Dp*pn0/Lp*(Sn*Lp/Dp*cosh(x1/Lp)+sinh(x1/Lp))./
                    (Sn*Lp/Dp*sinh(x1/Lp)+cosh(x1/Lp));
J0C=-q*Dn*np0/Ln*(Sp*Ln/Dn*cosh(x4/Ln)+sinh(x4/Ln))./
                    (Sp*Ln/Dn*sinh(x4/Ln)+cosh(x4/Ln));


Jrdep=-q*ni.*(x2+x3)./sqrt(taun0*taup0).*
          (2.*sinh(q.*bias./(2*kB*T))./(q.*(Vbi-bias)./(kB*T))).*pi/2;


fluxout=flux(1:(n+1)).*exp(-alpha*windowwidth-alpha*(L-windowwidth));


ii=find(bias>Vbi);
if size(ii,2)>0
    J0A(min(ii):NN)=0;
    J0C(min(ii):NN)=0;
    JlA(min(ii):NN)=0;
    JlC(min(ii):NN)=0;
    Jgdep(min(ii):NN)=0;
```

```
    Jrdep(min(ii):NN)=0;
    bias(min(ii):NN)=0;
end

Jl=JlA+JlC+Jgdep;
J0=J0A+J0C;
J=(J0.*(exp(q*bias/(kB*T))-1)-Jl+Jrdep);
```

Appendix B

Material Constants Used in Modeling Work

One of the challenges in constructing a model for the four junction device is the lack of good data for all the materials. GaAs is well-known and understood. However, GaInAsP is not very well known. Unfortunately, many of the material properties can be strongly affected by growth methods and procedures. As there is very little data on the quaternary alloy, much of the data used was interpolated from data for the binary alloys that make up the quaternary. In this section, I have gathered together all of the data used as inputs into my modeling work.

The absorption coefficients are very important in the calculation of the performance of the overall device. Unfortunately, there aren't any sources of data for alpha of the quaternary alloy. The absorption coefficients used are shown below. The absorption coefficient for the quarternary alloy was obtained by extrapolating an experimental data set. There is significant error in that absorption coefficient, so work is ongoing to use a spectroscopic ellipsometer to better characterize the absorption coefficient of that material and several of the other III-V alloys.

The material constants for GaAs used in COMSOL Multiphysics modeling work are shown in tables B.4, B.5.

Table B.1. Material constants used in the model

Material	n_r	n_i (cm^{-2})	m_n	m_p	S_n (cm/s)	S_p (cm/s)	ϵ
$Ga_{0.51}In_{0.49}P$	11.8	1.99×10^2	0.067	0.7	4000	1.5	11.8
GaAs	12.9	2.10×10^6	0.088	0.51	1000	1000	12.9
$Ga_{0.19}In_{0.81}As_{0.37}P_{0.63}$	13.4	2.75×10^9	0.041	0.48	1000	1000	13.4
$Ga_{0.47}In_{0.53}As$	13.9	1.63×10^{12}	0.059	0.45	1000	1000	13.9

Table B.2. Fit parameters for each material used in the mobility model[52]

Material	electron or hole	$\mu_{max}\,(300k)$ (cm^2/V·s)	μ_{min} (cm^2/V·s)	N$_{ref}\,(300K)$ (cm^{-3})	λ	θ_1	θ_2
$Ga_{0.51}In_{0.49}P$	electron	4300	400	2.0×10^{16}	0.70	1.66	1.95
	hole	150	15	1.5×10^{17}	0.80	2.0	1.47
GaAs	electron	9400	500	6.0×10^{16}	0.394	2.1	3.0
	hole	492	20	1.48×10^{17}	0.38	2.2	3.0
$Ga_{0.19}In_{0.81}As_{0.37}P_{0.63}$	electron	3771	99	9.76×10^{16}	0.517	1.39	3.01
	hole	104	13	2.36×10^{17}	0.606	1.58	2.64
$Ga_{0.47}In_{0.53}As$	electron	14000	300	1.3×10^{16}	0.48	1.59	3.68
	hole	320	10	4.9×10^{17}	0.403	1.59	3.0

Table B.3. Material constants used in the universal model of band gap as a function of temperature

Material	E_g (0) eV	α (10^{-4}eVK^{-1})	β (K)
$Ga_{0.51}In_{0.49}P$	2.011[63]	5.2[63]	190[63]
GaAs	1.519[64]	5.4051.519[64]	2041.519[64]
$Ga_{0.19}In_{0.81}As_{0.37}P_{0.63}$	1.30065[65]	5.26319[65]	260[65]
$Ga_{0.47}In_{0.53}As$	0.81[66]	4.91[66]	301[66]

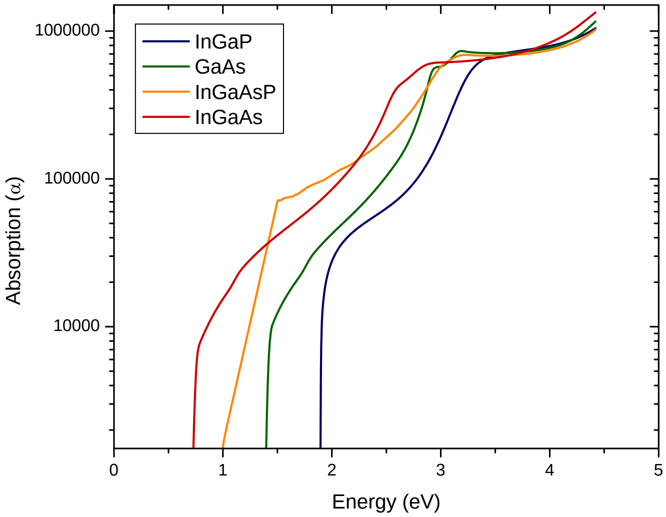

Figure B.1. Absorption coefficients used in the modeling work for GaInP[67], GaAs, GaInAsP[68], and GaInAs

Table B.4. Material constants used in COMSOL Multiphysics: Part I

Name	Expression	Value	Description
mun	8500[cm^2*V^-1*s^-1]	0.85[m^2/(s·V)]	Electron Mobility
mup	400[cm^2*V^-1*s^-1]	0.04[m^2/(s·V)]	Hole Mobility
q	1.602e-19[C]	(1.602e-19)[C]	Electronic Charge
k	1.38e-23[J/K]	(1.38e-23)[m^2·kg/(s^2·K)]	Boltzmann's Constant
T	300[K]	300[K]	Temperature
epsilonr	12.9	12.9	Static Dielectric Constant
ni	2.1e6[cm^-3]	2.1e12[1/m^3]	Intrinsic Carrier Concentration
Dn	k*T/q*mun	0.021966[m^2/s]	Electron Diffusivity
Dp	k*T/q*mup	0.001034[m^2/s]	Hole Diffusivity
mn	0.063	0.063	electron effective mass
mp	0.51	0.51	hole effective mass
Na	1e17[cm^-3]	10e22[1/m^3]	p-type doping
Nd	1e18[cm^-3]	10e23[1/m^3]	n-type doping
Eg	2.2815e-19[J]	(2.2815e-19)[J]	Band Gap
FnFp	Eg-k*T*log((mn/mp)^(3/2)*(Na/Nd))	(2.506695e-19)[J]	Difference in Fermi levels between the n and p-type material for a homojunction

Table B.5. Material constants used in COMSOL Multiphysics: Part II

Name	Expression	Value	Description
nn0	1e18[cm^-3]	10e23[1/m^3]	Initial Electron Density in the n-type region
pp0	1e17[cm^-3]	10e22[1/m^3]	Initial Hole Density in the p-type region
np0	ni^2/Na	44.1[1/m^3]	Initial Electron Density in the p-type region
pn0	ni^2/Nd	4.41[1/m^3]	Initial Hole Density in the n-type region
taun	5e-9[s]	(5e-9)[s]	Electron Lifetime
taup	3e-6[s]	(3e-6)[s]	Hole Lifetime
Sn	1e5[cm/s]	1000[m/s]	Electron Surface Recombination Velocity
Sp	1e5[cm/s]	1000[m/s]	Hole Surface Recombination Velocity
X	6.5209e-19[J]	(6.5209e-19)[J]	Electron Affinity
Va	0[V]	0[V]	Starting applied bias
V_junction	FnFp/q	1.564729[V]	
A	3000	3000	Constants for initializing the built-in field
d1	5e-6	5e-6	Constants for initializing the built-in field
d2	2e-7	2e-7	Constants for initializing the built-in field
B	-2.5	-2.5	Constants for initializing the built-in field
C	0.5	0.5	Constants for initializing the built-in field

Bibliography

[1] T. Trupke, M. A. Green, and P. Wurfel. Improving solar cell efficiencies by up-conversion of sub-band-gap light. *Journal of Applied Physics*, 92(7):4117–4122, 2002.

[2] T. Trupke, M. A. Green, and P. Wurfel. Improving solar cell efficiencies by down-conversion of high-energy photons. *Journal of Applied Physics*, 92(3):1668–1674, 2002.

[3] G. Conibeer. Third generation photovoltaics. *Materials Today*, 10:42–50, 20077.

[4] C. Strumpel, M. McCann, G. Beaucarne, V. Arkhipov, A. Slaui, V. Svrcek, C. del Canizo, and I. Tobias. Modifying the solar spectrum to enhance silicon solar cell efficiency — an overview of available materials. *Solar Energy Materials and Solar Cells*, 91:238–249, 2007.

[5] A. Luque and A. Marti. Increasing the efficiency of ideal solar cells by photon induced transitions at intermediate levels. *Physical Review Letters*, 78(26):5014–5017, 1997.

[6] A. Luque and A. Marti. A metallic intermediate band high efficiency solar cell. *Progress in Photovoltaics: Research and Applications*, 9(2):73–86, 2001.

[7] R. Ross and A. Nozik. Efficiency of hot-carrier solar energy converters. *Journal of Applied Physics*, 53(5):3813–3818, 1982.

[8] R. R King, D. C. Law, C. M. Fetzer, R. A. Sherif, K. M. Edmondson, S. Kurtz, G. S. Kinsey, H. L. Cotal, D. D. Krut, J. H. Ermer, and N. H. Karam. Pathways to 40 percent-efficient concentrator photovoltaics. In *Proceedings of the 20th European Photovoltaic Solar Energy Conference*, Barcelona, Spain, 2005.

[9] M. Wanlass, P. Ahrenkiel, D. Albin, J. Carapella, A. Duda, K. Emery, D. Friedman, J. Geisz, K. Jones, A. Kibbler, J. Kiehl, S. Kurtz, W. McMahon, T. Moriarty, J. Ol-

son, A. Ptak, M. Romero, and S. Ward. Monolithic, ultra-thin GaInP/GaAs/GaInAs tandem solar cells. In *4th World Conference on Photovoltaic Energy Conversion*, pages 729–732, Waikoloa, Hawaii, 2006. IEEE.

[10] James M. Zahler. *Materials integrations for high performance photovoltaics by wafer bonding.* PhD thesis, California Institute of Technology, 2005.

[11] E. A. Fitzgerald. Dislocations in strained-layer epitaxy: theory, experiment, and applications. *Materials Science Reports*, 7:87–142, 1991.

[12] R. Beanland, D. J. Dunstan, and P. J. Goodhew. Plastic relaxation and relaxed buffer layers for semiconductor epitaxy. *Advances in Physics*, 45(2):87–146, 1996.

[13] E. A. Fitzgerald, Y.-H. Xie, D. Monroe, P. J. Silverman, J. M. Kuo, A. R. Kortan, F. A. Theil, and B. E. Weir. Relaxed Ge_xSi_{1-x} structures for III-V integration with Si and high mobility two-dimensional electron gases in Si. *Journal of Vacuum Science and Technology B*, 10(4):1807–1819, 1992.

[14] T. P. Chin, J. C. P. Chang, K. L. Kavanagh, C. W. Tu, P. D. Kirchner, and J. M. Woodall. Gas-source molecular beam epitaxial growth, characterization, and light-emitting diode application of $In_xGa_{1-x}P$ on GaP(100). *Applied Physics Letters*, 62(19):2369–2371, 1993.

[15] Y. H. Xie, E. A. Fitzgerald, and P. J. Silverman. Fabrication and application of relaxed buffer layers. *Materials Science and Engineering B*, 30:201–203, 1995.

[16] F. Romanato, E. Napolitani, A. Camera, A. V. Drigo, L. Lazzarini, G. Salviati, C. Ferrari, A. Bosacchi, and S. Franchi. Synthesis and fundamental studies of $(H_3Ge)_{(x)}SiH_{4-x}$ molecules: Precursors to semiconductor hetero- and nanostructures on Si. *Journal of the American Chemical Society*, 127(27):9855–9864, 2005.

[17] K. Dettmer, U. Behner, and R. Beserman. Comparison of different Si/Ge alloy buffer concepts for $(Si_mGe_n)_p$ superlattices. *Journal of Crystal Growth*, 157(1):142–146, 1995.

[18] M. J. Ludowise, W. T. Deitze, R. Boettcher, and N. Kaminar. High efficiency (21.4%) $Ga_{0.75}In_{0.25}As$/GaAs (Eg = 1.15 eV) concentrator solar cells and the influence of lattice mismatch on performance. *Applied Physics Letters*, 43:468–470, 1983.

[19] C. R. Lewis, C. W. Ford, G. F. Vishup, B. A. Arau, R. T. Green, and J. G. Werthen. A two-terminal, two-junction monolithic cascade solar cell in a lattice-mismatched system. In *Proceedings of the 18th IEEE Photovoltaic Specialists Conference*, pages 556–561, Las Vegas, NV, 1985.

[20] J. C. Schultz, M. E. Klausmeier-Brown, M. L. Ristow, L. D. Partain, M. M. Al-Jassim, and K. M. Jones. Development of high-quantum-efficiency, lattice mismatched, 1.0-eV GaInAs solar cells. *Journal of Electronic Materials*, 22:755–761, 1993.

[21] R. W. Hoffman Jr., N. S. Fatemi, M. Stan, P. P. Jenkins, V. G. Weizer, D. Scheiman, and D. Brinker. High efficient ingaas-on-gaas devices for monolithic multi-junction solar cell applications. In *2nd World Conference on Photovoltaic Solar Energy Conversion*, pages 3604–3608, Vienna, Austria, 1998. IEEE.

[22] F. Dimroth, U. Schubert, and A. W. Bett. 25.5 percent efficient $Ga_{0.35}In_{0.65}P/Ga_{0.83}In_{0.17}$ as tandem solar cells grown on GaAs substrates. *IEEE Electron Device Letters*, 21(5):209–211, 2000.

[23] R. R. King, M. Haddad, T. Isshiki, P. Colter, J. Ermer, H. Yoon, D. E. Joslin, and N. H. Karam. Metamorphic GaInP/GaInAs/Ge solar cells. In *28th IEEE Photovoltaic Specialists Conference*, pages 982–985, Anchorage, Alaska, 2000. IEEE.

[24] C. M. Fetzer, H. Yoon, R. R. King, D. C. Law, T. D. Isshiki, and N. H. Karam. 1.6/1.1 eV metamorphic GaInP/GaInAs solar cells grown by MOVPE on Ge. *Journal of Crystal Growth*, 276(1-2):48–56, 2005.

[25] R. R. King, R. A. Sherif, D. C. Law, J. T. Yen, M. Haddad, C. M. Fetzer, K. M. Edmondson, G. S. Kinsey, H. Yoon, M. Joshi, S. Mesropian, H. L. Cotal, D. D. Krut, J. H. Ermer, and N. H. Karam. New horizons in III-V multijunction terrestrial concentrator cell research. In *21st European PV Solar Energy Conference*, Dresden, Germany, 2006.

[26] R. R. King, D. C. Law, K. M. Edmondson, C. M. Fetzer, G. S. Kinsey, H. Yoon, R. A. Sherif, and N. H. Karam. 40 percent efficient metamorphic GaInP/GaInAs/Ge multijunction solar cells. *Applied Physics Letters*, 90(18), 2007.

[27] J. F. Geisz, S. Kurtz, M. W. Wanlass, J. S. Ward, A. Duda, D. J. Friedman, J. M. Olson, W. E. McMahon, T. E. Moriarty, and J. T. Kiehl. High-efficiency GaInP/GaAs/InGaAs

triple-junction solar cells grown inverted with a metamorphic bottom junction. *Applied Physics Letters*, 91(023502), 2007.

[28] Brigham Young University. BYU - Cleanroom. (website), 2008.

[29] J. Haisma and G. A. C. M. Spierings. Contact bonding, including direct-bonding in a historical and recent context of materials science and technology, physics and chemistry — historical review in a broader scope and comparative outlook. *Materials Science & Engineering R-Reports*, 37(1-2):1–60, 2002.

[30] M. K. Weldon, Y. J. Chabal, D. R. Hamann, S. B. Christman, E. E. Chaban, and L. C. Feldman. Physics and chemistry of silicon wafer bonding investigated by infrared absorption spectroscopy. *Journal of Vacuum Science & Technology B: Microelectronics and Nanometer Structures*, 14(4):3095–3106, 1996.

[31] S. M. Sze. *Physics of Semiconductor Devices.* Wiley, New York, 2nd edition, 1981.

[32] M. K. Weldon, V. E. Marisco, Y. J. Chabal, A. Agarwal, D. J. Eaglesham, J. Sapjeta, W. L. Brown, D. C. Jacobson, Y. Caudano, S. B. Christman, and E. E. Chaban. On the mechanism of the hydrogen-induced exfoliation of silicon. *Journal of Vacuum Science & Technology B: Microelectronics and Nanometer Structures*, 15(4):1065–1073, 1997.

[33] M. K. Weldon, M. Collot, Y. J. Chabal, V. C. Venezia, A. Agarwal, T. E. Haynes, D. J. Eaglesham, S. B. Christman, and E. E. Chaban. Mechanism of silicon exfoliation induced by hydrogen/helium co-implantation. *Applied Physics Letters*, 73(25):3721–3723, 1998.

[34] Y. J. Chabal, M. K. Weldon, Y. Caudano, B. B. Stefanov, and K. Raghavachari. Spectroscopic studies of H-decorated interstitials and vacancies in thin-film silicon exfoliation. *Physica B: Condensed Matter*, 273–274:152–163, 1999.

[35] J. M. Zahler, A. F. I. Morral, M. J. Griggs, H. A. Atwater, and Y. J. Chabal. Role of hydrogen in hydrogen-induced layer exfoliation of germanium. *Physical Review B*, 75(3), 2007.

[36] K. N. Chen, C. S. Tan, A. Fan, and R. Reif. Morphology and bond strength of copper wafer bonding. *Electrochemical and Solid-State Letters*, 7(1):G14–G16, 2004.

[37] E. Yablonovitch, T. Sands, D. M. Hwang, I. Schnitzer, T. J. Gmitter, S. K. Shastty, D. S. Hill, and J. C. C. Fan. Van der Waals bonding of GaAs on Pd leads to a permanent, solid-phase-topotaxial, metallurgical bond. *Applied Physics Letters*, 59(24):3159–3161, 1991.

[38] V. Constantoudis, G. P. Patsis, A. Tserepi, and E. Gogolides. Quantification of line-edge roughness of photoresists. II. Scaling and fractal analysis and the best roughness descriptors. *Journal of Vacuum Science & Technology B*, 21(3):1019–1026, 2003.

[39] W. Shockley and H. J. Quiesser. Detailed balance limit of efficiency of p-n junction solar cells. *Journal of Applied Physics*, 32(3):510–519, 1961.

[40] C. H. Henry. Limiting efficiencies of ideal single and multiple energy gap terrestrial solar cells. *Journal of Applied Physics*, 51(8):4494–4500, 1980.

[41] G. Araujo and A. Marti. Absolute limiting efficiencies for photovoltaic energy conversion. *Solar Energy Materials and Solar Cells*, 33:213–240, 1994.

[42] J. K. Arch, F. A. Rubinelli, J. Y. Hou, and S. J. Fonash. Computer-analysis of the role of p-layer quality, thickness, transport mechanisms, and contact barrier height in the performance of hydrogenated amorphous-silicon p-i-n solar-cells. *Journal of Applied Physics*, 69(10):7057–7066, 1991.

[43] D. A. Clugston and P. A. Basore. PC1D version 5: 32-bit solar cell modeling on personal computers. In *Proceedings of the 26th IEEE Photovoltaic Specialists Conference*, pages 207–210, Anaheim, CA, 1997. IEEE.

[44] S. Michael, A. D. Bates, and M. S. Green. Silvaco ATLAS as a solar cell modeling tool. In *Proceedings of the 31st IEEE Photovoltaic Specialists Conference*, pages 719–721, Orlando, FL, 2005.

[45] N. J. Ekins-Daukes, T. R. Betts, Y. Kemmoku, K. Araki, H. S. Lee, R. Gottschalg, M. B. Boreland, D. G. Infield, and M. Yamaguchi. Syracuse — A multi-junction concentrator system computer model. In *Proceedings of the 31st IEEE Photovoltaic Specialists Conference*, pages 651–654, Orlando, FL, 2005. IEEE.

[46] M. Y. Ghannam, A. S. Alomar, N. Posthuma, G. Flammand, and J. Poortmans. Optimization of the triple junction $In_{0.5}Ga_{0.5}P$/GaAs/Ge monolithic tandem cell aimed

for terrestrial applications using an experimentally verified analytical model. *Kuwait Journal of Science & Engineering*, 31(2):203–234, 2004.

[47] A. L. Fahrenbruch and R.H. Bube. *Fundamentals of Solar Cells.* Academic Press, Inc., London, 1983.

[48] C. T. Sah, R. N. Noyce, and W. Shockley. Carrier generation and recombination in p-n junctions and p-n junction characteristics. *Proceedings of the Institute of Radio Engineers*, 45(9):1228–1243, 1957.

[49] W. Shockley and W. T. Read. Statistics of recombinations of holes and electrons. *Physical Review*, 87(5):835–842, 1952.

[50] A. Luque and S. Hegedus, editors. *Handbook of Photovoltaic Science and Engineering.* John Wiley & Sons, Ltd., Chichester, West Sussex, England, 2003.

[51] C. Y. Tsai, C. H. Chen, T. L. Sung, T. Y. Wu, and F. P. Shih. Theoretical model for intravalley and intervalley free-carrier absorption in semiconductor lasers: Beyond the classical drude model. *IEEE Journal of Quantum Electronics*, 34(3):552–559, 1998.

[52] M. Sotoodeh, A. H. Khalid, and A. A. Rezazadeh. Empirical low-field mobility model for III-V compounds applicable in device simulation codes. *Journal of Applied Physics*, 87(6):2890–2900, 2000.

[53] B. Marion, B. Kroposki, K. Emery, J. del Cueto, D. Meyers, and C. Osterwald. Validation of a photovoltaic module energy ratings procedure at NREL. *NREL Technical Report 520-26909*, 1999.

[54] S. M. Sze and Kwok K. Ng. *Physics of Semiconductor Devices.* Wiley, New York, 3rd edition, 2007.

[55] G. Letay, M. Hermle, and A. W. Bett. Simulating single-junction GaAs solar cells including photon recycling. *Progress in Photovoltaics: Research and Applications*, 14:683–696, 2006.

[56] M. Hermle, S. P. Philipps, G. Ltay, and A. W. Bett. Numerical simulation of tunnel diodes and multijunction solar cells. In *Proceedings of the 33rd IEEE Photovoltaic Specialists Conference*, San Diego, CA, 2008.

[57] J. R. Dong, S. J. Chua, Y. J. Wang, and H. R. Yuan. Substrate orientation dependence of In composition of AlGaInP epilayers grown by MOCVD. *Journal of Crystal Growth*, 269(2–4):408–412, 2004.

[58] C. P. Kuo, S. K. Vong, R. M. Cohen, and G. B. Stringfellow. Effect of mismatch strain on band-gap in III-V semiconductors. *Journal of Applied Physics*, 57(12):5428–5432, 1985.

[59] A. J. Rosakis, R. P. Singh, Y. Tsuji, E. Kolawa, and N. R. Moore Jr. Full field measurements of curvature using coherent gradient sensing: application to thin film characterization. *Thin Solid Films*, 325:42–54, 1998.

[60] D. Ngo, Y. Huang, A. J. Rosakis, and X. Feng. Spatially non-uniform, isotropic misfit strain in thin films bonded on plate substrates: The relation between non-uniform film stresses and system curvatures. *Thin Solid Films*, 515:2220–2229, 2006.

[61] D. Ngo, X. Feng, Y. Huang, A. J. Rosakis, and M. A. Brown. Thin film/substrate systems featuring arbitrary film thickness and misfit strain distributions. Part I: Analysis for obtaining film stress from non-local curvature information. *International Journal of Solids and Structures*, 44:1745–1754, 2007.

[62] M. A. Brown, A. J. Rosakis, X. Feng, Y. Huang, and Ersan Ustundag. Thin film/substrate systems featuring arbitrary film thickness and misfit strain distributions. Part II: Experimental validation of the non-local stress/curvature relations. *International Journal of Solids and Structures*, 44:1755–1767, 2007.

[63] W. C. Yeh, S. Chen, Y. S. Huang, C. H. Ho, and K. K. Tiong. Temperature dependent polarized-piezoreflectance study of GaInP. *Journal of Physics: Condensed Matter*, 12:2183–2192, 2000.

[64] Ioffe Physico-Technical Institute. Semiconductors on NSM. (website), 2008.

[65] S. Adachi. *Physical Properties of III-V Semiconductor Compounds*. Wiley, New York, 1992.

[66] P. Bhattacharya. *Properties of Lattice-Matched & Strained InGaAs*. INSPEC, the Institution of Electrical Engineers, London, 1993.

[67] Mathias Schubert, V. Gottschalch, Craig M. Herzinger, Huade Yao, Paul G. Snyder, and John A. Woollam. Optical constants of $\mathrm{Ga_xIn_{1\text{-}x}P}$ lattice matched to GaAs. *Journal of Applied Physics*, 77(7):3416–3419, 1995.

[68] S. M. Kelso, D. E. Aspnes, M. A. Pollack, and R. E. Nahory. Optical properties of $\mathrm{In_{1\text{-}x}Ga_xAs_yP_{1\text{-}y}}$ from 1.5 to 6.0eV determined by spectroscopic ellipsometry. *Physical Review B*, 26(12):6669–6681, 1982.